AMERICAN UNIVERSITY OF BEIRUT

SYNTHESIS AND APPLICATION OF PHOTOLUMINESCENT DOPED LANTHANIDE OXIDE MICROSPHERES USING THE REACTION-DIFFUSION FRAMEWORK (RDF)

by
CHRISTINA RENEE KATBE

A thesis
submitted in partial fulfillment of the requirements
for the degree of Master of Science
to the Department of Chemistry
of Faculty of Arts and Sciences
at the American University of Beirut

Beirut, Lebanon
June 2023

AMERICAN UNIVERSITY OF BEIRUT

SYNTHESIS AND APPLICATION OF
PHOTO-LUMINESCENT LANTHANIDE
DOPED LANTHANUM OXIDE
MICROSPHERES USING THE
REACTION-DIFFUSION FRAMEWORK (RDF)

by
CHRISTINA RENEE KATBE

Approved by:

_____

Dr. Mazen Al Ghoul, Professor   Advisor
Chemistry

_____

Dr. Houssam El-Rassy, Professor   Member of Committee
Chemistry

_____

Dr. Digambara Patra, Professor   Member of Committee
Chemistry

Date of thesis defense: June 22, 2023

AMERICAN UNIVERSITY OF BEIRUT

THESIS RELEASE FORM

Student Name: ___Katbe_____Christina_____Renee____

                         Last   First   Middle

      I authorize the American University of Beirut, to: (a) reproduce hard or electronic copies of my thesis; (b) include such copies in the archives and digital repositories of the University; and (c) make freely available such copies to third parties for research or educational purposes

___ **As of the date of submission of my thesis**

___ **After 1 year from the date of submission of my thesis .**

✓ **After 2 years from the date of submission of my thesis .**

___ **After 3 years from the date of submission of my thesis .**

Christina Renee Katbe

_____   30 June 2023

       Signature   Date

ACKNOWLEDGEMENTS

Abstract
of the Thesis of

Christina Renee Katbe   for   Master of Science

                                                Major: Chemistry

Title: Synthesis and Application of Photo-luminescent Lanthanide Doped Lanthanum Oxide Micro-spheres Using the Reaction Diffusion Framework (RDF)

Self-organization is the spontaneous process whereby some form of overall spatiotemporal order arises from synergies between parts of an initially disordered system. It occurs in open systems driven away from thermal equilibrium. Liesegang banding is a type of far-from-equilibrium self-organizing phenomenon that emerges due to the coupling of diffusion to precipitation chemical reactions[1]. We can exploit Liesegang banding to make crystalline material via the so-called reaction-diffusion framework (RDF); a method which allows control over the size, morphology, and composition of crystalline solids[2]. In this work, we are particularly interested in studying the optical properties of lanthanide-doped lanthanum oxide mono-dispersed spheres synthesized in an agar hydrogel matrix via the reaction-diffusion framework (RDF). Having long excited state lifetimes in the millisecond range, resistance to photo-bleaching, and low toxicity, Lanthanide-doped luminescent inorganic nanoparticles give rise to promising possibilities for light-emitting applications, bioassays, and bioimaging[3], [4].

First, the lanthanum hydroxide crystals (pure and doped) are precipitated by pouring an outer electrolyte of concentrated ammonia onto agar gel containing the lanthanide salts in given initial proportions. Macroscopically, the resulting lanthanum hydroxide material forms a set of Liesegang bands. SEM images of individual bands reveal a microscopic hierarchical structure of nano-platelets self-assembling into exquisitely shaped nano- and micro- spheres[2].The average size of the spheres depends on the selection of a specific Liesegang band and the resulting set. As expected, RDF provides a green, fast and easy synthetic route to obtain lanthanide-doped nanoparticles. The dopants used include erbium, samarium, europium and terbium ions. The lanthanide doped La_2O_3:Ln^{3+} (Ln = Eu, Sm, Eu, Tb) phosphors[5] are obtained from the corresponding hydroxide by calcination. The emission spectra of the lanthanide-doped La_2O_3 phosphors are found to exhibit

classic sharp easily recognizable inner-shell 4f-4f transitions which span both the visible and near-infrared (NIR) ranges[4].

TABLE OF CONTENTS

Illustrations

9

TABLES

ABBREVIATIONS

RDF   Reaction Diffusion Framework
PXRD   Powder X-ray Diffraction
SEM   Scanning Electron Microscope
DLS   Dynamic Light Scattering
BET   Brunner-Emmett-Teller surface area analyzer
FTIR   Fourier Transform Infrared Spectroscopy
UCNPs   Up-converting Nano-particles
RE   Rare Earth
LRET   Luminescence Resonance Energy Transfer
LOD   Limit of Detection
PL   Photo-luminescence

CHAPTER 1

INTRODUCTION

1.1 Lanthanide Doped Lanthanum Oxide

1.1.1 *Properties of Dopant Trivalent Lanthanide Ions*

The intricate optical properties of the trivalent lanthanide ions Ln III originate in the special features of the electronic $[Xe]4f^n$ configurations (n = 0–14) which result in Lanthanide ions possessing a large number of metastable energy levels , as shown in figure 1.3, due to the configurations giving rise to a large number of electronic arrangements called microstates. The number of microstates arising from each electronic configuration can be calculated using the formula $\frac{14!}{n!(14-n)}$ where n refers to the number of 4f electrons. In the case of Eu(III) dopant, having the electron configuration $[Xe]4f^6$ the number of microstates would be $\frac{14!}{6!(14-6)!} = 3003$ microstates. The microstates are characterized by three quantum numbers S, L, and J, within the frame of Russell-Saunders spin-orbit coupling scheme, where S is the total spin quantum number, L is the total orbital angular momentum quantum number and J is the total angular quantum number which indicates the relative orientation of the spin and the orbital momenta. These can be grouped into 259 $^{2S+1}L_J$ electronic terms for Eu(III). The number of microstates grouped within each of the 259 electronic states is $(2\,S+1)\,(2\,L+1)$ or $(2\,J+1)$. The possible values for J are L + S, L + S –1, L + S – 2, . . ., $|L-S|$[6].

Considering the lanthanide-doped luminescent nanoparticles feature octahedrally coordinated dopants, the degeneracy of the energy states generated by the $4f^n$ configurations is partly or totally lifted by crystal field effects that arise due to interactions between the lanthanide dopants and the ligands as shown in figure 1.1. The energies of these levels are well-defined due to the shielding of the 4 f orbitals by the filled $5s^2 5p^6$ subshells which makes lanthanide luminescence highly insensitive to the chemical environment[5], [7]. As a result, inner shell 4f–4f transitions which span the visible and near-infrared (NIR) ranges are sharp and easily recognizable as shown in figure 1.2. For example, Eu^{3+} luminescence is characterized by emissions at 590 nm, 610 nm, and 720 nm, Tb^{3+} luminescence is characterized by line-like emissions at 490 nm, 540 nm, and 580 nm, Er^{3+} luminescence is characterized by line-like emissions at 543 nm, 552 nm, and 650 nm, and Sm^{3+} luminescence is characterized
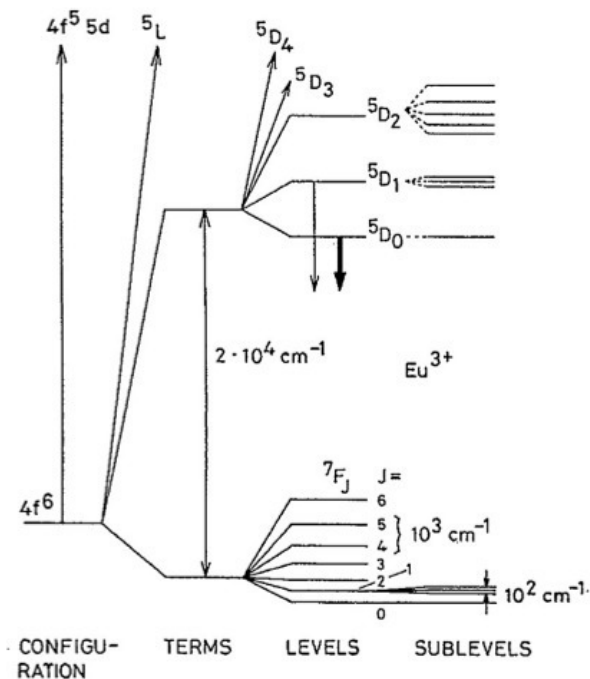
Figure 1.1: Partial Energy Diagram of Eu^{3+} showing the magnitude of the inter-electronic repulsion (terms), spin-orbit coupling (levels), and crystal feild effects (sublevels). Adapted from [6].

by line-like emissions at 564 nm, 600 nm, 650 nm, and 713 nm[8]–[10].

When discussing light emission by Lanthanide dopant ions, the term "luminescence" is used as opposed to "fluorescence" or "phosphorescence". The terms fluorescence and phosphorescence are commonly used to describe light emission by organic molecules. These terms also incorporate information on the emission mechanism; fluorescence referring to spin allowed singlet to singlet emission, and phosphorescence referring to spin forbidden triplet to singlet emission. In the case of Lanthanide ions, emissions are due to intraconfigurational transitions within the 4f sub-shell. Once excited, the Lanthanide ion undergoes a radiative transition to a lower 4f state by characteristic line-like photo-luminescence. Luminescence refers to all radiative transitions from excited states and comprises a broader set of transitions than fluorescence or phosphorescence. Luminescence by a Lanthanide ion is only possible from certain levels termed resonance levels. In the case of Eu^{3+}, $^5D_0$ is the main resonance level. If the Ln^{3+} is excited to a certain non-emitting level, the excitation energy is dissipated via non-radiative processes until a resonance level is reached[7], [11].

Upon direct excitation, Ln(III) ions display a negligible Stokes' shift; however, when the Ln(III) ions are used as dopants, ligand excitation leading to dopant excitation results in large pseudo Stokes' shifts which allow the easy distinction between emission and absorption bands. This permits easy spectral discrimination of their emission bands in the visible and NIR ranges[6], [13]. When the lanthanide dopants occupy octahedral sites, non-centrosymmetric interactions allow the mix-

Figure 1.2: Emission Spectra of selected trivalent Lanthanide Ions. Adapted from [12].

Figure 1.3: Calculated energy levels of the trivalent lanthanides in the energy range up to 40,000 cm^{-1}. Adapted from [12].

ing of electronic states of opposite parity into the 4f wave functions. As a result, electric dipole 4f–4f transitions which are originally parity forbidden become partly allowed and result in photoluminescence. These transitions are known as forced electric dipole transitions. Because these transitions are formally parity forbidden, the lifetimes of the excited states are long and extend to the millisecond range, thus allowing the use of the doped lanthanides in time resolved detection[4], [13], [14].

Concentration quenching represents a major obstacle toward constructing efficient Ln^{3+} doped Oxides and Fluorides when it comes to luminescence efficiency. An elevated concentration of dopant ions leads to higher luminescence intensity due to the presence of a higher density of optical centers which collect and sustain the excitation energy. However, when the % dopant exceeds a certain system dependant threshold, the reduced inter-dopant distance resulting from the higher % Ln^{3+} dopant enhances interactions of optical centers. These deleterious interactions which include localized cross-relaxation, phonon-assisted energy transfer, and long-distance energy migration to lattice/surface defects diminish the luminescence intensity of the system due to the depopulation of the excited states[15]. Energy gain resulting from light absorption increases with dopant concentration according to the Lambert-Beer Law [16]:

$$E_G = I_0(1 - e^{-aC})$$

where I_0 is the incident light intensity, a is a constant related to the absorptivety of the dopant, and C is the dopant concentration.

Energy loss (E_L) is dictated by Forster resonance energy transfer in relation to the quantity of quenching centers through [17]:

$$E_L = kC^2$$

where k is a constant affected by the quenching process and C is the dopant concentration. Based on the latter equations, concentration quenching can be mitigated by an increase of excitation intensity and/or suppression of energy trapping by quenching sites[15].

1.1.2 *Synthesis Methods*

Due to their exquisite optical properties, a variety of chemical synthetic approaches have been adopted to synthesize lanthanide-doped luminescent nanoparticles, such as Lanthanide doped Lanthanum Oxide, with controlled morphology, monodispersity, and high crystallinity. The most representative methods include thermal decomposition[3], [18], [19], high temperature coprecipitation[20], and hydro(solvo)thermal synthesis[3], [19], [21]. Formation of Lanthanide-doped luminescent nanoparticles specifically Ln^{3+} doped La_2O_3 is discussed below.

1.1.2.1   Thermal Decomposition

Using thermal decomposition to prepare high quality Ln^{3+} doped luminescent nanoparticles involves the formation of the doped species from organometallic compounds

such as metal trifluoroacetate La(CF$_3$COO)$_3$ placed at high temperatures in a high boiling point organic solvent such as 1-octadecene(ODE). Surfactants such as oleic acid or oleylamine which typically contain a functional capping group to coordinate the metallic elements and a long hydrocarbon chain to prevent nano-particle aggregation are also added[22]. By optimizing the use of different variables such as the type of solvent, concentration of the metal precursor, reaction temperature and time, one can obtain high quality mono-dispersed nano-particles with good crystallinity. The main drawback regarding this synthesis method is the need to use expensive, air-sensitive, highly toxic Ln^{3+} trifluoroacetate precursors as well as the formation of hazardous by-products such as HF[3]. Nucleation and growth processes using this method are also very fast. This increases the amount of defects in the formed crystals and leads to a lower up-conversion quantum yield[19], [22]. Decomposition method has has enabled the synthesis of many RE fluorides, oxides, and oxyfluorides such as LaF$_3$[23], NaYF$_4$[24], [25], LiYF$_4$[26], MF$_2$ (M = Mg, Ca, and Sr)[27].

1.1.2.2 Hydro(solvo)thermal Synthesis

Hydro-thermal synthesis involves a chemical reaction taking place in a closed vessel at high temperatures above the critical point of the solvent, and at high pressures. The vessel is used to provide a high pressure high temperature sealed environment to promote reactions between solid precursors and form highly crystalline nano-materials. The pressure temperature conditions facilitate the dissolution of the chemical reagents and the production of products by crystallization. In a typical procedure of hydro(solvo)thermal synthesis, appropriate reaction precursors, solvents, and surfactants with functional groups are mixed and then heated in the specialized reaction vessel. Surfactants like polyethylenimine (PEI)[28],ethylenediaminetetraacetic acid (EDTA)[29], cetyltrimethylammonium bromide (CTAB)[30],and OA[31] provide chelating ability with cationic dopant ions to regulate their reacting concentration and attain control over the crystalline phases, sizes, morphologies, and surface functional groups. Once cooled to room temperature, the products are washed, centrifuged and dried[3], [32]. A variety of lanthanide-doped UCNPs with well-controlled crystal phase, size, and shape have been synthesized via this method including NaYF$_4$[33], NaLaF$_4$[31], NaLuF$_4$[34], BaGdF$_5$[35], KMnF$_4$[36]. The main drawback of this synthesis method is the impracticality of needing specialized reaction vessels (autoclaves), and the inability to watch the particles as they grow[19].

1.1.2.3 High Temperature Co-precipitation

High temperature co-precipitation depends on Ostwald ripening, the process where larger particles with smaller surface-to-volume ratios are favored over energetically less stable smaller particles, resulting in the growth of larger particles at the expense of smaller ones[37]. High temperature co-precipitation bypasses the need to use organic solvents and provides a cost-effective way to synthesize highly crystalline luminescent nano-particles doped with Ln^{3+} emitters at a high yield. This method is more favorable in terms of its milder reaction conditions, low cost for required equipment and short reaction time. Nucleation occurs when concentrations of the

mixed species reaches critical super-saturation and growth of the nuclei occurs via diffusion of the solutes to the surface of the crystal. Adopting this synthesis method is problematic due to the broad size distribution, ill-defined shapes, and low luminescence efficiency of the final products. To achieve mono-dispersity, nucleation and growth should ideally be separated. This is achieved by coating the nanoparticles with carboxylate surfactant during the nucleation process at room temperature followed by dispersion of the nanoparticles in an organic medium during growth at high temperature[3], [19]. Hexagonal phase $NaYF_4$:Yb^{3+}/Er^{3+}(or Tm^{3+}) UC-NPs are synthesized via this method using OA as the capping ligand and ODE as the high boiling point solvent. In this case, $NaYF_4$ coprecipitates at room temperature followed by the growth of the nano-particles using the Ostwald ripening process at elevated temperatures (300 ^{o}C)[38]–[40].Controlling the ripening process by regulating temperature and reaction time allows one to produce hexagonal phase, mono-dispersed nano-particles, with narrow size distribution[22].

1.1.2.4 Solution Combustion

Solution combustion involves a self-sustained reaction in a homogeneous solution of different oxidizers (e.g., metal nitrates) and fuels (e.g., urea, glycine, hydrazides). Synthesizing La_2O_3 could be accomplished by mixing $La(NO_3)_3$ with acetamide. The solution is placed in the furnace at 600 °C for a few hours, then cooled for 4-5 hours [3], [19], [22], [41].

1.1.2.5 Sol Gel

A sample procedure for Sol Gel synthesis of La_2O_3 includes forming a sol consisting of $La(OH)_3$ dispersed in 40 ml of deionized water. 0.1 M NaOH solution is added to the $La(OH)_3$ solution and stirred using a magnetic stirrer to adjust the pH of the solution to about 10-11. 10 vol% TEOS tetraethoxysilane controlled with methanol is added drop-wise with continuous stirring. The solution is heated in an oil bath at 40°C for 2 hours. The gel is later dried at 120°C and calcined at 800°C for 2 hours[3], [19], [22].

1.1.2.6 Sonochemical Synthesis

Sonochemical synthesis of Lanthanum oxide involves a 2 step synthesis where Lanthanum carbonate is generated from a Lanthanum acetate precursor coated with PEG (polyethylene glycol) surfactant. The lanthanum carbonate nanoparticles are then calcined at 600°C for 2 hours to synthesize lanthanum oxide nanoparticles. Sonolysis of the weak metal carbon bonds in Lanthanum acetate inside collapsing bubbles allows diffusion into the bulk liquid to form functional nanomaterials. The extreme, transient conditions produced during acoustic cavitation, allow a reaction that would otherwise require high temperature, high pressures, and long reaction times[19], [42].

1.1.2.7 Reflux

Formation of La_2O_3 by reflux involves a 2 step synthesis where a precursor solution of $La(NO_3)_3 \cdot 6\,H_2O$ and urea is maintained in a round bottom flask at a temperature of 120°C for 24 h. Prepared nanoparticles are then calcined at 500°C for 1 h[19].

1.1.2.8 Spray Pyrolysis

Forming La_2O_3 via spray pyrolysis is obtained when a solution containing a $LaCl_3 \cdot 7\,H_2O$ precursor is sprayed with H_2O_2 in the furnace, leading to the decomposition of the precursor to form the final desired material on the substrate. The nanostructure parameters of the formed La_2O_3 including particle size, shape, and thickness are controlled by controlling the spray energy, the droplet size of the precursors, the duration of the spray, the distance between the spray gun and the substrate, and the temperature of the furnace and substrate[19], [43].

1.1.3 *Applications*

Having low toxicity, long-lived luminescence, sharp easily recognizable emission bands and large anti-Stokes shift that allow for spectral and time discrimination of sharp f–f transitions, lanthanide doped nanoparticles have become top candidates for light emitting and biological applications that exploit their luminescence lifetime in the millisecond range as well as their viability for up-conversion applications[4], [14]. Lanthanide doped nanoparticles are well suited for theranostics due the efficiency of their implementation in imaging, drug delivery, bio-sensing, and bio-assays. Lanthanide dopant ions can produce visible emissions when excited by IR light or by UV light. Excitation of Lanthanide doped nano-particles using IR, long wavelength light, as opposed to short wavelength light for imaging makes them particularly appealing because imaging can be accomplished free from background noise of biological samples which are excited by short wavelength UV light. Ln^{3+} doped La_2O_3 imaging agents can therefore operate within the optical transparency window of living cells (700-1100 nm). Traditional photoluminescence imaging agents such as heavy metal-based quantum dots exhibit low signal-to-background ratio (SBR) due to unwanted auto-fluorescence and strong light scattering of biological tissues when short wavelength excitations are applied[3], [13], [22], [44]. Even if UV light is used for excitation of Ln^{3+} doped material, interference of background noise of biological tissues doesn't pose a problem considering the background noise generated by auto-fluorescence of biological samples has lifetimes in the nanosecond range while the photoluminescence lifetime of the doped nanoparticles is in the millisecond range. In this case, time resolved photoluminescence (TRPL) can be used to detect and quantify analyte without the interference of short-lived background noise of biological samples[4]. In addition to traditional photoluminescence imaging agents producing low signal to background ratio, these agents risk potential DNA damage and cell death due to exposing the human body to short wavelength UV excitation for long periods of time and due to being toxic themselves in some instances. For example, heavy metal-based quantum dots for bio-imaging contain toxic elements such as

cadmium, mercury, and lead[3], [13], [22], [44]. Ln^{3+} doped nanoparticles provide an excellent alternative to traditional imaging agents considering they produce a high signal to background ratio when imaging biological samples regardless of whether IR or UV light is used for excitation, and they are not toxic.

Due to the lanthanide dopants having a large number of meta-stable energy levels, lanthanide doped materials are an excellent means for achieving photon up-conversion; a process where low energy near infrared (NIR) photons are converted to high energy ultraviolet or visible photons via an energy transfer between the closely spaced energy levels of the dopants[5]. Ln^{3+} doped La_2O_3 are used to facilitate two main upconversion processes including Excited State Absorption and Energy Transfer Upconversion. Excited State absorption (ESA) as shown in figure 1.4a is the simplest upconversion process where an ion absorbs a photon whose energy matches that of an excited state E1, and moves from the ground state G to excited state E1. The ion is subsequently excited by another matching photon to the excited state E2. When the ion decays from excited state E2 to the ground state, upconverted light is emitted. ESA is achieved when Ln^{3+} dopant ions have a ladder-like arrangement of energy levels such that the excitation wavelength of these dopants matches the output of commercially available diode lasers. Lanthanide ions matching this description include $Er^{3+}, Ho^{3+}, Tm^{3+}$, and Nd^{3+}[22], [45]. Energy transfer upconversion (ETU) as shown in figure 1.4b utilizes two or more lanthanide dopants, where one dopant, termed the sensitizer, absorbs light and acts as a donor, and the other Lanthanide dopant, termed the activator, accepts and emmits the light originally absorbed by the sensitizer. The first step of this process includes the sensitizer absorbing a photon and being promoted from it's ground state to it's first excited state, and transferring the absorbed energy to the acceptor. Ion 2 is then excited to its intermediate excited state and further excited from the intermediate state to the excited state E2 upon absorbing another photon. When ion 2 decays from E2 to the ground state, it emits upconverted light. The most common pairs of dopants used to achieve ETU include Er^{3+} /Yb^{3+} or Tm^{3+} /Yb^{3+} where Yb^{3+} is a convenient sensitizer due it having only one excited state thus preventing risk of cross relaxation[22], [45].

1.1.3.1 Biological Assays

Developing non-intrusive nontoxic methods for analysis of diverse bio-molecules particularly cancerous bio-markers in human fluid samples is critical for early cancer theranostics, and for increasing patient survival. Lanthanide doped nanoparticles such as Lanthanide doped Lanthanum Oxide micro-spheres have provided a means to achieve two main efficient bio-assay methods including heterogeneous sandwich-type photoluminescence (PL) assays and homogeneous LRET assay techniques[46], [47]; the distinguishing factor between the two groups being their signal detection formats[48].

Heterogeneous assays are used for detection of trace amounts of analyte anchored on a solid substrate via capture molecules. The high binding affinity be-
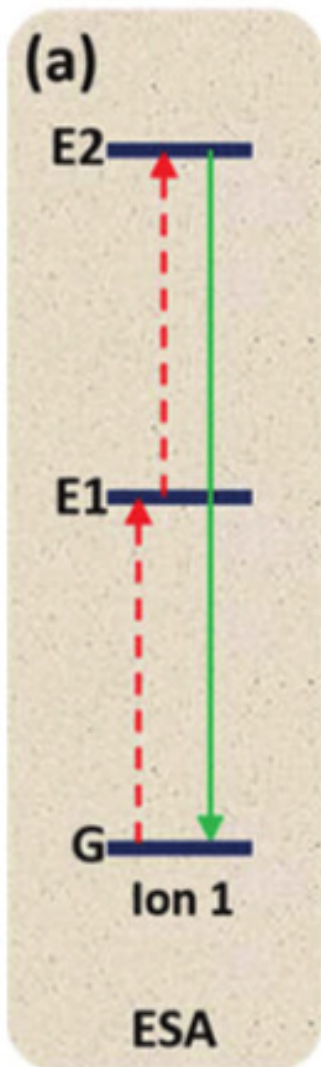
(a) Excited State Absorption(ESA): Upconversion process where an Ln^{3+} dopant ion absorbs a photon whose energy matches that of E1, moves from G to E1, is subsequently excited by another matching photon to E2, and decays from E2 to the ground state emitting upconverted light.
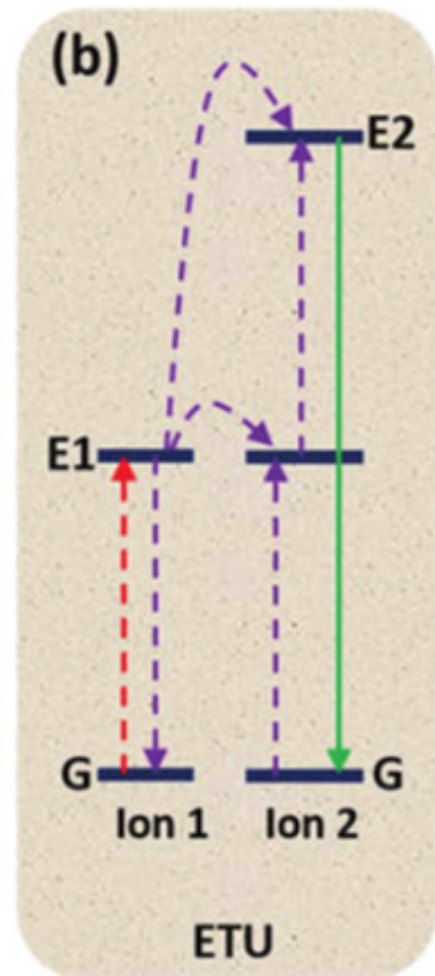
(b) Energy Transfer Upconversion(ETU): Upconversion process where a sensitizer absorbs a photon, is promoted from G to E1, and transfers the absorbed energy to the ion 2. Ion 2 is promoted to E1, and is further excited to E2 upon absorbing another photon. When ion 2 decays from E2 to G, it emits upconverted light.

Figure 1.4: Upconversion Processes, adapted from [45]

(a) Non-competitive Heterogenous Assay

(b) Competitive Heterogeneous Assay
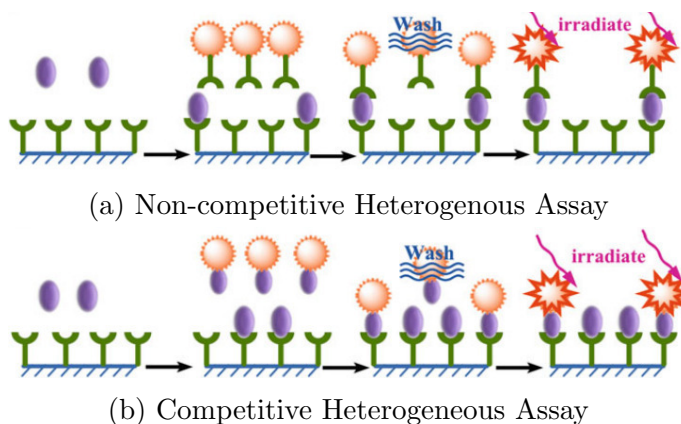
Figure 1.5: Schematic illustration of typical heterogeneous assays based on Ln^{3+}-doped nanoprobes. Adapted from [3].

tween these target analytes and capture molecules allows for the quantification of trace amounts of analyte[49]. In a noncompetitive heterogeneous assay, the analyte that needs to be quantified is immobilized on a solid phase. The Ln^{3+} doped nanoparticle labelled capture molecule which binds to the analyte is then added. After excess capture molecules are washed off, photoluminescence measurements of the lanthanide doped luminescent nanoparticles are taken. Since the intensity of the emission is directly proportional to the amount of analyte, the amount of analyte can be determined as shown in figure1.5a. In a competitive heterogeneous assay, nano-particle labelled analyte instead of nano-particle labelled capture molecule is added to compete with free analyte to bind to the capture molecule as shown in figure1.5b. In this case, the photoluminescence intensity is inversely proportional to the amount of free analyte[3]. If the bio-assays are carried out using a UV excitation light source, unwanted interference of scattered light and auto-fluorescence from cells and tissues are minimized by employing time resolved photoluminescence detection techniques (TRPL). By setting the appropriate delay time and gate time, higher detection sensitivity with better signal to noise ratio is obtained. When NIR light is used for excitation of upconverting Lanthanide doped nanoparticles to achieve visible emissions, no auto-fluorescence from biological cells and tissues is obtained[3]. This has lead to significantly improved LOD in heterogeneous assays over conventional assays. Heterogeneous bioassays based on UC particles were reported for the detection of numerous bio-markers including prostate-specific antigen (PSA) in human prostate tissue[50], human chorionic gonadotropin[51], levels of drug abuse[52], DNA[53], [54], bacterial pathogens (Streptococcus pneumoniae)[55], and nucleic acids[56].

Homogeneous LRET assays is another technique for bio-molecule identification where biochemical recognition is transduced to an optical signal given by UCNPs such as Lanthanide doped Lanthanum Oxide. The transduction is implemented by an LRET mechanism where UCNPS act as energy donors. Homogeneous assays are less labor intensive than heterogeneous bioassays which require tedious separation

and washing steps. LRET involves the detection of biomolecules in solution due a distance dependent energy transfer between an excited donor and a nearby acceptor in close proximity. The emission of the lanthanide doped luminescent nanoparticles and the absorbance of the acceptor overlap, therefore based on the frequency of the emitted light, one can distinguish whether light was emitted from the acceptor in close proximity to the donor or simply from the donor[3]. This process is also achieved by labelling a Lanthanide doped UCNP and an acceptor molecule with the capture molecule that can specifically seize the analyte. When the capture molecule labeled UCNPs and the capture-molecule-labeled acceptor molecules are far from each other in the solution, no detectable signal is produced. The presence of analytes (bio-molecules we are interested in detecting) can bring the UCNPs and the acceptor molecules into close proximity to establish an LRET process as shown in figure 1.7[49], [57], [58]. If UV light is used for excitation instead of IR light and TR-LRET (time resolved luminescence resonance energy transfer) is applied, the long luminescence lifetime of the dopants can clear background noise resulting from emissions of biological molecules whose emissions have short lifetimes[3], [13], [44], [59].

Among the bio-markers detected using LRET is biotin, which was detected at $\lambda_{excitation}$= 980 nm using streptavidin-conjugated Er^{3+},Yb^{3+}-doped UPC phosphor as a donor and bio-tinylated phycobiliprotein as an acceptor[60]. Another instance includes identifying target-DNA with a LOD of 1.3 nm using oligonucleotide-modified UCNPs. Here, a short oligonucleotides is covalently bound to the photon upconverting particle, while another oligonucleotide is labeled with a fluorophore whose excitation spectrum overlaps with the emission spectrum of the upconverting particle. In the presence of the target oligonucleotide, the fluorophore is brought close to the UCNP, and energy transfer takes place, leading to the light emission from the fluorophore as shown in figure 1.6[61]. Besides organic dyes, metallic nanoparticles like gold nanoparticles have also been investigated as superior quenchers of UC donors in homogeneous assays. An example includes the detection goat antihuman immunoglobulin G (IgG) using LRET where NIR UCNPs $NaYF_4$:Yb^{3+},Er^{3+} act as energy donors and gold nanopaticles act as energy acceptors in a sandwich-type LRET-based immunoassay for the detection of goat antihuman immunoglobulin G (IgG)[62], [63].

In addition to biomolecule detection, LRET can also be used for the detection of metal ions and gas molecules. Metal ions including cyanide CN^- and mercuric ions Hg^{2+} are extremely toxic to mammals. UCNPs can be used for the detection of these ions in an LRET process where the UCNPs serve as energy donors and organic dyes with a recognition capacity for the ions of interest are energy acceptors. The biochemical recognition between the organic indicator and ion of interest will then modulate the luminescence intensity, displaying a colorimetric change. Hg^{2+} can be detected in an aqueous media using $NaYF_4$:Yb^{3+}/Tm^{3+} as an energy donor and SYBR green, a DNA intercalating dye, as an energy acceptor. By monitoring the ratio of acceptor emission to donor emission, the amount of Hg^{2+} can be quantitatively detected in solution[22], [64]–[67]. CN^-,a toxic anion which can strongly interact with the active site of cytochrome a_3 and inhibit cellular respiration in mammalian
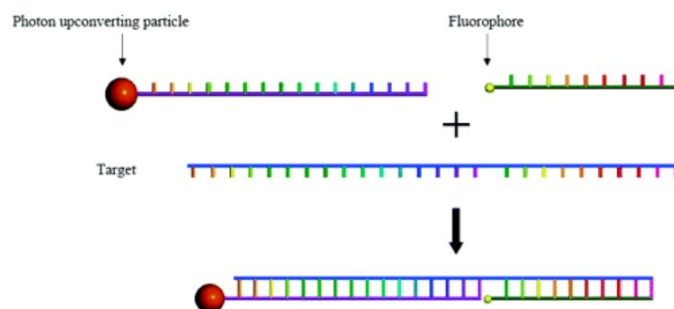
Figure 1.6: LRET based Nucleotide Sensor Diagram. Adapted from [61].
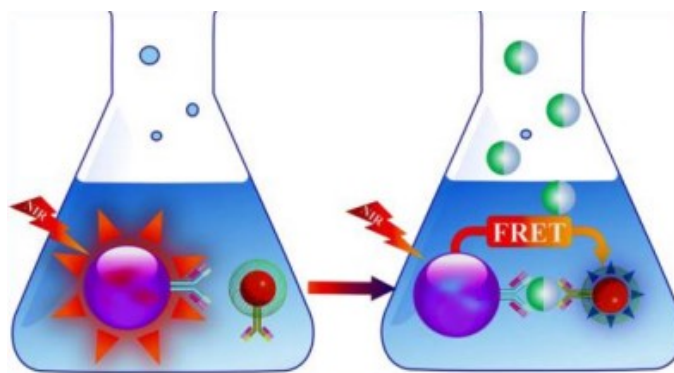
Figure 1.7: Homogenous LRET Biological Assay based on distance-dependent energy transfer between an energy donor (UCNPs) and a nearby acceptor molecule through long-range dipole-dipole interactions to detect analytes in the solution. Adapted from [22].

cells[68], can be detected using hydrophobic oleic acid (OA)-coated $NaYF_4$: 20% Yb^{3+}, 2% Ho^{3+} upconversion nanophosphor as an energy donor and a CN^- reactive Iridium(III) complex $([(ppy)_2Ir(dmpp)]PF_6)$ as an energy acceptor. Upon excitation $\lambda_{excitation}$= 980 nm, the absorbance of the Iridium complex overlaps with the emission band of the UCNPs at 540 nm, whereby an LRET process between them will quench the green emission of the UCNPs. After CN^- is added to the medium, the absorbance intensity of the Iridium complex bleaches dramatically due to the reaction of the complex with CN^-. This causes the LRET to be less effective and recovers the green emission of the UCNPs[69]. Determination of the concentration of gas molecules such as oxygen, carbon dioxide, and ammonia is of very high priority especially when monitoring biochemical reactions in the human body[70]–[72]. One of the first Oxygen sensors using UCNPs involved using the $NaYF_4$:Yb^{3+}/Tm^{3+} as an energy donor and an Iridium complex $[Ir(CS)_2(acac)]$ as an energy acceptor; both of which were incorporated into an ethyl cellulose thin film. Upon laser excitation at λ= 980 nm, the blue emission of the UCNPs photo-excites the iridium complex dissolved in ethyl cellulose which emits green light. This green emission is reversibly quenched by the presence of molecular Oxygen, thus detection of Oxygen can be accomplished by monitoring the extent of quenching[22], [73], [74].

1.1.3.2 Biosensing

Temperature Sensing is an extremely valuable tool especially for monitoring reactions within living systems. Developing a suitable bio-compatible temperature probe having minimal interactions with the cellular constituents has been highly sought after because it would allow the study of the effects of temperature on temperature sensitive reactions in vitro[75]. This can actually be accomplished via photo-luminescent Lanthanide doped Lanthanum Oxide UCNPs which can be used as versatile optical nanothermometers[76]–[78]. An excellent candidate for temperature sensing is Er^{3+} doped La_2O_3. This is because the photo-luminescence emission intensity ratio of Er^{3+} ions at 520 nm from the $^2H_{11/2} \to {}^4I_{15/2}$ and at 550 nm from the $^4S_{3/2} \to {}^4I_{15/2}$ transition is very sensitive to temperature. The populations of $^2H_{11/2}$ and $^4S_{3/2}$ follow the Boltzmann Distribution Law under steady-state excitations; therefore, the ratio of the two intensities for the mentioned transitions I_{520} and I_{550} can be related to the temperature through the following equation:

$$\frac{I_{520}}{I_{550}} = A exp\left(\frac{-\Delta E}{K_b T}\right)$$

$$ln\left(\frac{I_{520}}{I_{550}}\right) = \frac{-\Delta E}{K_b}\left(\frac{1}{T}\right) + ln(A)$$

where K_b is the Boltzmann constant, ΔE is the energy gap between the two excited levels, and A is a constant depending on the lifetimes of the 2 levels[22], [75], [79]. This reveals that the ratio I_{520}/I_{550} will increase as the temperature increases. $ln\left(\frac{I_{520}}{I_{550}}\right)$ will also vary linearly with the inverse of the temperature[80].

An $NaYF_4$:$Er^{3+}Yb^{3+}$ nanothermometer has been reported as a thermal nanoprobe for temperature sensing in liquids and HeLa cervical cancer cells[22], [75], [79]. In this case, the Fluoride matrix is co-doped with Yb^{3+} which acts as a sensitizer and Er^{3+} which acts as an emitter in an energy transfer upconversion process used to emit visible light in response to excitations at $\lambda ex.= 920$ nm. The Yb^{3+} has one excited state $^2F_{5/2}$ that is resonant with the $^4I_{11/2}$ state of Er^{3+}. The Er^{3+} ion is excited to its $^4F_{7/2}$ state via two successive energy transfers from Yb^{3+} promoting it from it's ground state $^4I_{15/2}$ to the intermediate $^4I_{11/2}$ and subsequently to the excited state $^4F_{7/2}$ as shown in figure 1.8a. Temperature sensitive green emissions consists of bands centered at 525 nm and 545 nm due to the transitions $^2H_{11/2} \to {}^4I_{15/2}$, and $^4S_{3/2} \to {}^4I_{15/2}$ respectively. As the temperature increases, the ratio I_{525}/I_{545} increases[80]; therefore, a thermometric scale for the temperature-sensitive water-dispersible nanoparticles can be obtained as shown in figure 1.8b. Given the fact that $NaYF_4$:Er^{3+}, Yb^{3+} nanoparticles can be efficiently internalized by Hela cervical cancer cells, their thermal sensitivity can be exploited to create a nanothermometer capable of measuring the internal temperature of a living cancer cell[81]. In this case, the Er^{3+} doped nanoparticles function as nanothermometers for monitoring intracellular conditions. The mode of functioning consists of using the change in the I_{525}/I_{545} intensity ratio in response to an applied voltage to measure the internal temperature of the illuminated HeLa cells at each corresponding voltage. The
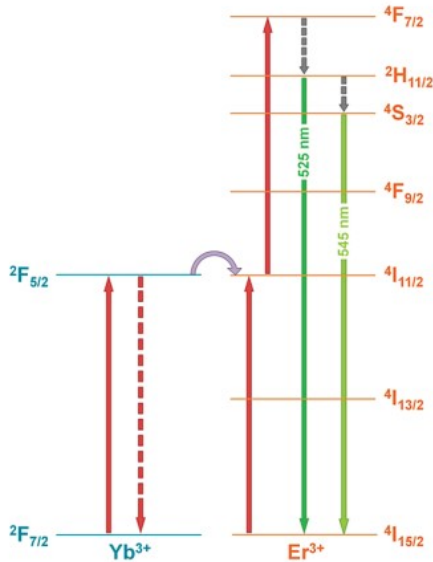
(a) Energy Transfer Upconversion leading to temperature sensitive green emissions in Er^{3+}. $\lambda_{excitation}$= 920nm
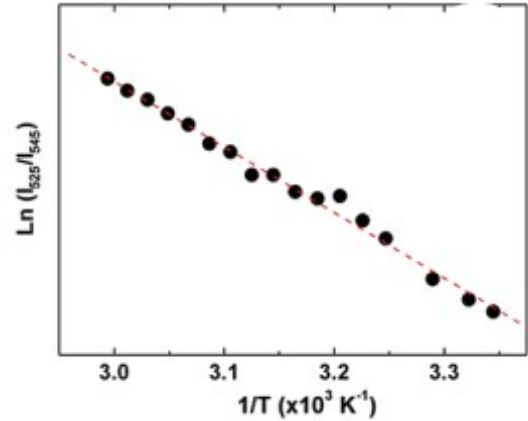
(b) Variation of $Ln(I_{525}/I_{545})$ as a function of 1/T (K^{-1})

Figure 1.8: Correlation between intensity ratio of the temperature sensitive emissions (I_{525}/I_{545}) and Temperature (K^{-1}). Adapted from [75].

cellular changes occurring as a result of external heating are monitored by means of transmission optical images of the illuminated cells at different temperatures as shown in figure 1.9. At room temperature 25 °C, the cancer cells show their characteristic irregular shape. Increasing the temperature to 35 °C does not produce any relevant changes in morphology. At 45 °C, cell death is detected due to the appearance of a small membrane fragment[75].

pH Sensing Photo-luminescent optical sensors for pH have attracted attention over the years considering they possess certain advantages over electrodes in that they do not require reference elements, they can be small, they enable contactless sensing and imaging, and they can be manufactured at reasonable costs. Using long wave pH sensors such as Lanthanide doped Lanthanum Oxide nanoparticles is of particular interest due to their functioning within the optical transparency window of biological tissues which exhibit strong intrinsic background luminescence in the UV and shortwave visible. One of the first reported instances of pH sensing using UCNPs includes $NaYF_4$:Er^{3+},Yb^{3+} upconversion nanorods which emit green and red emissions. The UCNPs are paired with a long wave absorbing pH probe (Bromothymol blue; BTB) that causes a pH-dependent inner filter effect. The UCNPs have a luminescence intensity that is independent of pH in the range from 2 to 11. When pairing the UCNPs with BTB, the emission of the UCNPS and the absorbance of BTB overlap; thus, depending on the pH dependant absorbance
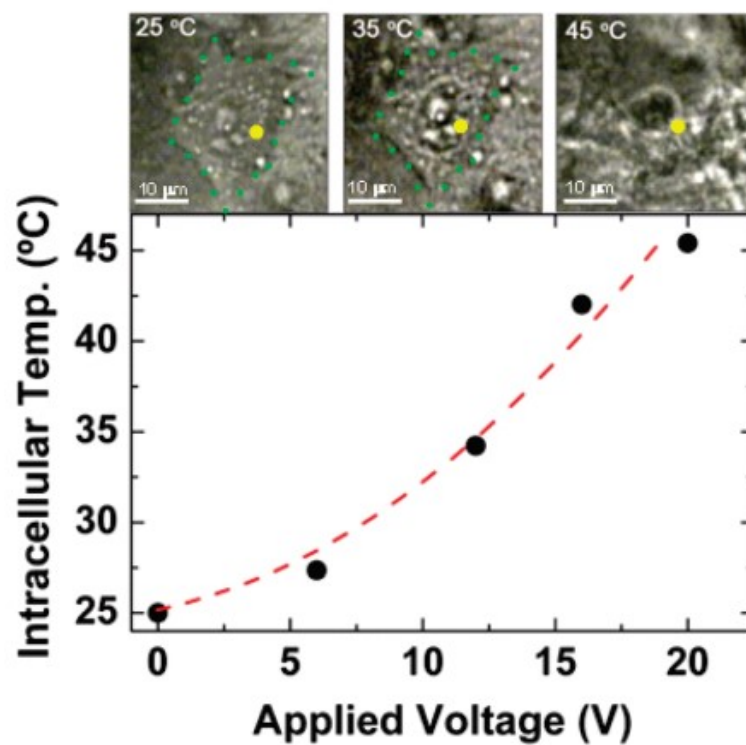
Figure 1.9: Optical transmission images of an individual Hela cell at 3 inner temperatures.(Bottom) Temperature of the Hela cell determined by the Er^{3+} ion fluorescence in the $NaYF_4$:Er^{3+},Yb^{3+} nanoparticles as a function of the applied voltage. Adapted from [75].

of BTB, the emission intensity of the UCNPs is altered. The pH probe generally undergoes a large spectral shift and distinct colour change with pH where it's color changes from yellow at pH=6 to blue at pH=8. When light is emitted by UCNPs, it is screened by a pH sensitive film made of BTB whose color depends on pH. When the dye is in it's blue base form, the absorbance of the film between 510 and 700 nm is strong, and the emission of the UCNPs is filtered off as shown in figure 1.10. At low pH, the absorbance of the film between 510 and 700 nm is weak and most of the light emitted by the UCNPs is detected [82]–[87]. This is the first optical pH sensor based on upconversion luminescence. Similar sensors can be employed in the detection of acidic gases such as CO_2 or basic gases such as NH_3 considering these gases can be quantified based on the pH of the medium. A CO_2 optical sensor utilizing the $NaYF_4$:Yb^{3+}/Er^{3+} UCNPs, that can be excited with 980 nm laser light to give green and red luminescence, in combination with a long wavelength absorption pH probe bromothymol blue (BTB) can be used for CO_2 detection with a LOD of about 0.11 % CO_2. The higher acidity of the medium which signifies a higher level of dissolved CO_2 corresponds to a higher signal intensity by the UCNPs due the lower absorbance of BTB in more acidic media[88]–[91]. Similarly, $NaYF_4$:Yb^{3+}/Er^{3+} UCNPs, excited with a 980 nm laser, used in combination with the pH probe phenol red immobilized in a polystyrene matrix can be used to detect ammonia. The presence of Ammonia, which is the equivalent of saying:"the higher the pH", causes a strong increase in the 560 nm absorption of the pH probe which, in turn, causes the green emission of the UCNPs to be screened off as shown in figure 1.11. The red emission of the UCNPs, in contrast, remains unaffected by ammonia and can serve as a reference signal[92], [93]. Optical pH sensors can also be used as enzymatic biosensors to monitor proton consumption in urease or proton production in glucose oxidase[94].

1.1.3.3   High Contrast Bio-imaging

Functioning within the optical transparency window of biological tissues (750-1100 nm) and having low cytotoxicity, Lanthanide doped materials are excellent candidates for imaging considering they allow for deeper light penetration, lower autofluorescence, and reduced light scattering compared to traditional imaging techniques.

Low cytotoxicity of Lanthanide doped nanoparticles is demonstrated in several cases including in-vivo toxicity in mice[95]–[97], worms[98]–[100], and zeebrafish embryos[101]. The results of these studies all indicate no obvious toxicity of UCNPs. In one instance, NIR emitting $NaYF_4$:Yb^{3+}/Tm^{3+} UCNPS coated with either polyethylene glycol (PEG) or polyacrylic acid (PAA) were intravenously injected into mice. Blood levels of UCNPs were measured, and Yttrium levels in various organs were measured to determine the bio-distribution of the UCNPs over 3 months. In this toxicology study, no noticeable toxic side effect was noticed for either UCNP-PAA or UCNP-PEG, despite the long-term retention of those nanoparticles in the reticulo-endothelial systems including the liver and spleen of mice. The results of this study and similar studies encourage future exploration of UCNPs for
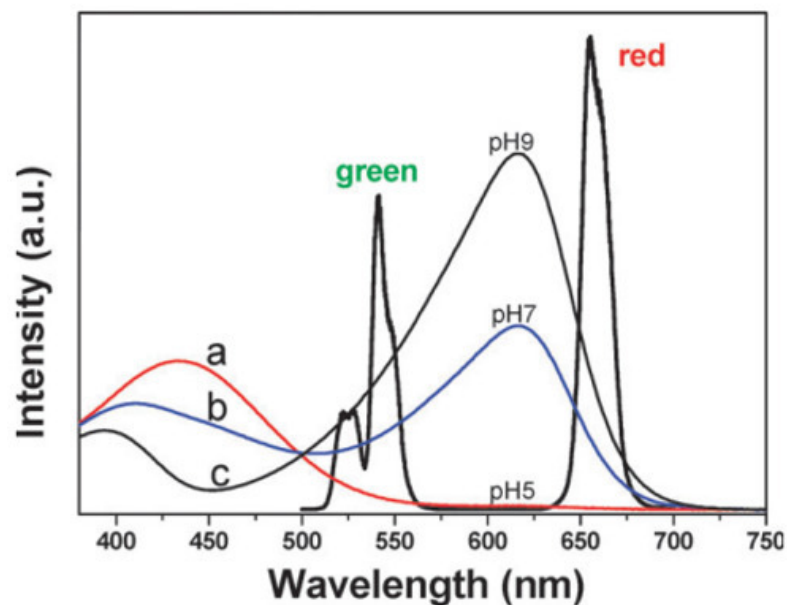
Figure 1.10: Absorption Spectra of BTB in aqueous solutions of pH 5,7,9, respectively (a,b,c); and luminescence emission (red and green) of the $NaYF_4:Er^{3+},Yb^{3+}$ nanorods in cyclohexane solution following photoexcitation with a 980-nm laser. Adapted from [82].
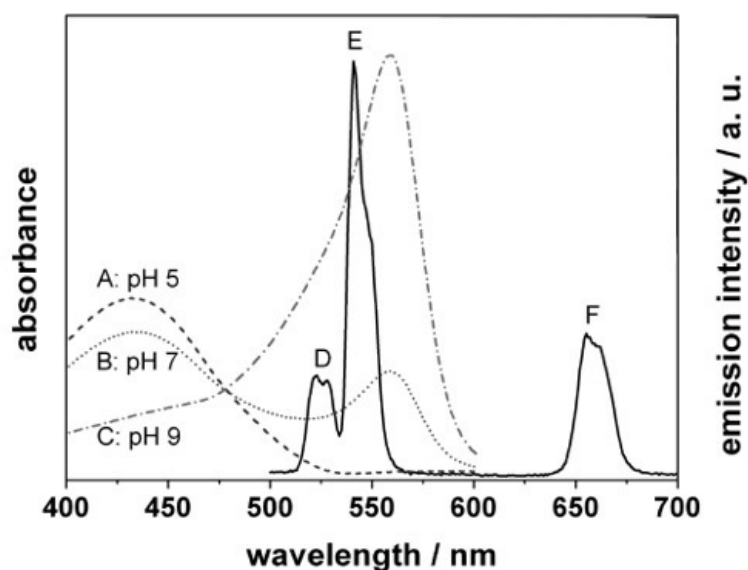
Figure 1.11: A, B, C: Absorption spectra of phenol red in aqueous solutions of pH 5, 7, and 9, respectively. D, E, F: Luminescence emission (green and red) of the upconverting nanoparticles in aqueous solution following 980 nm laser excitation. Adapted from [92].

in vivo biomedical applications.

High contrast Cellular imaging using NIR-to-visible (blue, green, red) and NIR-to-NIR UCNP has been an area of increasing interest in recent years. Non-functionalized UCNPs have been utilized to image a variety of cell lines through cellular endocytosis including breast cancer cells such as SK-BR-3 and MCF-7[102], HeLa cells[81], [103]–[106], NIH 3T3 mouse embryonic fibroblasts[93], ovarian cancer cells[107], AB12 mouse mesothelioma cells[108], Huh-7 liver cancer cells[109], MB49 bladder cancer cell lines[110], and Panc 1 cells[111]. Several instances of targeted imaging of tumor cells using UCNPs fictionalized with bio-molecular recognition moieties are also reported. For example, polyethyleneimine-coated $NaYF_4$:Yb^{3+},Er^{3+} UCNPs conjugated with folic acid were used to target human HT29 adenocarcinoma cells and human OVCAR3 ovarian carcinoma cells that have high levels of folate receptors on their cell surface[112]. In this case, the recognition moiety folic acid is used for for targeting folate receptors. UCNPs can also be conjugated with antibodies for targeting specific antigens. For instance, rabbit anti-CEA8 antibodies are conjugated with UCNPs for targeting carcinoembryonic antigen (CEA) on HeLa cells[113].

Passive Imaging using UCNPs under NIR laser diode excitations has enabled lymphatic imaging, high-resolution vascular imaging, multiplexed imaging, and real-time cellular trafficking. Local lymphatic drainage is an important route for the metastasis of cancer cells. This makes the identification and study of the sentinel lymph nodes important for cancer diagnostics and therapy. In one case, $NaYF_4$:Yb^{3+},Tm^{3+} UCNPs were successfully utilized for two-color imaging of mouse lymph nodes without going through any extensive post processing of the images[114]. In addition to lymphatic imaging, vascular imaging is extremely important considering changes in vascularization and vascular malfunction are associated with many diseases including cardiovascular and kidney diseases as well as various types of cancers. Vascular imaging allows the determination of the number and configurations of vessels, their permeability, and any functional abnormalities of the vessels. Lanthanide doped UCNPs Y_2O_3:Yb^{3+}, Er^{3+} coated with PEG polymer that minimizes nonspecific tissue binding and prolongs the circulation half-lives of the particles in the blood can be used for in vivo vascular imaging of nude mice[115] as shown in figure 1.12.

1.2 Reaction Diffusion Framework

Self organization is defined as the appearance of an array of organized structures repeated with defined or undefined symmetries that arise far from equilibrium without the intervention of external conditions[116]. Regulatory processes in cells, including cellular respiration, feedback loops, and other biochemical pathways, which govern the functioning of living beings are a product of self organization. Self organization is also seen in the nonlinear coupling between reaction and diffusion which induces
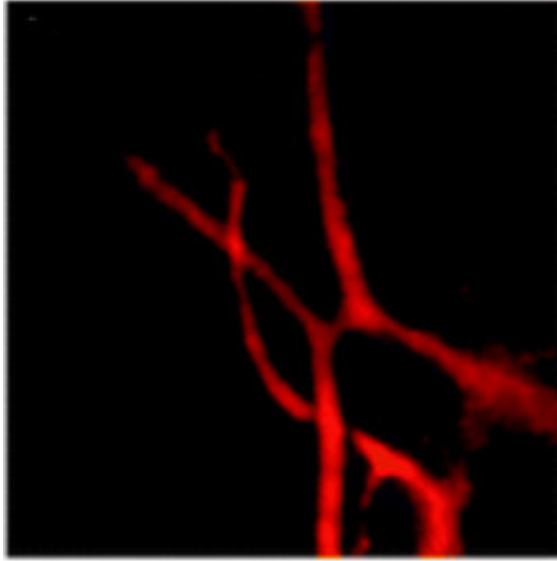
Figure 1.12: Upconversion image of Y_2O_3:Yb^{3+}, Er^{3+} nanoparticles in blood vessels in the mouse ear following tail vein injection at $\lambda_{excitation}$= 980 nm and laser power density of 550 mW $\cdot$ cm^{-2}. Adapted from [115].

chemical oscillations in space and time. Common structures originating from reaction diffusion include the iris banding of agate, the structure of cave stalactites, and the formation of dendritic structures on limestone[117].

The reaction-diffusion framework (RDF) is a system where an outer electrolyte is poured on top of an inner electrolyte embedded in a gel matrix. RDF starts with the conversion of the components via a chemical reaction and ends with their transportation in space via diffusion. The difference in the concentrations of the inner and outer electrolytes establishes a concentration gradient across the system. As the outer electrolyte diffuses through the gel, the reactants react to form a precipitate. Near the interface, supersaturation is highest and nucleation dominates. Further down the tube, supersaturation is lower and growth dominates. The nonlinear interaction of the diffusing supersaturation gradient with nucleation and crystal growth results in Liesegang instability where the resulting product organizes into a banding pattern of macroscopic periodic precipitation. Each band contains particles of uniform size and morphology[118].

1.2.1 *Theories governing the Liesegang banding phenomenon*

Two theories are mainly used to explain Liesegang banding, the pre-nucleation theory, based on the Ostwald's supersaturation theory [119]–[121], and the post-nucleation theory based on the Ostwald's ripening[122].

1.2.1.1 Ostwald's supersaturation theory

The Ostwald supersaturation-nucleation-depletion cycle explains periodic precipitation as a non-equilibrium process. The first precipitation bands do not appear

immediately upon the diffusion of the outer electrolyte into the gel, rather they appear after the supersaturation of the solution. The cycle begins with nucleation and growth of the particles in a specific region being accompanied by depletion of the electrolytes in the surrounding region. Consequently, the solubility product of the inner and outer electrolytes in the surrounding region decreases and nucleation is inhibited there. Diffusion of the outer electrolyte continues until supersaturation occurs again, thus allowing the formation of a new band. The repetition of this cycle leads to an alternative precipitation of filled and void domains[123].

1.2.1.2   Ostwald's ripening

Ostwald ripening theory is based on the formation of the product after a competition between particles of different sizes occurs. In order to decrease the energy of the system, smaller particles are dissolved and bigger particles are formed. The periodic precipitation is explained as a mechanism of the aggregation of big particles, leaving depleted clear zones of smaller particles in the surrounding regions[124], [125].

1.3   Aim of our Work

Synthesis of lanthanide doped materials via the most common routes posed drawbacks in terms of practicality, cost, and final product characteristics. Ideally, a convenient synthetic method should be adopted to synthesize lanthanide doped nanoparticles with controlled morphology, mono-dispersity, high crystallinity, and high photoluminescence efficiency. In our study we aim to synthesize lanthanide doped lanthanum oxide microspheres using the reaction diffusion framework (RDF) in order to obtain mono-dispersed crystalline micro particles and to bypass the need for high temperature, high pressure, toxic byproducts, and organic solvents[3]. The first step of the synthesis involves production of lanthanide doped lanthanum hydroxide microspheres by self-assembly in RDF which consists of diffusing an outer ammonia solution into a hydrogel matrix containing lanthanum ions as well as small percentages of lanthanide dopants such as europium, erbium, samarium, or terbium. The diffusion controlled reaction results in the formation of solid-containing lanthanum hydroxide bands. Because the reacting components are initially separated and poured one on top of the other, a gradient of supersaturation is obtained starting at the gel–solution interface and extending down the tube. Near the interface, supersaturation is high and nucleation dominates; this translates to having smaller particles. Down the tube, the gradient decreases and growth dominates. This translates to spheres increasing in size as we move away from the interface[1], [2]. As a result, each region of the tube will display a particular size range for the doped lanthanides, and thus the gradient of supersaturation translates to a gradient of sizes.

Following the synthesis of lanthanide doped lanthanum hydroxide microspheres, lanthanide doped lanthanum oxide microspheres are obtained by oxidizing the hydroxides in a furnace oven. Ln^{3+} doped $La(OH)_3$ microspheres undergo the following calcination reaction[20]:

$\text{La(OH)}_3 \rightarrow \text{LaOOH} + \text{H}_2\text{O}$

$2\,\text{LaOOH} \rightarrow \text{La}_2\text{O}_3$
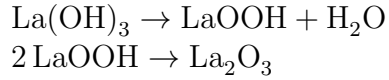
In order to precipitate La(OH)_3 micro-spheres, the RDF system is left to run for 4-5 days. During this time the radial size of the spheres in each region of the tube gradually increases while the outer ammonia solution is still diffusing through the tube. To better understand the growth mechanism of the spheres, growth of the spheres in different regions of the tube is measured under optical microscope, and radial size as a function of time is studied.

In the next part of our study, we aim to use synthesized Er^{3+} doped La_2O_3 for thermometry considering the photo-luminescence emission intensity ratio of Er^{3+} ions at 523 nm from the $^2H_{11/2} \rightarrow {}^4I_{15/2}$ transition and at 546 nm from the $^4S_{3/2} \rightarrow {}^4I_{15/2}$ transition is very sensitive to temperature. As the temperature increases from 22^oC to 60^oC, the intensity ratio $\frac{I_{523}}{I_{546}}$ also increases. $\ln(\frac{I_{523}}{I_{546}})$ varies linearly as a function of T^{-1}, thus a thermometric scale capable of evaluating temperature in an aqueous medium is obtained.

CHAPTER 2

MATERIALS AND METHODS

2.1 Materials

Lanthanum Nitrate Hexahydrate ($La(NO_3)_3 \cdot 6\,H_2O$, 99%) was purchased from BDH and from Baker Chemical Co, Europium Nitrate ($Eu(NO_3)_3$, 5N), and Erbium Nitrate ($Er(NO_3)_3$, 3N) from Chemicals 101 Corp, Lanthanum Chloride Heptahydrate ($LaCl_3 \cdot 7\,H_2O$, 98%) and Samarium Chloride Trihydrate ($SmCl_3 \cdot 3\,H_2o$) from BDH, Terbium Nitrate Hexahydrate ($Tb(NO_3)_3 \cdot 6\,H_2O$, 99.9%) from Thermo Scientific, Ammonium Hydroxide Solution ($25\%NH_3$) from sigma-aldrich, and Bacto agar gel from BD Chemicals.

2.2 Preparation of Ln^{3+} Doped Lanthanum Oxide using a Reaction Diffusion Framework (RDF)

The reaction diffusion framework (RDF) synthesis of Ln^{3+} doped La_2O_3 has enabled the synthesis of spherical, monodispered, crystalline microparticles with high photoluminescence efficiency. Our optimized synthesis procedure is based on the diffusion of a basic outer electrolyte 14 M Ammonia solution into a gel matrix containing 50 mM $Ln(NO_3)_3$ or $LnCl_3$ (where Ln= La^{3+}, Eu^{3+}, Er^{3+}, Sm^{3+}, or Tb^{3+}) which constitute the inner electrolyte as shown in figure 2.1. Using a 50 mM inner electrolyte, 14 M outer electrolyte came after a series of optimization trials which allowed us to identify which conditions enabled the synthesis of the most functional products. In order to allow diffusion, the concentration of the outer electrolyte is significantly greater than that of the inner electrolyte. After the precipitation of spherical $La(OH)_3$ micro-particles, different regions along the tube are extracted, washed, and centrifuged. The powder is then dried overnight in the vacuum oven and placed in the furnace at 800ºC for 3 hours to oxidize the Ln^{3+} doped $La(OH)_3$ to Ln^{3+} doped La_2O_3. The newly formed powder is pure La_2O_3. In order to prevent the La_2O_3 powder from reverting back to $La(OH)_3$, the La_2O_3 must be kept under inert atmosphere.
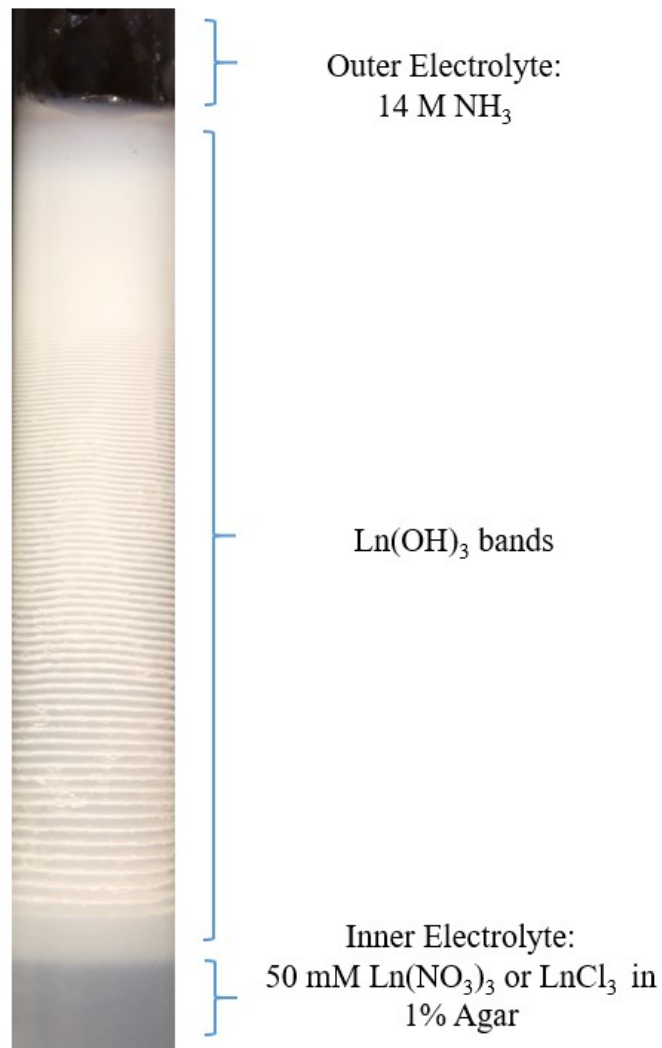
Figure 2.1: Reaction Diffusion Framework setup used to synthesize $La(OH)_3$ doped with Eu^{3+}, Er^{3+}, Sm^{3+}, Tb^{3+}, or a mixture of Tb^{3+} and Eu^{3+}. Preparation included pouring a 14 M outer electrolyte onto a 50mM inner Electrolyte comprising $Ln(NO_3)_3$ or $LnCl_3$ (where Ln= La^{3+}, Eu^{3+}, Er^{3+}, Sm^{3+}, or Tb^{3+}). The inner electrolyte is embedded in a 1 % agar gelatin matrix.

2.2.1 Samples prepared with 50 mM optimized inner electrolyte concentration

All samples discussed below are prepared using the same procedure. The only distinguishing factor is the inner electrolyte added.

2.2.1.1 La_2O_3 Control

A 1% agar solution is prepared by weighing out 0.02g of Agar and pouring them into 20 ml of double distilled water. The solution is placed in the microwave for 30-40 seconds for the agar to dissolve in the water. Proper dissolution is achieved when the color of the solution is translucent. 0.433 g of $La(NO_3)_3 \cdot 6\,H_2O$ powder are also weighed and added to the 20 ml solution to generate a 50 mM $La(NO_3)_3$ solution embedded in a 1% agar matrix. After proper mixing of solution, the homogeneous solution is transferred into a Pyrex test tube and kept at room temperature until gelation. Once gelation has taken place, 14M NH_3 is added on the top of the gel and left to allow the precipitation coupled with the diffusion. After 5 days of diffusion, white bands of pure $La(OH)_3$ are formed. The precipitate is extracted with a spatula, washed in double distilled at high temperature to remove the gel, and then dried for at least 10 hours in a 50 °C vacuum oven. The newly washed $La(OH)_3$ is transferred to a glass ceramic and placed in a furnace where it's temperature is brought from 25 °C to 800°C over a period of 5 hours. The powder is kept at 800°C for 3 hours, and then brought back to room temperature over a period of 5 hours.

Sample calculation for the mass (g) of $La(NO_3)_3 \cdot 6\,H_2O$ inner electrolyte added to the 1% agar gel (V is the volume of the solution in liters, M is the molar mass in g/mol):

$$m(g) = [La(NO_3)_3](M) \cdot V(l) \cdot M(La(NO_3)_3)(g/mol)$$

$$m(g) = 0.05(M) \cdot 0.02(l) \cdot 433.02(g/mol) = 0.433g$$

2.2.1.2 Eu^{3+} doped La_2O_3

Eu^{3+} doped La_2O_3 is prepared similarly to the control La_2O_3 with the same outer solution of Ammonia; however, the 50 mM inner electrolyte solution consists of $Eu(NO_3)_3$ and $La(NO_3)_3$. The masses that should be added of each substituent depend on the final inner electrolyte composition needed as shown in table 2.1. The solution initially prepared with 2% $Eu(NO_3)_3$ and 98% $La(NO_3)_3$ consists of 1 mM $Eu(NO_3)_3$ and 49 mM $La(NO_3)_3$. After the agar is fully dissolved in double distilled water, 0.0086 g of $Eu(NO_3)_3$ and 0.424 g of $La(NO_3)_3$ are added to the 20 ml solution. After gelation, the 14M NH_3 solution is left to diffuse through the tube for 5 days. The resulting Eu^{3+} doped $La(OH)_3$ precipitate is washed, oxidized, and used for further characterization.

2.2.1.3 Er^{3+} doped La_2O_3

Er^{3+} Doped La_2O_3 is prepared similarly to the control La_2O_3 with the same outer solution of Ammonia. The inner electrolyte powder samples used to create inner

Inner Electrolyte composition	m(g) La(NO$_3$)$_3$	m(g) Eu(NO$_3$)$_3$
98% La(NO$_3$)$_3$, 2% Eu(NO$_3$)$_3$	0.424	0.0086
94% La(NO$_3$)$_3$, 6% Eu(NO$_3$)$_3$	0.407	0.0257

Table 2.1: 50 mM inner electrolyte compositions for Eu^{3+} doped La(OH)$_3$ synthesis.

Inner Electrolyte composition	m(g) La(NO$_3$)$_3$	m(g) Er(NO$_3$)$_3$
96% La(NO$_3$)$_3$, 4% Er(NO$_3$)$_3$	0.416	0.0177
94% La(NO$_3$)$_3$, 6% Er(NO$_3$)$_3$	0.407	0.0266

Table 2.2: 50 mM inner electrolyte compositions for Er^{3+} doped La(OH)$_3$ synthesis

electrolytes having different compositions, as shown in table 2.2, are each added to the agar solution before gelation.

2.2.1.4   Sm^{3+} doped La$_2$O$_3$

Sm^{3+} doped La$_2$O$_3$ synthesis follows the same procedure. The inner electrolyte powder samples used to create inner electrolytes having different compositions, as shown in table 2.3, are each added to the agar solution before gelation.

2.2.1.5   Tb^{3+} doped La$_2$O$_3$

Tb^{3+} doped La$_2$O$_3$ is initially prepared with an inner electrolyte composed of 4% TbCl$_3$ and 96% La(NO$_3$)$_3$. 0.0149 g of TbCl$_3$ and 0.416 g of La(NO$_3$)$_3$ are weighed and added to the 20 ml 1% agar solution.

2.2.1.6   Eu^{3+},Tb^{3+} co-doped La$_2$O$_3$

La$_2$O$_3$: Eu^{3+},Tb^{3+} is prepared using the same procedure. The first trial included an

Inner Electrolyte composition	m(g) LaCl$_3$	m(g) SmCl$_3$
98% LaCl$_3$, 2% SmCl$_3$	0.364	0.0062
95% LaCl$_3$, 5% SmCl$_3$	0.353	0.0155
92.5% LaCl$_3$, 7.5% SmCl$_3$	0.344	0.0233

Table 2.3: 50 mM inner electrolyte compositions for Sm^{3+} doped La(OH)$_3$ synthesis.

Inner Electrolyte composition	m(g) La(NO$_3$)$_3$	m(g)TbCl$_3$	m(g) Eu(NO$_3$)$_3$
96% La(NO$_3$)$_3$, 2% TbCl$_3$, 2% Eu(NO$_3$)$_3$	0.416	0.0075	0.0086
95% La(NO$_3$)$_3$, 2% TbCl$_3$, 3% Eu(NO$_3$)$_3$	0.411	0.0075	0.0128
94% La(NO$_3$)$_3$, 4% TbCl$_3$, 3% Eu(NO$_3$)$_3$	0.407	0.0149	0.0128
91% La(NO$_3$)$_3$, 6% TbCl$_3$, 3% Eu(NO$_3$)$_3$	0.394	0.0224	0.0128
93% La(NO$_3$)$_3$, 2% TbCl$_3$, 5% Eu(NO$_3$)$_3$	0.403	0.0075	0.0214
91% La(NO$_3$)$_3$, 4% TbCl$_3$, 5% Eu(NO$_3$)$_3$	0.394	0.0149	0.0214
89% La(NO$_3$)$_3$, 6% TbCl$_3$, 5% Eu(NO$_3$)$_3$	0.385	0.0224	0.0214

Table 2.4: 50 mM inner electrolyte compositions for Tb^{3+}, Eu^{3+} codoped La(OH)$_3$ synthesis.

inner electrolyte composed of 2% TbCl$_3$, 2% Eu(NO$_3$)$_3$ and 96% La(NO$_3$)$_3$. 0.0075 g of TbCl$_3$, 0.0086 g of Eu(NO$_3$)$_3$ and 0.416 g of La(NO$_3$)$_3$ are weighed and added to the 20 ml 1% agar solution. Afterwards, several trials were done to optimize the inner electrolyte solution composition to give microspheres with optimum luminescence intensity. Different inner electrolyte solution compositions used in each trial are shown in table 2.4.

2.2.2 *Optimization*

Deciding to use a 50 mM inner electrolyte, 14 M NH$_3$ outer electrolyte came after a set of trial experiments. The purpose of the trials was to get Ln^{3+} doped La$_2$O$_3$ with spherical morphology and optimum luminescence efficiency. The optimization steps taken are discussed below.

2.2.2.1 200 mM Inner Electrolyte

The first attempt at using RDF to synthesize the La$_2$O$_3$ phosphors included using an inner electrolyte concentration of 200 mM Ln(NO$_3$)$_3$ where Ln^{3+}= La^{3+}, Eu^{3+} or

Inner Electrolyte composition	m(g) La(NO$_3$)$_3$	m(g) Ln(NO$_3$)$_3$
100% La(NO$_3$)$_3$	1.73	0
99.5% La(NO$_3$)$_3$, 0.5% Eu(NO$_3$)$_3$	1.72	0.0086
99% La(NO$_3$)$_3$, 1% Eu(NO$_3$)$_3$	1.71	0.017
98% La(NO$_3$)$_3$, 2% Eu(NO$_3$)$_3$	1.70	0.034
96% La(NO$_3$)$_3$, 4% Eu(NO$_3$)$_3$	1.66	0.068
94% La(NO$_3$)$_3$, 6% Eu(NO$_3$)$_3$	1.63	0.103
92% La(NO$_3$)$_3$, 8% Eu(NO$_3$)$_3$	1.59	0.137
98% La(NO$_3$)$_3$, 2% Er(NO$_3$)$_3$	1.70	0.035
96% La(NO$_3$)$_3$, 4% Er(NO$_3$)$_3$	1.66	0.071
94% La(NO$_3$)$_3$, 6% Er(NO$_3$)$_3$	1.63	0.106
92% La(NO$_3$)$_3$, 8% Er(NO$_3$)$_3$	1.59	0.142

Table 2.5: 200 mM inner electrolyte compositions for Eu^{3+} or Er^{3+} doped La(OH)$_3$ synthesis.

Er^{3+}. The different inner electrolyte compositions are tabulated in 2.5. During this attempt, Leisegang banding was very pronounced macroscopically as shown in 2.2. The spacing between the bands decreased and the bands became more more ordered as % dopant increased. The main drawback of this condition is the morphology of the La(OH)$_3$ precipitate produced was not spherical as % dopant added exceeded 1%; instead the particles resembled platelets. The luminescence intensity for the Eu^{3+} doped samples increased as the %Eu^{3+} increased; however, the luminescence intensity for the Er^{3+} doped samples was extremely low when using a 200 mM inner electrolyte. Further optimization was required to increase luminescence intensity of the final product while maintaining the spherical morphology of the Ln^{3+} doped La(OH)$_3$ particles.

2.2.2.2 3.5 M Outer Electrolyte

During the second attempt to synthesize La$_2$O$_3$ phosphors using RDF, a 3.5 M NH$_3$ outer electrolyte was added to a 200 mM inner electrolyte. The compositions of the inner electrolyte solutions was 100% La(NO$_3$)$_3$ in the first tube or 98% La(NO$_3$)$_3$, 2% Eu(NO$_3$)$_3$ in the second tube. The final Ln^{3+} doped La$_2$O$_3$ product did not show
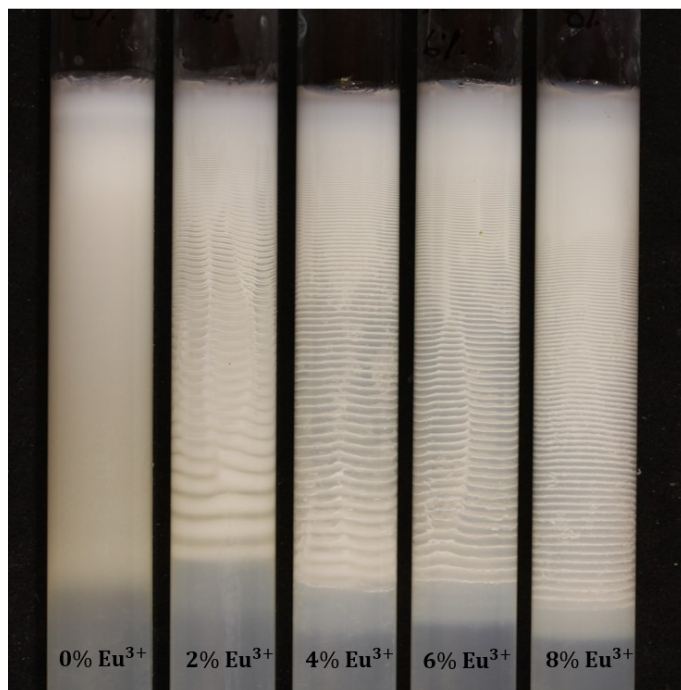
(a) La$_2$O$_3$ prepared with a 200 mM inner electrolyte consisting of Ln(NO$_3$)$_3$ where Ln^{3+} = La^{3+} and Eu^{3+}
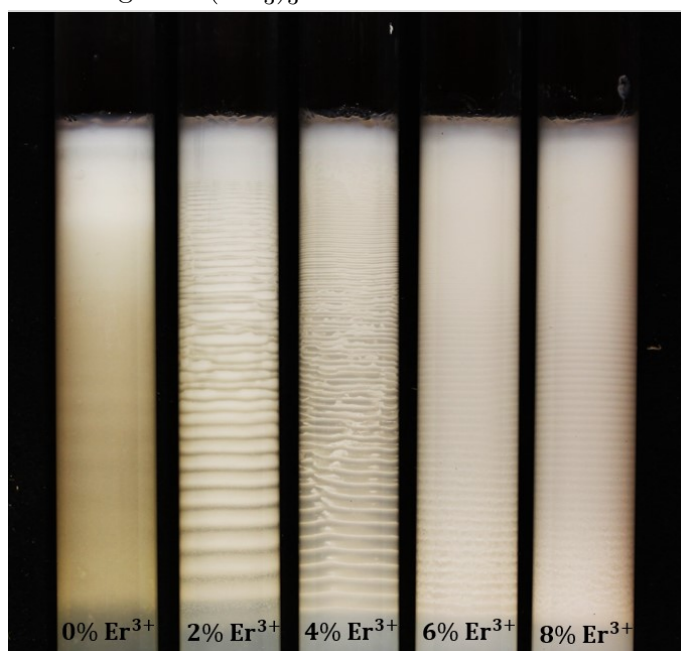
(b) La$_2$O$_3$ prepared with a 200 mM inner electrolyte consisting of Ln(NO$_3$)$_3$ where Ln^{3+} = La^{3+} and Er^{3+}

Figure 2.2: Macroscopic Leisegang Banding pattern in samples prepared with a 200mM Ln(NO$_3$)$_3$ inner electrolyte.

Inner Electrolyte composition	Results
100% $Eu(NO_3)_3$	no new precipitate formed
100% $Er(NO_3)_3$	no new precipitate formed
100% $La(NO_3)_3$	$La(OH)_3$ microspheres formed
94% $La(NO_3)_3$, 6% $Eu(NO_3)_3$	Eu^{3+} doped $La(OH)_3$ microspheres formed
94% $La(NO_3)_3$, 6% $Er(NO_3)_3$	Er^{3+} doped $La(OH)_3$ microspheres formed

Table 2.6: 50 mM inner electrolyte compositions for the 1st trial.

any significant improvement compared to the products obtained from the first trial. The main result of this trial was that decreasing outer electrolyte concentration leads to the formation of larger spheres with lower luminescence intensity than the first trial.

2.2.2.3 50 mM Inner Electrolyte/ 14 M Outer Electrolyte

The best morphology and luminescence efficiency for the Ln^{3+} doped La_2O_3 micro-particles was obtained using a 50 mM inner electrolyte solution $Ln(NO_3)_3$ where $Ln^{3+}= La^{3+}$, Eu^{3+}, Er^{3+}, Sm^{3+}, or Tb^{3+}. Macroscopically, banding is not always visible using a 50 mM inner electrolyte; however, regions of spherical luminescent micro-particles are obtained under this condition. Different regions of each tube comprise monodisperesed spheres of a specific size with smaller spheres closer to the interface where nucleation dominates, and larger spheres farther away from the interface where growth dominates. Using a 50 mM inner electrolyte concentration instead of 200 mM leads to the overall production of smaller spheres in the RDF. This is a great advantage considering the decrease in final La_2O_3 product size is much more suitable for biological applications which require particles to be scaled in the nm range[22]. The first trial using a 50 mM inner electrolyte involved preparing 5 tubes with different inner electrolytes embedded in 1% agar as shown in figure 2.3. The results, tabulated in 2.6, lead all future study to be conducted on 50 mM inner electrolyte RDFs as shown in figure 2.4.

2.2.3   *300 mM Inner Electrolyte: Samples for growth experiment*

In order to study the growth of the spherical microparticles obtained using RDF, samples having 300 mM inner electrolyte concentration are prepared and left to run in a 1D glass tube shown in figure 2.5 for 2-3 days. The composition of the different inner electrolyte solutions are tabulated in 2.7. Considering the inner electrolyte concentration (300 mM) is higher than previous trials, the size of the spheres obtained is large enough for the growing spheres to be visible under an optical microscope at 10x10 magnification.
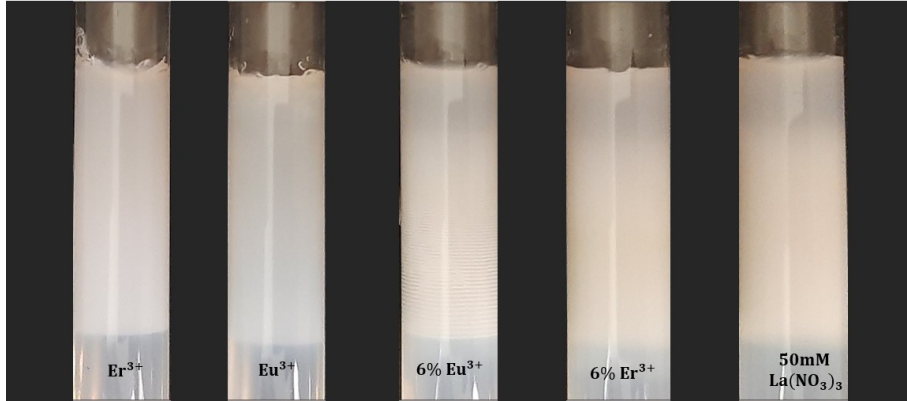
Figure 2.3: Trial 1: Samples prepared using a 50mM inner electrolyte.
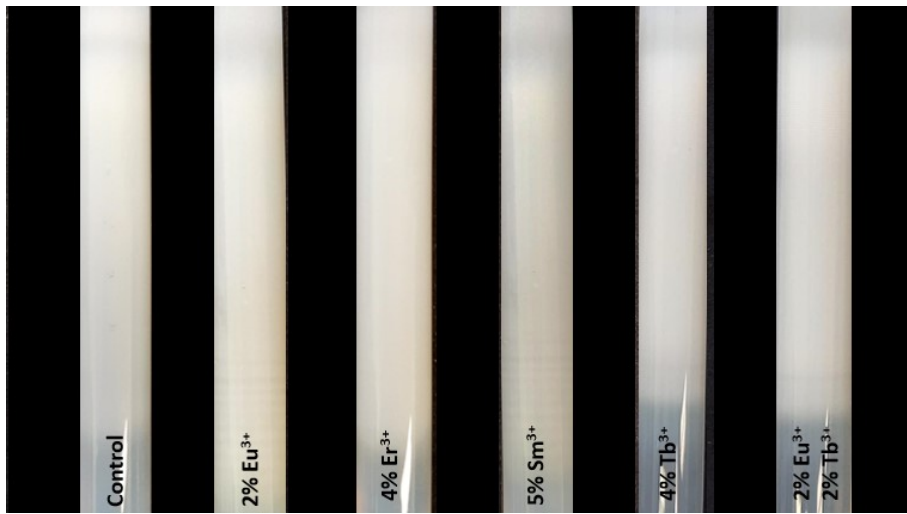
Figure 2.4: Ln^{3+} doped $La(OH)_3$ synthesized using a 50 mM $Ln(NO_3)_3$ inner electrolyte solution where $Ln^{3+}= La^{3+}$, Eu^{3+}, Er^{3+}, Sm^{3+}, or Tb^{3+}.

Inner Electrolyte composition	m(g) $La(NO_3)_3$	m(g) $Er(NO_3)_3$
100% $La(NO_3)_3$	2.60	0
96% $La(NO_3)_3$, 4% $Er(NO_3)_3$	1.66	0.0709

Table 2.7: 300 mM inner electrolyte compositions for growth study.

Figure 2.5: La(OH)$_3$ synthesis in a 1D tube using 300mM inner electrolyte.

2.3 Characterization of Lanthanide Doped lanthanum Oxide Microspheres

2.3.1 *Powder X-Ray diffraction (PXRD)*

Powder X-Ray diffraction (PXRD) allows for the identification of a powder sample characterized by a unique PXRD pattern. XRD enables crystalline phases to be identified,quantified, and their atomic structure determined– all with very little sample preparation. This prevents the risk of destroying the phases and/or modifying the characteristics of the sample. Powder X-Ray diffraction (PXRD) patterns are recorded on a Bruker D8 advance XRD diffractometer using CuKα radiation (λ=1.5406Å) at 40 kV and 40 mA, with 2θ ranging between 10° and 80°. The monochromator used is Johansson Type. The step size is 0.02 s and the scan rate is 20 s per step.

2.3.2 *Scanning Electron Microscopy Analysis (SEM)*

The morphology and the size of the particles in different regions of the tube are investigated using a scanning electron microscope (Tescan MIRA3 LMH Schottky FE-SEM), operating at 5 kV; and equipped with Oxford detector for energy dispersive X-ray (EDX) characterization at 15 kV. The EDX is used as a qualitative determinant for the presence of certain elements in our sample. The samples are coated with a 20 nm layer of gold prior to SEM using the sputtering machine Q150T PLUS Turbomolecular Pumped Coater.

2.3.3 *Brunauer-Emmett-Teller (BET) surface area analysis*

In order to analyze the surface area of the of the Ln^{3+} doped $La(OH)_3$ and La_2O_3 micropheres, nitrogen isotherms are carried on using a Micromeritics 3Flex Surface Characterization Analyzer. The BET surface area is calculated using NOVA 2200e surface area analyzer after degassing the samples for 6 hours at 80 °C under vacuum.

2.3.4 *Fourier Transform Infrared Spectroscopy FTIR*

The chemical structures of some products are characterized by FTIR spectroscopy. A Thermo Nicolet 4700 Fourier Transform Infrared Spectrometer equipped with a Class 1 Laser is used for this purpose. The KBr pellet technique is applied to perform the transmission experiments in the range between 4000 and 400 cm^{-1}. Raman spectra are recorded using a confocal micro-Raman spectrometer (Horiba Jobin Yvon/Labram Aramis) with an excitation wavelength of 473 nm. The experiments are carried out in the range between 100 and 1200 cm^{-1}. .

2.3.5 *DLS Dynamic Light Scattering*

The colloidal stability of Ln^{3+} doped $La(OH)_3$ and La_2O_3 micropheres is assessed by conducting zeta potential measurements using the Nanoplus HD zeta/nano particle analyzer (Particulate Systems). The NanoPlus also has the capability of measuring the zeta potential of sample suspensions in the -200 mV to +200 mV range with concentrations from 0.001% to 40%.

2.3.6 *Fluorometer*

Fluorescence measurements are performed on a 2-D slide containing the desired Lanthanide doped Lanthanum Oxide powder using Cary Eclipse Varian fluorescence spectrophotometer. The slide is placed vertically and the fluorescence emission spectrum is recorded in front surface or right angle geometry. The steadystate fluorescence emission measurements are documented with resolution increment 1 nm, slit 5 nm using a Jobin-Yvon-Horiba Fluorolog III fluorometer and the FluorEssence software. The excitation source is a 100 W Xenon lamp, and the detector used is the R-928 operating at a voltage of 950 V. In all the emission spectra collected, $\lambda_{excitation}$= 386 nm was applied. To observe the effect of temperature on the emission intensity of Er^{3+} doped samples, a circulator bath allows temperature regulation of the area surrounding a cuvette containing the powder sample immersed in liquid.

2.3.7 *Fluorescent Microscope*

Doped La_2O_3 Microspheres are observed using a DM6 B Microscope (Leica Microsystems) which allows the view of the photoluminescence of our samples using an RGB filter at $\lambda_{excitation}$= 390 - 410nm.

Chapter 3

SYNTHESIS AND CHARACTERIZATION OF LANTHANUM OXIDE PHOSPHORS

3.1   Introduction

Due to their wide array of applications in sensing and imaging, synthesizing Ln^{3+} doped oxides and fluorides have captured massive attention over the years. Numerous attempts have been made to achieve a cost effective practical synthesis method for Ln^{3+} doped particles having controlled morphology, mono-dispersity, high crystallinity, and high photoluminescence efficiency; the most representative methods being thermal decomposition, high temperature coprecipitation, and hydro(solvo)thermal synthesis. The reaction diffusion framework (RDF) has actually made such a synthesis procedure possible considering photoluminescent, highly crystalline, monodispered Ln^{3+} doped La_2O_3 microparticles are synthesized primarily at room temperature and pressure via a simple procedure that only requires 10-15 minutes of hands-on work. In the upcoming section, characterization of the La_2O_3 final product, synthesized using RDF, will be discussed using data collected from the scanning electron microscope (SEM), X-ray Diffractometer (XRD), Fourier Transform Infrared Spectrometer (FTIR), Brunauer-Emmett-Teller (BET) surface area analyzer, Dynamic Light Scattering (DLS), luminescence spectrometer, and Fluorescence microscope. Furthermore, anaylysis of the growth mechanism of the Ln^{3+} doped $La(OH)_3$ used to produce Ln^{3+} doped La_2O_3 phosphors is carried out under optical microscope to display radial growth as a function of time in different regions of the RDF system.

3.2 Results and Discussion

3.2.1 *Characterization of samples prepared with 50 mM optimized inner electrolyte concentration*

3.2.1.1 Powder X-Ray Diffraction of Lanthanide Doped Lanthanum Hydroxide and Lanthanide Doped Lanthanum Oxide Micro-spheres

The PXRD patterns of the obtained crystals before calcination (Ln^{3+} doped $La(OH)_3$) and after calcination (Ln^{3+} doped La_2O_3) are recorded and compared to the simulated pattern of pure $La_2(OH)_3$ in figure 3.1 and pure La_2O_3 in figure 3.2 respectively. The sharp peaks observed in the PXRD patterns of the collected white $La(OH)_3$ and La_2O_3 powder samples synthesized via RDF perfectly match the main peaks of the simulated pattern of pure hexagonal $La(OH)_3$[126] and pure hexagonal La_2O_3[127] respectively and no additional peaks are observed. This indicates the synthesized crystals are highly crystalline and pure.

3.2.1.2 Scanning Electron Microscopy Analysis

A tube of inner electrolyte $[Ln(NO_3)_3] = 50$ mM or $[LnCl_3]=50$mM embedded in 1% agar and outer electrolyte 14 M NH_3 is used to precipitate Ln^{3+} doped $La(OH)_3$. The system is kept at room temperature (25ºC) throughout the precipitation process. Scanning Electron Microscopy is used to examine the particle morphology of Ln^{3+} doped $La(OH)_3$ powder sample produced in several regions of each tube. SEM images of Ln^{3+} doped $La(OH)_3$ reveal that the particles are platelets in regions closer to the interface. At around 3.5 cm from the interface, particles begin to exhibit spherical morphology. An increase in the size of the spheres is observed as we move farther away from the interface which is expected considering nucleation dominates closer to the interface leading to the production of smaller particles, and growth dominates farther away from the interface leading to the production of larger particles. Ln^{3+} doped $La(OH)_3$ powder sample is collected from the tube, washed and oxidized to La_2O_3 using the furnace at 800ºC for 3 hours. SEM images of the oxidized samples reveal that particles retain their spherical morphology after oxidation. SEM images of samples prepared with different inner electrolyte compositions before and after calcination are represented below.

$La(OH)_3$ and La_2O_3 Control: The inner electrolyte of the control consists of 50 mM $La(NO_3)_3$ embedded in 1% agar solution. $La(OH)_3$ sample is collected from 5 different regions of the tube and observed using SEM as shown in figure 3.3. SEM images of the Oxide sample obtained after calcination are also taken. They show the spherical morphology of the $La(OH)_3$ crystals is retained after calcination as shown in 3.3.

Eu^{3+} doped $La(OH)_3$ and La_2O_3: The same precipitation, oxidation procedure was carried out on a tube containing an inner electrolyte composition of 2% $Eu(NO_3)_3$ and 98% $La(NO_3)_3$. Eu^{3+} doped $La(OH)_3$ sample is collected from 5
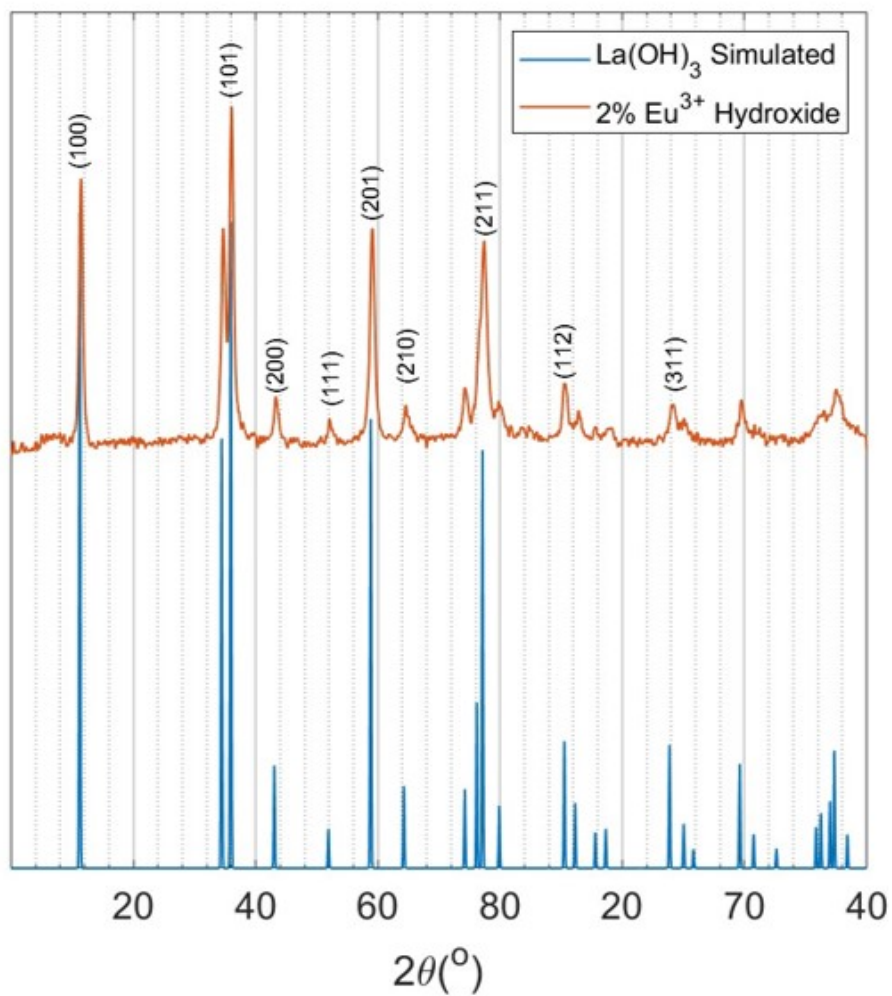
Figure 3.1: PXRD patterns of simulated La(OH)$_3$ crystals and Eu^{3+} doped La(OH)$_3$, prepared with inner electrolyte 2% Eu(NO$_3$)$_3$ 98% La(NO$_3$)$_3$, synthesized via RDF.
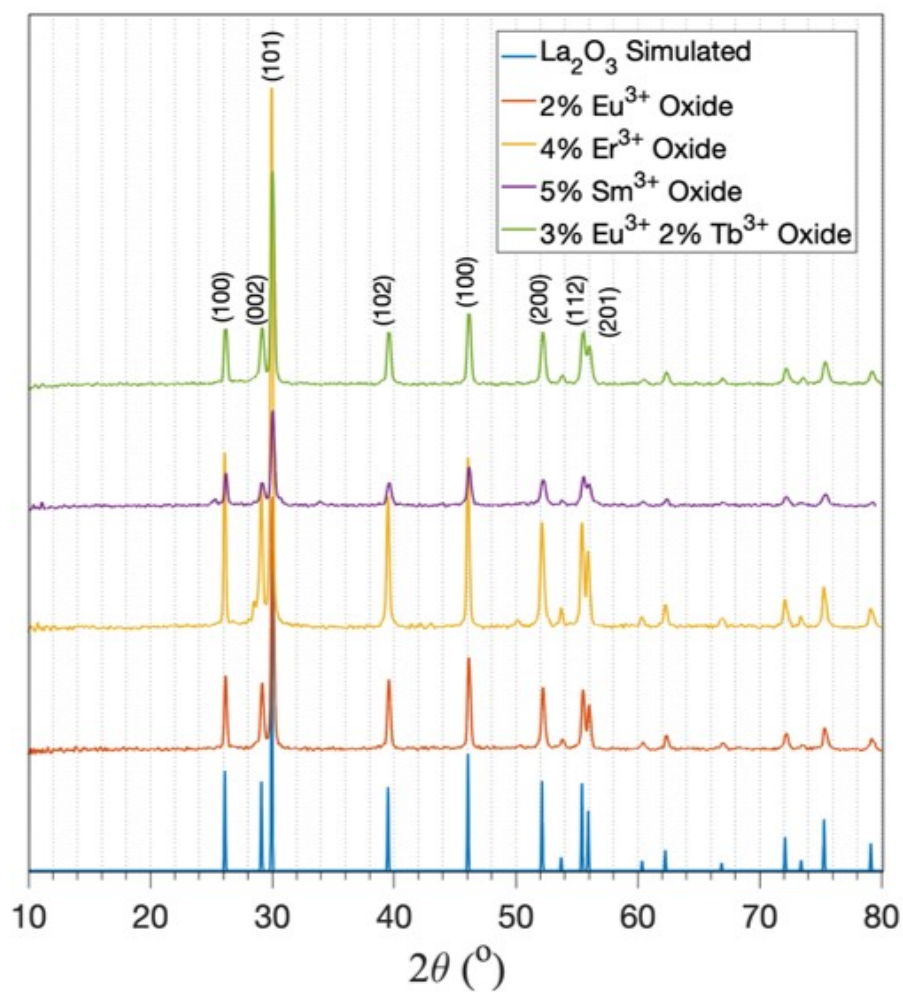
Figure 3.2: PXRD patterns of simulated La_2O_3 crystals and Ln^{3+} doped La_2O_3 ($Ln^{3+}=$ Eu^{3+}, Er^{3+}, Sm^{3+}, Tb^{3+}) synthesized via RDF using a 50 mM inner electrolyte.
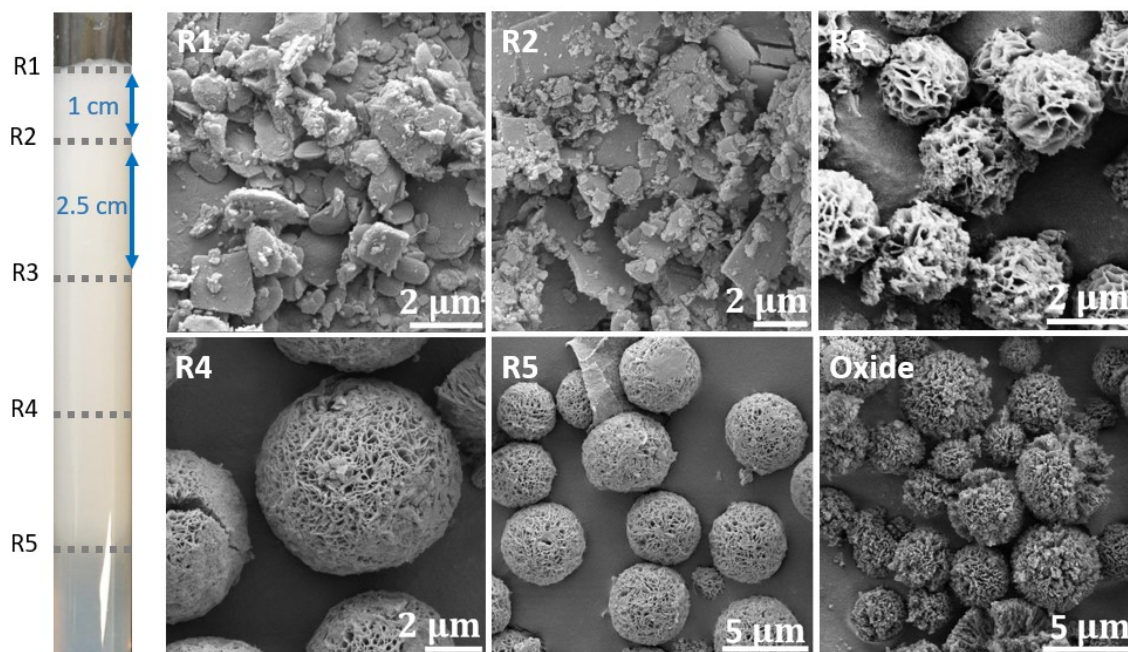
Figure 3.3: RDF used to synthesize La(OH)$_3$ microspheres using 50 mM La(NO$_3$)$_3$ embedded in 1% agar and 14M NH$_3$ outer electrolyte. (Bottom right) La$_2$O$_3$ microspheres obtained after calcination.

different regions of the tube and observed using SEM. SEMs of the corresponding spherical Eu^{3+} doped La$_2$O$_3$ were taken as shown in figure 3.4.

Er^{3+} doped La(OH)$_3$ and La$_2$O$_3$: The same precipitation, oxidation procedure was carried out on a tube containing an inner electrolyte composition of 4% Er(NO$_3$)$_3$ and 96% La(NO$_3$)$_3$. Er^{3+} doped La(OH)$_3$ sample is collected from 5 different regions of the tube and observed using SEM. SEMs of the corresponding Er^{3+} doped La$_2$O$_3$ microspheres are also taken as shown in figure 3.5.

Sm^{3+} doped La(OH)$_3$ and La$_2$O$_3$: The same precipitation, oxidation procedure was carried out on a tube containing an inner electrolyte composition of 5% SmCl$_3$ and 95% LaCl$_3$. Sm^{3+} doped La(OH)$_3$ sample is collected from 8 different regions of the tube and observed using SEM as shown in figure 3.6. SEMs of the corresponding Sm^{3+} doped La$_2$O$_3$ microspheres were taken as shown in figure 3.7.

Tb^{3+} doped La(OH)$_3$ and La$_2$O$_3$: The same precipitation, oxidation procedure was carried out on a tube containing an inner electrolyte composition of 4% TbCl$_3$ and 96% La(NO$_3$)$_3$. Tb^{3+} doped La(OH)$_3$ sample is collected from 5 different regions of the tube and observed using SEM. SEMs of the corresponding Tb^{3+} doped La$_2$O$_3$ microspheres were taken as well as shown in figure 3.8.

Figure 3.4: RDF used to synthesize Eu^{3+} doped La(OH)$_3$ microspheres using an inner electrolyte composition of 98% (49 mM) La(NO$_3$)$_3$ and 2% (1 mM) Eu(NO$_3$)$_3$ embedded in 1% agar and 14M NH$_3$ outer electrolyte. (Bottom right) Eu^{3+} doped La$_2$O$_3$ microspheres obtained after calcination.
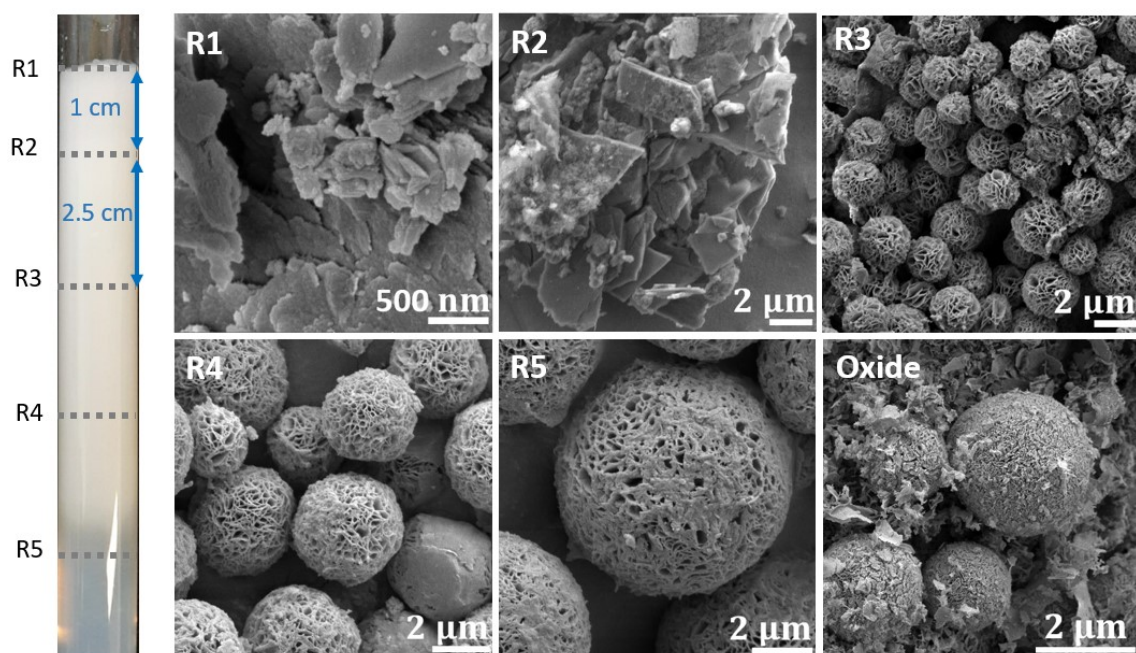
Figure 3.5: RDF used to synthesize Er^{3+} doped La(OH)$_3$ microspheres using an inner electrolyte composition of 96% (48 mM) La(NO$_3$)$_3$ and 4% (2 mM) Er(NO$_3$)$_3$ embedded in 1% agar and 14M NH$_3$ outer electrolyte. (Bottom right) Er^{3+} doped La$_2$O$_3$ microspheres obtained after calcination.
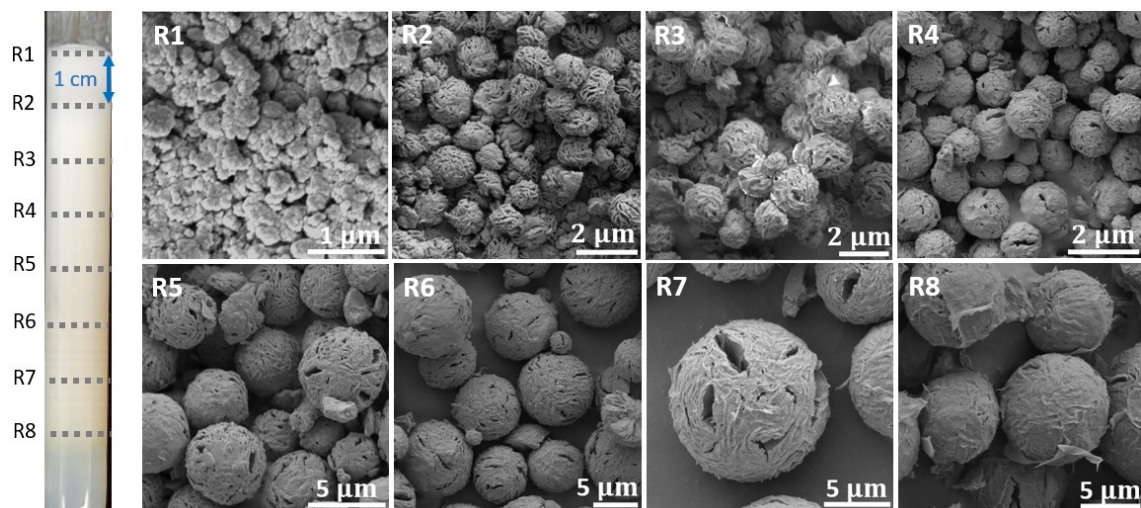
Figure 3.6: Sm^{3+} doped La(OH)$_3$ microspheres obtained via RDF using an inner electrolyte composition of 95% (47.5 mM) LaCl$_3$ and 5% (2.5 mM) SmCl$_3$ embedded in 1% agar and 14M NH$_3$ outer electrolyte.
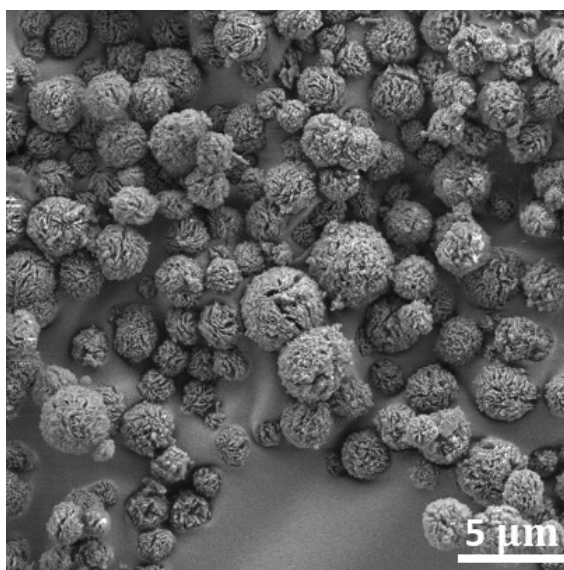
Figure 3.7: Sm^{3+} doped La$_2$O$_3$, synthesized using inner electrolyte composition 95% LaCl$_3$ and 5% SmCl$_3$, obtained after calcination.
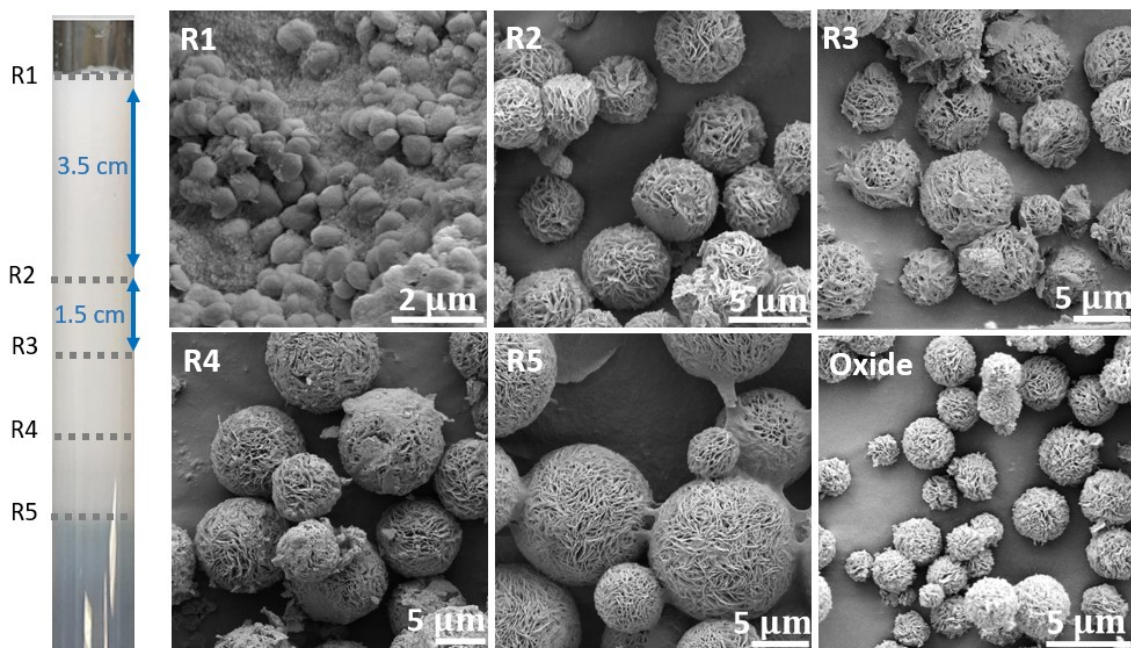
Figure 3.8: RDF used to synthesize Tb^{3+} doped $La(OH)_3$ microspheres using an inner electrolyte composition of 96% (48 mM) $La(NO_3)_3$ and 4% $TbCl_3$ (2 mM) $TbCl_3$ embedded in 1% agar and 14M NH_3 outer electrolyte. (Bottom right) Tb^{3+} doped La_2O_3 microspheres obtained after calcination.

Tb^{3+}, Eu^{3+} co-doped $La(OH)_3$ and La_2O_3: The same precipitation, oxidation procedure was carried out on a tube containing an inner electrolyte composition of 2% $TbCl_3$, 2% $Eu(NO_3)_3$, and 96% $La(NO_3)_3$. Tb^{3+}, Eu^{3+} co-doped $La(OH)_3$ sample is collected from 5 different regions of the tube and observed using SEM. SEMs of the corresponding Tb^{3+}, Eu^{3+} co-doped La_2O_3 micropsheres were also taken as shown in figure 3.9.

EDX measurements were initially conducted on samples during the 1st mentioned trial where 200 mM inner electrolyte was used. EDX served as a qualitative determinant of the presence of small percentages of lanthanide dopants in the final products. The overall trend observed from the EDX measurements is % dopant in the final product is less than the amount of dopant initially incorporated. For instance, samples synthesized with 2% $Eu(NO_3)_3$, 48% $La(NO_3)_3$ inner electrolyte composition will have a final %Eu^{3+} < 2 %. In some cases, % dopant is seen to be higher near the interface, however; no conclusive statements can be made due to the large error on the values obtained using EDX.

Effect of % dopant on particle morphology As % dopant increases, the recurrent trend indicates that the spherical morphology of the Ln^{3+} doped $La(OH)_3$ is destroyed; the morphology is rod-like instead. This shift is very apparent with Sm^{3+} doped $La(OH)_3$ prepared with an inner electrolyte composition of 7.5% $SmCl_3$ and 92.5% $LaCl_3$ embedded in 1% agar. At the region 4 cm from the interface, the
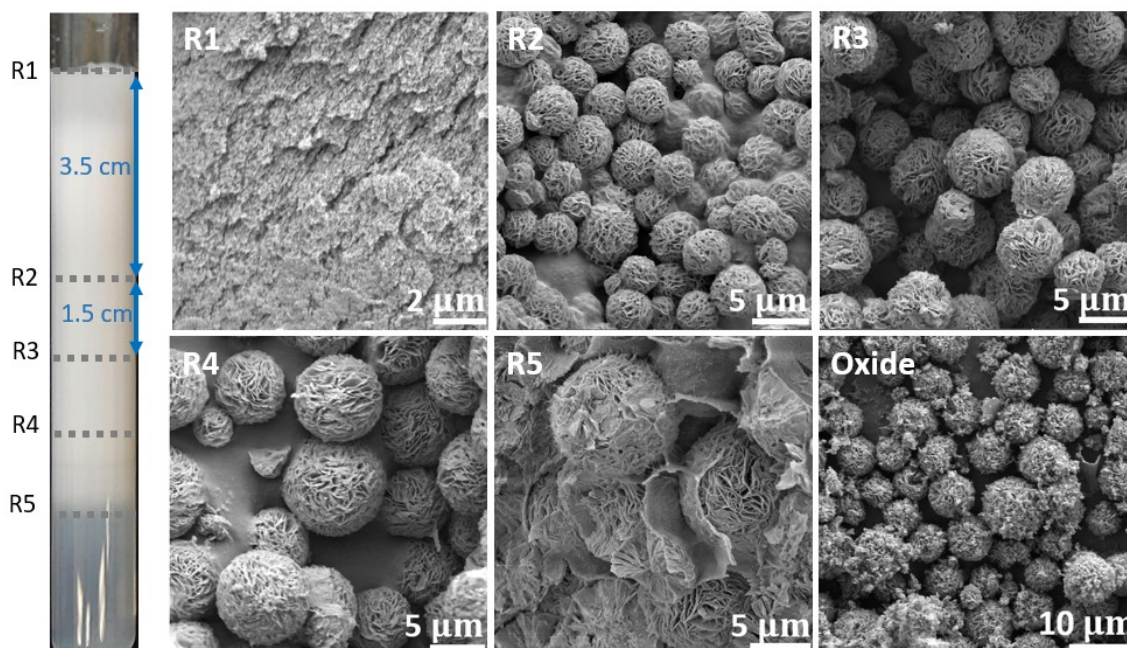
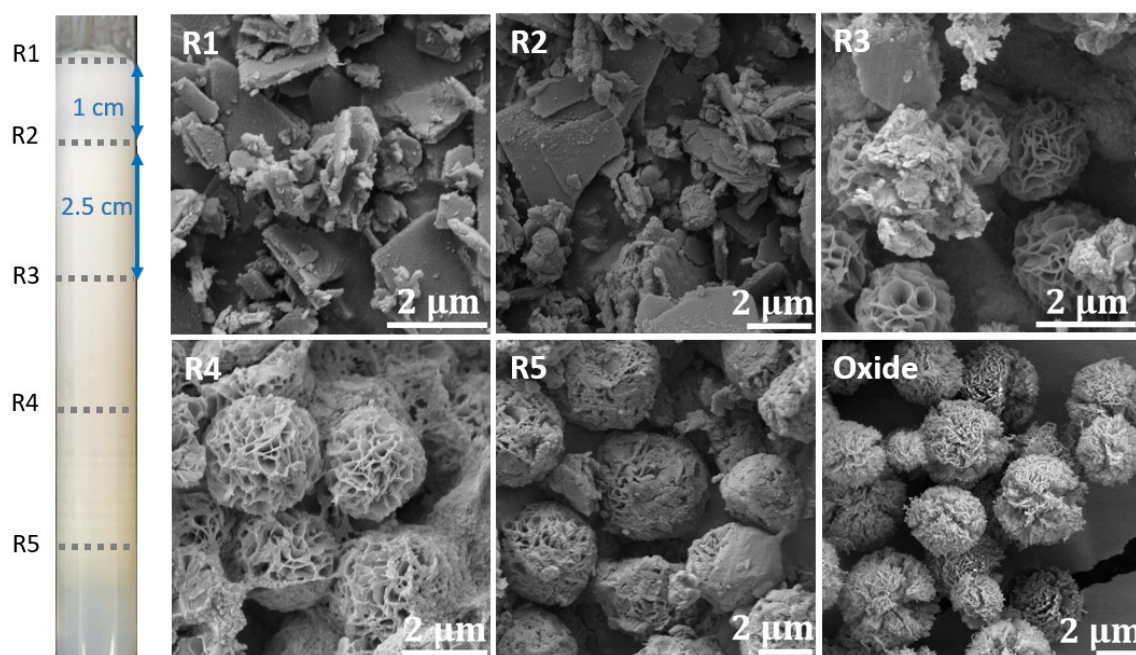Figure 3.9: RDF used to synthesize Eu^{3+}, Tb^{3+} co-doped $La(OH)_3$ microspheres using an inner electrolyte composition of 96% (48 mM) $La(NO_3)_3$, 2% (1 mM) $TbCl_3$, and 2% (1 mM) $Eu(NO_3)_3$ embedded in 1% agar and 14M NH_3 outer electrolyte. (Bottom right) Eu^{3+}, Tb^{3+} co-doped La_2O_3 microspheres obtained after calcination.

morphology shifts from spheres to platelets as shown in figure 3.10. When % $SmCl_3$ is lower, in the tube prepared with an inner electrolyte of 5% $SmCl_3$ and 95% $LaCl_3$ for example, the $La(OH)_3$ particles are spherical throughout the tube as shown in figure 3.6.

3.2.1.3   Luminesence Spectroscopy

In order to check the luminescence of the Ln^{3+} doped La_2O_3 microspheres, different powder samples are placed in the fluorometer to obtain their luminescence emission spectrum. The narrow sharp well defined characteristic peaks of the Lanthanide dopants are clearly visible, thus confirming the success of this novel synthesis method for Ln^{3+} doped La_2O_3 microparticle synthesis. In order to see if concentration quenching occurs when using different dopants, luminescence intensity for each transition is plotted as a function of % Ln^{3+}. It should be noted that luminescence efficiency is subject to change depending on the concentration of inner electrolyte. Some samples were luminescent when using a 50 mM inner electrolyte and not luminescent when using a 200 mM inner electrolyte solution with the same constituent proportions. Optimization is key while finding the correct synthesis procedure.

Eu^{3+} doped La_2O_3: Eu^{3+} luminescence, characterized by emissions at 590 nm, 610 nm, and 720 nm, is evident in Eu^{3+} doped La_2O_3, synthesized with an inner electrolyte composition of 2% or 6% $Eu(NO_3)_3$, as shown in figure 3.11 (a). When
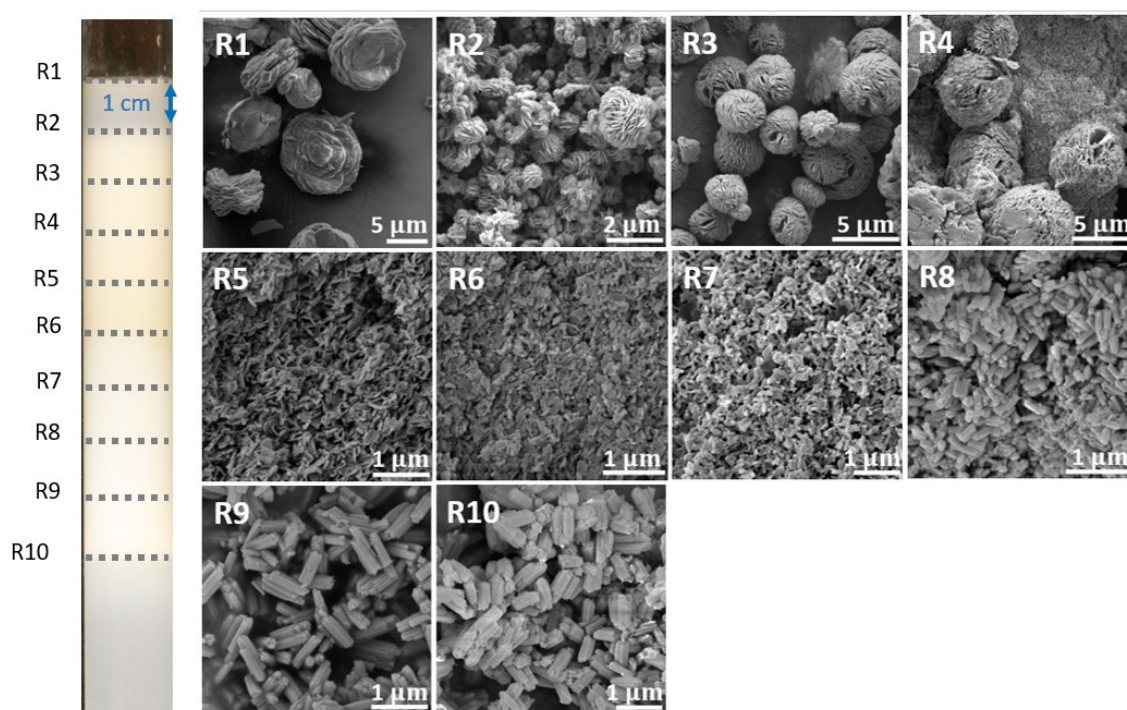
Figure 3.10: Sm^{3+} doped $La(OH)_3$ obtained via RDF using an inner electrolyte composition of 92.5% (46.25 mM) $LaCl_3$ and 7.5% (3.75 mM) $SmCl_3$ embedded in 1% agar and 14M NH_3 outer electrolyte. There is a shift in morphology from spheres to rods 4 cm from the interface in R5.

Figure 3.11: (a) Luminescence emission spectrum of Eu^{3+} doped La_2O_3, prepared with inner electrolyte solution containing 2% or 6% $Eu(NO_3)_3$, obtained at $\lambda_{ex.}=$ 386 nm. (b) Intensity as a function of % Eu^{3+} in the inner electrolyte solution.

plotting the intensity for each transition as a function of % Eu^{3+} in the inner electrolyte, the intensity increases as % Eu^{3+} increases as shown in figure 3.11 (b). This trend is also seen in samples during the first trial using 200 mM inner electrolyte. This proves that no concentration quenching is occurring when using % $Eu^{3+} \leq 6\%$ in the 50 mM inner electrolyte solution.

In order to determine whether luminescence intensity is uniform in Eu^{3+} doped La_2O_3 samples prepared from different regions of the RDF, the luminescence emission spectrum of oxide samples originating from different regions of a tube prepared with inner electrolyte composition 3% $Eu(NO_3)_3$, 98% $La(NO_3)_3$ was obtained. No significant difference in the luminescence intensity of these samples was observed as shown in figure 3.12. This proves that the Eu^{3+} dopants are evenly distributed throughout the tube when doping using RDF. Lifetime measurements were conducted on the same samples. 2 measurements for the lifetime of oxide sample originating from each region of the tube was taken as shown in table 3.1 and figure 3.13. Both measurements for each region were in good agreement, and the excited state lifetimes for samples originating from different regions of the tube were also in good agreement. As expected, the luminescence lifetime of the Eu^{3+} doped La_2O_3 samples was in the millisecond range. This is one of the primary characteristics of Lanthanide doped oxides that makes them excellent candidates for time resolved luminescence used in imaging and bio-sensing.

Er^{3+} doped La_2O_3: Er^{3+} luminescence, characterized by emissions at 543 nm, 552 nm, and 650 nm, is evident in Er^{3+} doped La_2O_3, synthesized with an inner
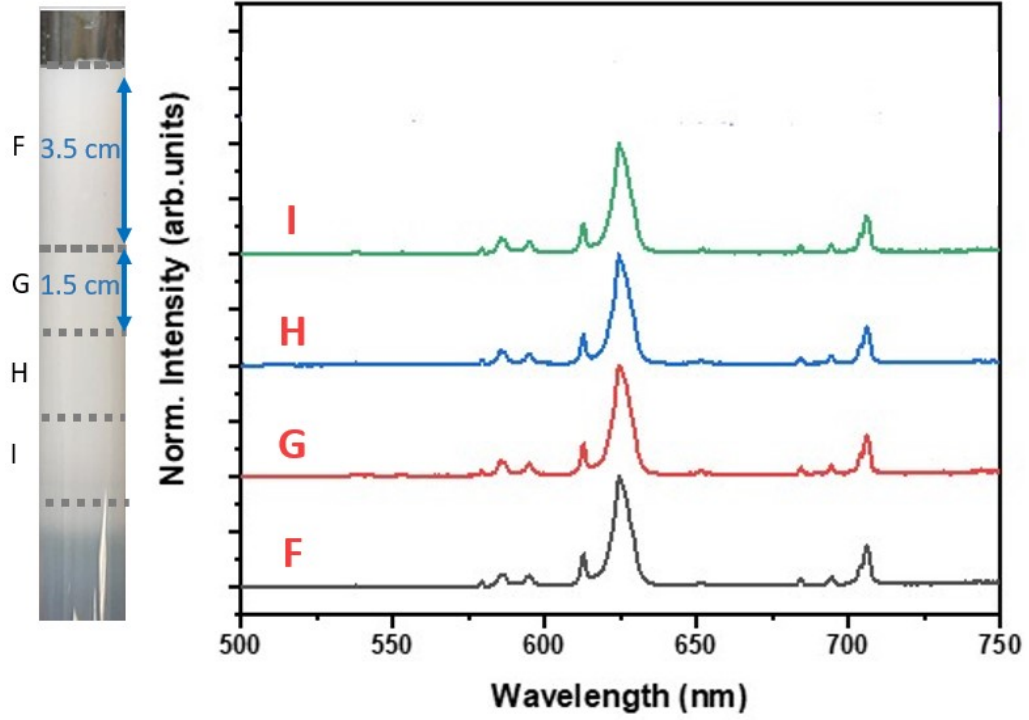
Figure 3.12: Luminescence emission spectra of Eu^{3+} doped La$_2$O$_3$ prepared using different regions of a 3% Eu(NO$_3$)$_3$ RDF obtained at $\lambda_{ex.}$= 395 nm.

Sample	τ_1 (ms)	τ_2 (ms)
F	0.4326 ±0.0028	0.8322 ±0.0203
G	0.4686 ±0.0053	0.8918 ±0.0316
H	0.4219 ±0.0040	0.7510 ±0.0183
I	0.4709 ±0.0034	0.8735 ±0.0314

Table 3.1: Luminescence excited state lifetime measurements for Eu^{3+} doped La$_2$O$_3$ samples prepared using samples extracted from different regions of a RDF tube with initial inner electrolyte composition 3% Eu(NO$_3$)$_3$, 97% La(NO$_3$)$_3$.

Figure 3.13: Luminescence excited state lifetime measurements for Eu^{3+} doped La_2O_3 samples prepared using samples extracted from different regions of a RDF tube with initial inner electrolyte composition 3% $Eu(NO_3)_3$, 97% $La(NO_3)_3$.
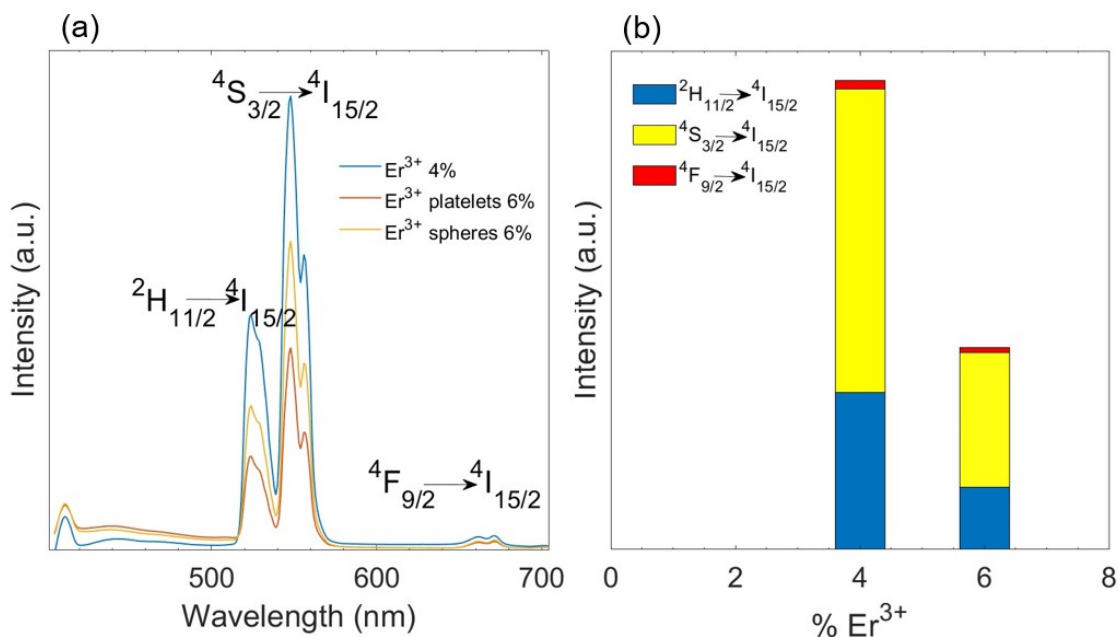
Figure 3.14: (a) Luminescence emission spectrum of Er^{3+} doped La_2O_3, prepared with inner electrolyte solution containing 4% or 6% $Er(NO_3)_3$, obtained at $\lambda_{ex.}=$ 386 nm. (b) Intensity as a function of % Er^{3+} in the inner electrolyte solution.

electrolyte composition of 4% or 6% $Eu(NO_3)_3$, as shown in figure 3.14 (a). When plotting the intensity for each transition as a function of % Er^{3+} in the inner electrolyte, the intensity decreases as % Er^{3+} increases as shown in figure 3.14 (b). This proves concentration quenching does occur when Er^{3+} is used as a dopant. Synthesis of Er^{3+} doped La_2O_3 using RDF requires Er^{3+} to be properly dispersed in the crystal matrix to overcome interactions that lead to nonradiative emissions.

Sm^{3+} doped La_2O_3: Sm^{3+} luminescence, characterized by line-like emissions at 564 nm, 600 nm, 650 nm, and 713 nm, is evident in Sm^{3+} doped La_2O_3 which is synthesized with an inner electrolyte composition of 2%, 5%, or 7.5% $SmCl_3$ as shown in figure 3.15 (a). When plotting the intensity for each transition as a function of % Sm^{3+} in the inner electrolyte, the intensity first increases between 2% and 5% $SmCl_3$, then decreases as % $SmCl_3$ in the inner electrolyte increases to 7.5% as shown in figure 3.15 (b). This proves concentration quenching does occur when %Sm^{3+} in the inner exceeds 5%. Synthesis of Sm^{3+} doped La_2O_3 using RDF requires optimization to work within the window where there is enough dopant to produce a legible luminescence spectrum, but not too much dopant leading to nonradiative emissions.

In order to determine whether luminescence intensity is uniform in Sm^{3+} doped La_2O_3 samples prepared from different regions of the RDF, the luminescence emission spectrum of oxide samples originating from different regions of a tube prepared with inner electrolyte composition 5% $SmCl_3$, 95% $LaCl_3$ was obtained. No significant difference in the luminescence intensity of these samples was observed as shown
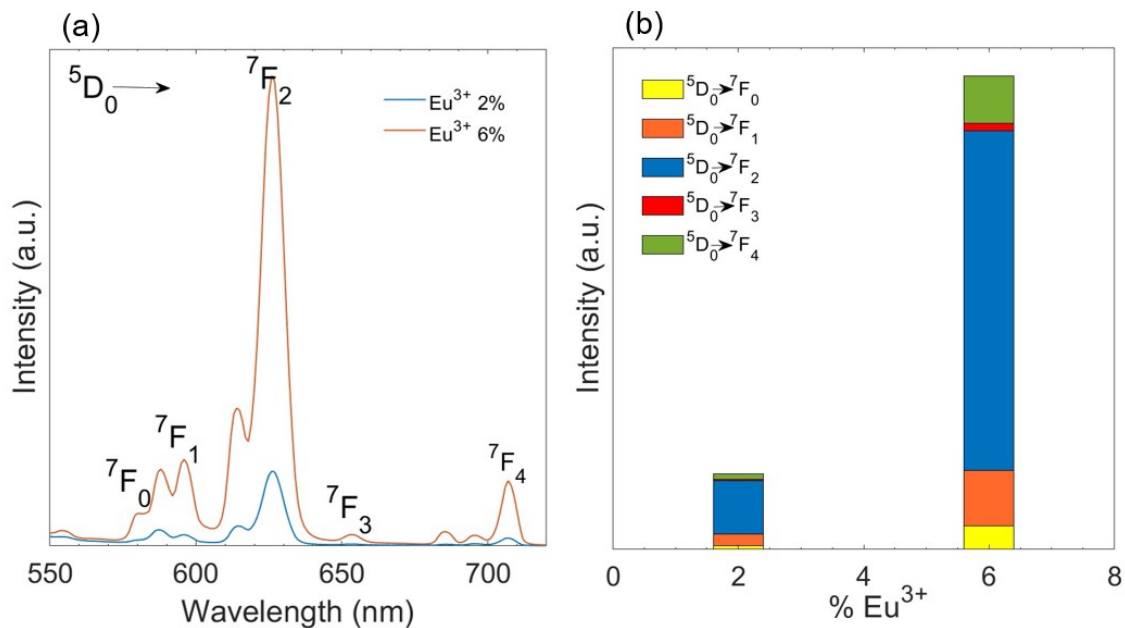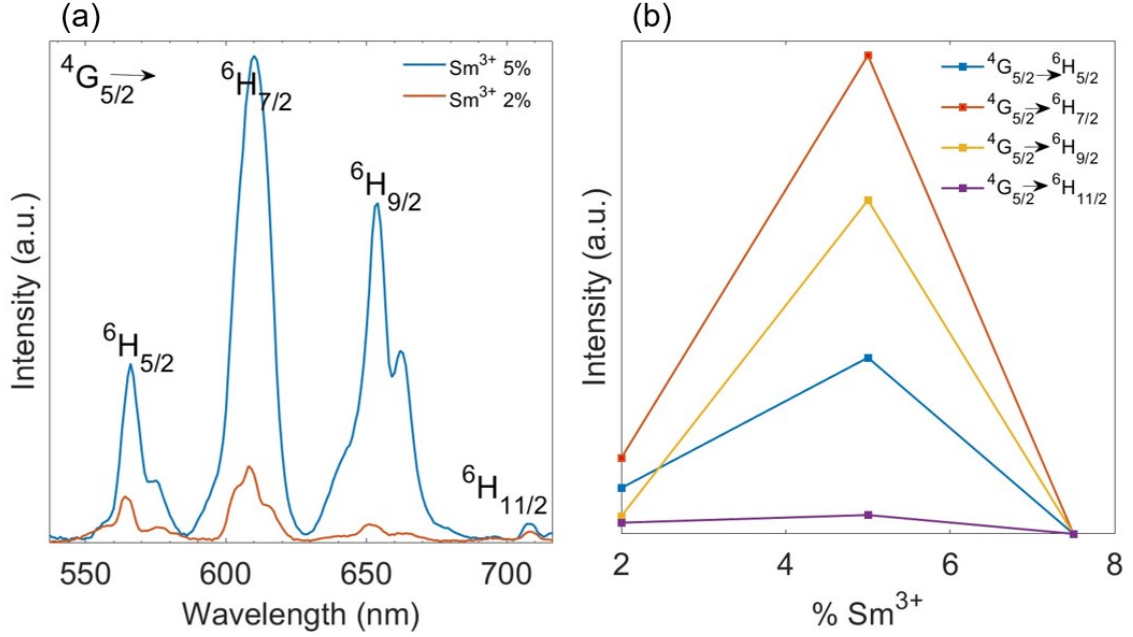
Figure 3.15: (a) Luminescence emission spectrum of Sm^{3+} doped La_2O_3, prepared with inner electrolyte solution containing 2%, 5% or 7.5% $Er(NO_3)_3$, obtained at $\lambda_{ex.}=$ 386 nm. (b) Intensity as a function of % Sm^{3+} in the inner electrolyte solution.

Sample	τ_1 (ms)	τ_2 (ms)	τ_3 (ms)
O	0.0945 $\pm$0.0048	0.3403 $\pm$0.0108	0.9505 $\pm$0.0147
P	0.0583 $\pm$0.0050	0.2970 $\pm$0.0072	0.8636 $\pm$0.0065
Q	0.1446 $\pm$0.0063	0.5361 $\pm$0.0184	1.0868 $\pm$0.0169
R	0.1697 $\pm$0.0078	0.5602 $\pm$0.0278	1.0878 $\pm$0.0212

Table 3.2: Luminescence excited state lifetime measurements for Sm^{3+} doped La_2O_3 samples prepared using samples extracted from different regions of a RDF tube with initial inner electrolyte composition 5% $SmCl_3$, 95% $LaCl_3$.

in figure 3.16. This proves that the Sm^{3+} dopants are evenly distributed throughout the tube when doping using RDF.

Lifetime measurements were conducted on oxide samples originating from an RDF with 5% $SmCl_3$, 95% $LaCl_3$ inner electrolyte. 3 measurements for the lifetime of oxide sample originating from each region of the tube was taken as shown in figure 3.17 and in table 3.2. Measurements for each region were in good agreement, and the excited state lifetimes for samples originating from different regions of the tube were also in good agreement. As expected, the luminescence lifetime of the Sm^{3+} doped La_2O_3 samples was in the millisecond range which further validates the credibility of Ln^{3+} doping using RDF.

Tb^{3+}, Eu^{3+} co-doped La_2O_3: Tb^{3+} luminescence, characterized by line-like emissions at 490 nm, 540 nm, and 580 nm, is evident in Tb^{3+} doped La_2O_3, synthe-
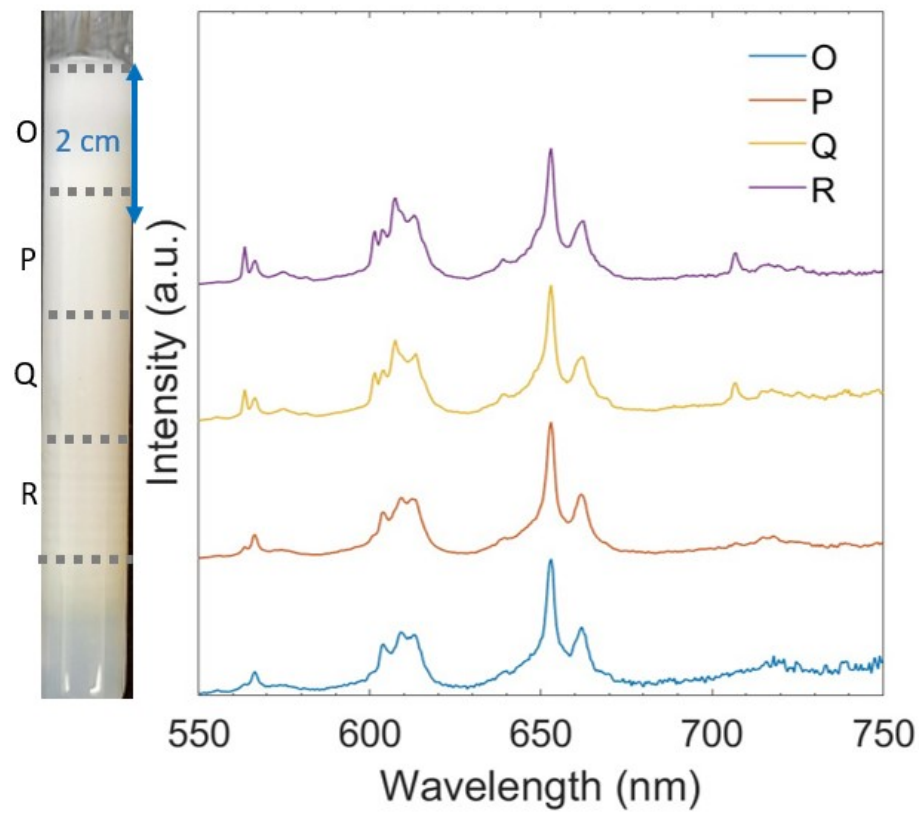
Figure 3.16: Luminescence emission spectra of Sm^{3+}, doped La_2O_3 prepared from different regions of an RDF with inner electrolyte 5% $SmCl_3$, 95% $La(NO_3)_3$ obtained at $\lambda_{ex.}=$ 408 nm.
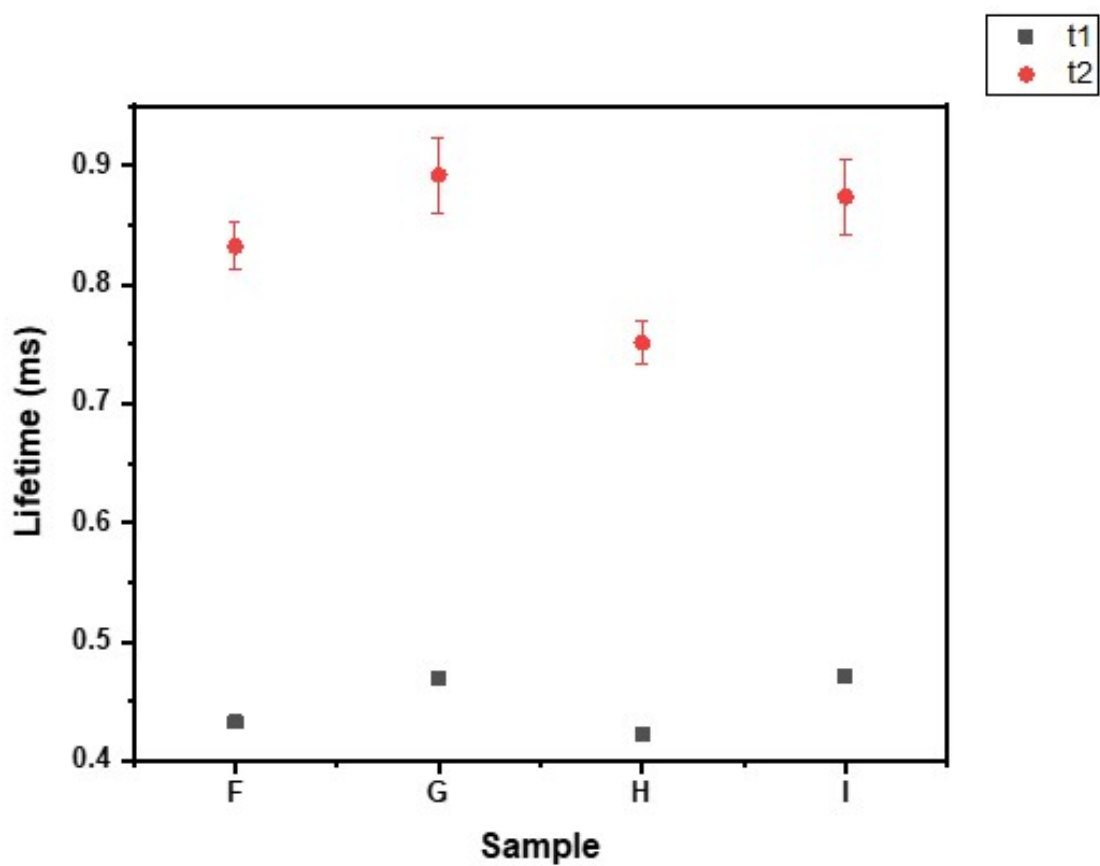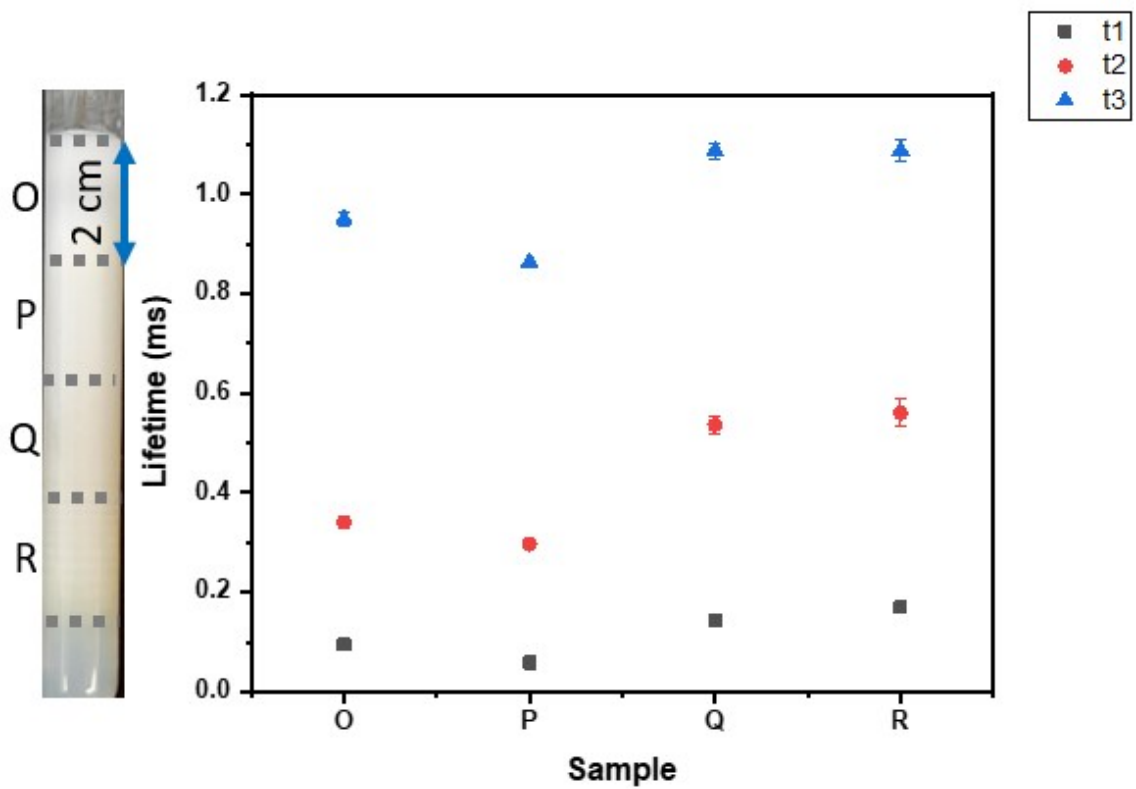
Figure 3.17: Luminescence excited state lifetime measurements for Sm^{3+} doped La_2O_3 samples prepared using samples extracted from different regions of a RDF tube with initial inner electrolyte composition 5% $SmCl_3$, 95% $LaCl_3$.
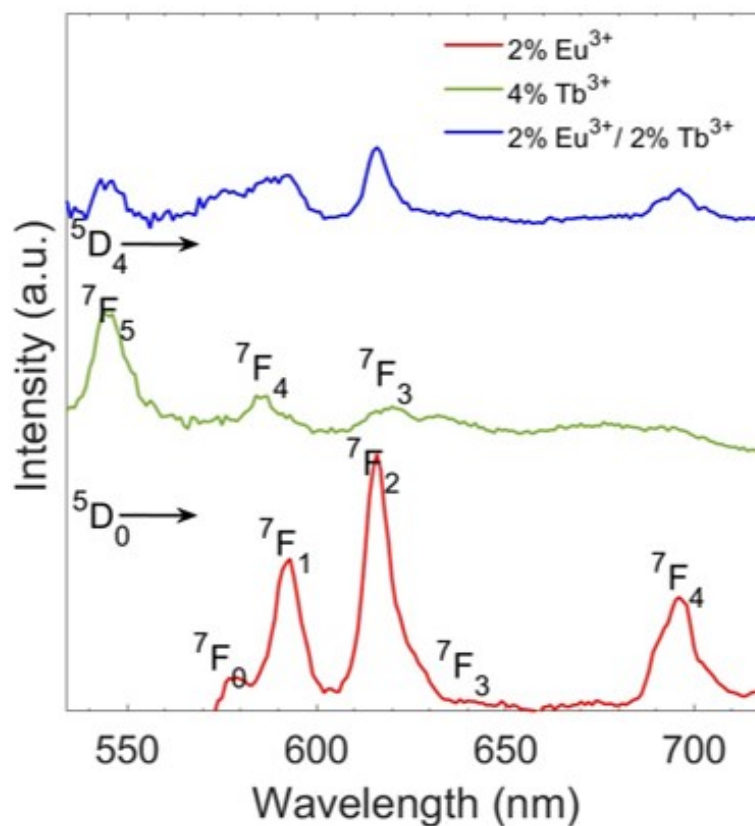
Figure 3.18: Luminescence emission spectra of Eu^{3+}, Tb^{3+}, or Eu^{3+} and Tb^{3+} doped La_2O_3, prepared with inner electrolyte solution containing 2% Eu^{3+}, 4% Tb^{3+}, or 2% Eu^{3+} and 2% Tb^{3+} respectively, obtained at $\lambda_{ex.}= 386$ nm.

sized with an inner electrolyte composition of 4% $TbCl_3$ as shown in figure 3.18. A co-doping experiment using RDF was attempted to synthesize La_2O_3: Eu^{3+},Tb^{3+} using an inner electrolyte solution of 2% $TbCl_3$, 2% $Eu(NO_3)_3$, and 96% $La(NO_3)_3$. The luminescence emission spectrum of the co-doped sample displayed peaks characteristic of both Eu^{3+}, and Tb^{3+} as shown in figure 3.18. The main concern while working with Tb^{3+} as a dopant is whether it is being oxidized to Tb^{4+} after heat treatment in the furnace.

In order to determine whether luminescence intensity is uniform in Ln^{3+} doped La_2O_3 samples prepared from different regions of the RDF, the luminescence emission spectrum of oxide samples originating from different regions of a tube prepared with inner electrolyte composition 2% $TbCl_3$, 2% $Eu(NO_3)_3$, and 96% $La(NO_3)_3$ was obtained as shown in figure 3.19. No significant difference in the luminescence intensity of these samples was obtained. This proves that the Eu^{3+} and Tb^{3+} dopants are evenly distributed throughout the tube when doping using RDF. Furthermore, it proves that the luminescence intensity of oxide samples originating from different regions of the tube is somewhat even.

As shown in figure 3.18, the luminescence intensity of the codoped sample is
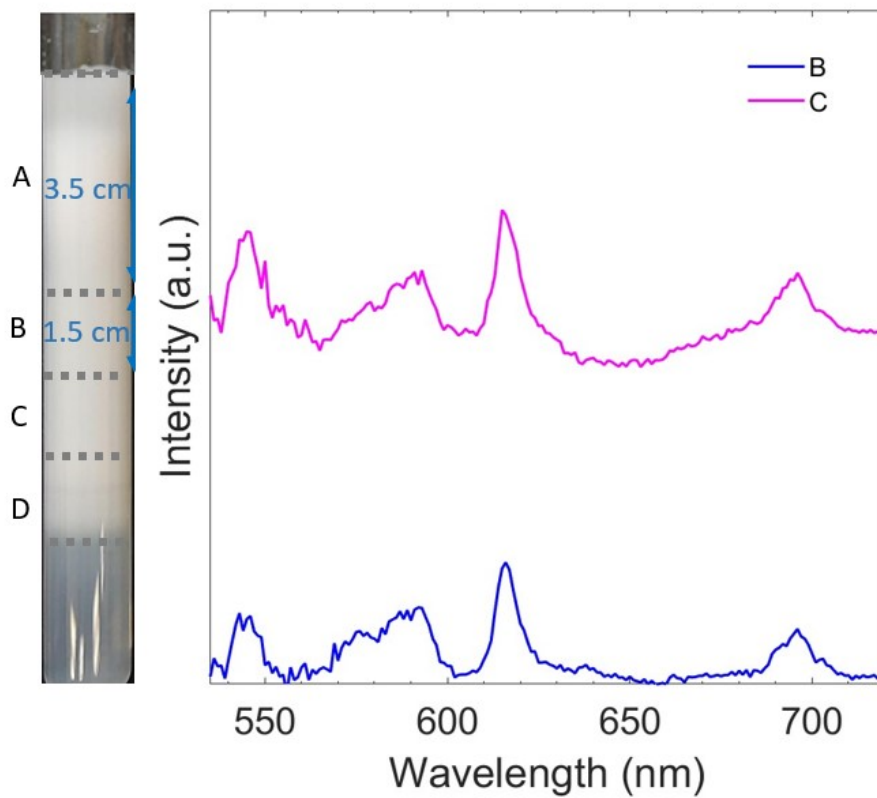
Figure 3.19: Luminescence emission spectra of Eu^{3+}, Tb^{3+} co-doped La_2O_3 prepared different regions of the RDF obtained at $\lambda_{ex.}= 386$ nm.

lower than the luminescence intensity for a sample prepared with Eu^{3+} or Tb^{3+} alone. The next step in the synthesis process of the codoped sample includes finding the optimum inner electrolyte concentration for the co-doped La_2O_3; Eu^{3+}, Tb^{3+} where the spherical morphology of the phosphors is retained and the luminescence intensity is highest. In order to do this, 6 RDF tubes with different inner electrolyte compositions were prepared as shown in figure 3.20 and the morphology and luminescence intensity of the samples was explored to determine which inner electrolyte composition would lead to the synthesis of microspheres with the highest luminescence intensity. The first 3 tubes consisted of an inner electrolyte composition of 3% $Eu(NO_3)_3$, and 2%, 4%, or 6% $TbCl_3$. The second 3 tubes consisted of an inner electrolyte composition of 5% $Eu(NO_3)_3$, and 2%, 4%, or 6% $TbCl_3$. From the tubes containing 5% $Eu(NO_3)_3$ and different amounts of $TbCl_3$, no microspheres were obtained; the morphology of the doped $La(OH)_3$ was mostly needle-like. The tube containing 5% $Eu(NO_3)_3$ and 4% $TbCl_3$ showed the highest luminescence intensity for each transition. Concentration quenching did take place in the tube containing 5% $Eu(NO_3)_3$ and 6% $TbCl_3$ which did have a significantly lower luminescence intensity for each transition. These trends can be seen in figure 3.21 and in figure 3.22 (b). The increased amount of dopant did lead to visible banding in these tubes 3.20, a trend mentioned earlier when working with 200 mM inner electrolyte doped with $Eu(NO_3)_3$ or $Er(NO_3)_3$. From the tubes containing 3% $Eu(NO_3)_3$ and different amounts of $TbCl_3$, microspheres were obtained in all three tubes. The tube prepared with 3% $Eu(NO_3)_3$ and 2% $TbCl_3$ showed the highest net luminescence intensity among samples collected from these three tubes as shown in figure 3.21 and in figure 3.22 (a). The morphology of the $La(OH)_3$ microspheres codoped with Eu^{3+} and Tb^{3+} and the luminescence emission spectrum of the La_2O_3: Eu^{3+}, Tb^{3+}, both synthesized with optimum inner electrolyte composition of 3% Eu^{3+}, and 2% Tb^{3+} can be seen in figure 3.23 (a), and figure 3.23 (b) respectively.

3.2.1.4 Fluorescence Microscope

Photoluminescence of the spherical doped La_2O_3 final product is also clearly visible using a fluorescence microscope. Real Camera shots of luminescent Ln^{3+} doped La_2O_3 where $Ln^{3+}=Eu^{3+}$, Er^{3+}, or Sm^{3+} are obtained at $\lambda_{excitation}=390-410$ nm using an RGB filter. The oxide samples seen are prepared from $La(OH)_3$ samples extracted approximately 5 cm from the interface of tubes with original inner electrolyte composition 2% $Eu(NO_3)_3$, 98% $La(NO_3)_3$ as shown in figure 3.24 (a), 4% $Er(NO_3)_3$, 96% $La(NO_3)_3$ as shown in figure 3.24 (b), and 5% $SmCl_3$, 95% $LaCl_3$ as shown in figure 3.24 (c).

3.2.1.5 UV lamp

Luminescence of Ln^{3+} doped La_2O_3 where $Ln^{3+}=Eu^{3+}$, Er^{3+}, Sm^{3+}, Tb^{3+}, or Tb^{3+} and Eu^{3+} is shown in figures 3.25 and 3.26 using a UV lamp. The inner electrolyte compositions used to synthesize the displayed samples in figure 3.25 are 2% $Eu(NO_3)_3$, 98% $La(NO_3)_3$ for sample (a), 2% $TbCl_3$, 98% $La(NO_3)_3$ for sam-
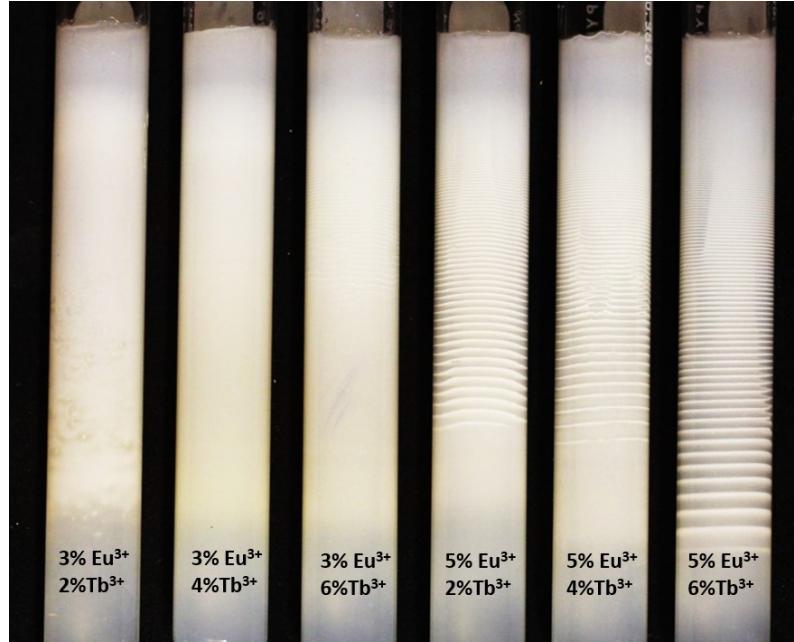
Figure 3.20: $La(OH)_3$ micro-spheres co-doped with 50 mM inner electrolyte solutions which contain different amounts $Eu(NO_3)_3$, and $TbCl_3$.

ple (b), 2% $TbCl_3$, 2% $Eu(NO_3)_3$, 98% $La(NO_3)_3$ for sample (c), 4% $Er(NO_3)_3$, 96% $La(NO_3)_3$ for sample (d), 5% $SmCl_3$, 95% $LaCl_3$ for sample (e). The inner electrolyte compositions used to synthesize the displayed samples in figure 3.26 are 100% $La(NO_3)_3$ for sample (a), 5% $SmCl_3$, 95% $LaCl_3$ for sample (b), 4% $Er(NO_3)_3$, 96% $La(NO_3)_3$ for sample (c), 2% $Eu(NO_3)_3$, 98% $La(NO_3)_3$ for sample (d).

3.2.1.6 BET Surface Area Measurements

Surface area analysis using Brunauer-Emmett-Teller BET is performed on a $La(OH)_3$ control synthesized using a 50 mM $La(NO_3)_3$ inner electrolyte, and it's corresponding oxide obtained after calcination. The $La(OH)_3$ isotherm shown in figure 3.27(a) is a type IV isotherm characterized by an inflection point where the first monolayer almost completes formation followed by a low slope region where pore condensation takes place. A typical feature of Type IV isotherms, found in figure 3.27(a), is a final saturation plateau of variable length which in our case is reduced to a mere inflection point. Having a type IV isotherm, $La(OH)_3$ is mesoporous (pore diameter 2-50 nm). It has a surface area of 11 m^2g^{-1} and pore volume 0.06 cm^3g^{-1} as shown in table 3.3. Since capillary condensation is accompanied by a hysteresis loop, $La(OH)_3$ has a type IVa isotherm. A hysteresis, which is associated with capillary condensation taking place in mesopores, is seen when the pore width exceeds a certain critical width determined by the adsorption system and the temperature[128]. The La_2O_3 isotherm shown in figure 3.27(b) can also be seen as a type IV isotherm although the hysteresis is not as obvious. The inflection point indicates the approximate location of monolayer formation, and the low slope region in middle of the isotherm indicates where the first few multilayers are formed. Since La_2O_3 has a type IV isotherm, it
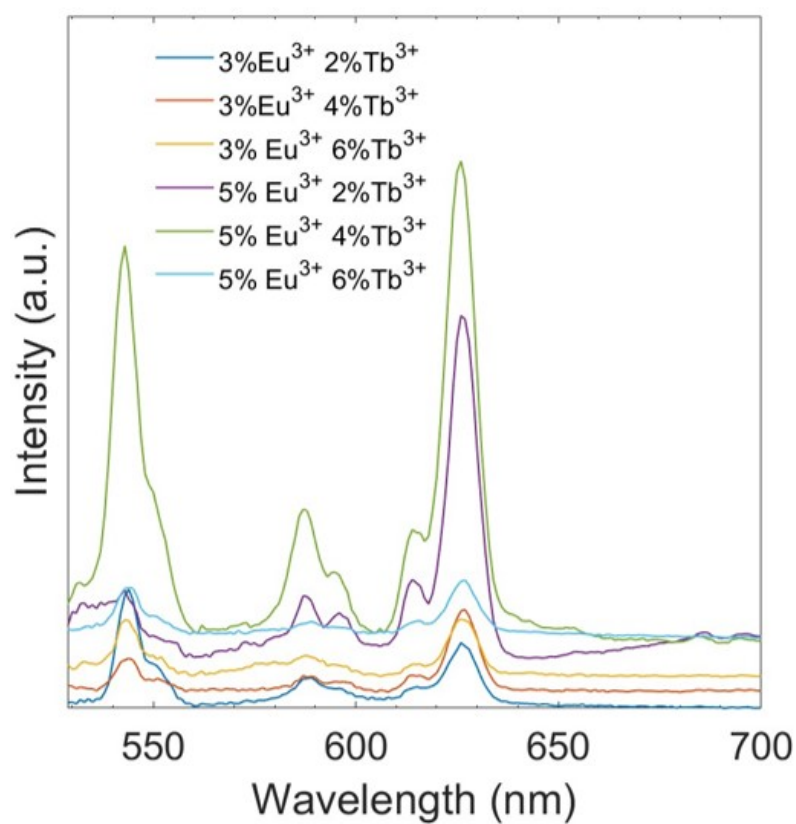
Figure 3.21: La_2O_3: Eu^{3+}, Tb^{3+} luminescence emission spectra for samples prepared with different inner electrolyte compositions. Each spectrum shows 3 peaks; the first at 545 nm, the second at 589 nm, and the third at 626 nm.
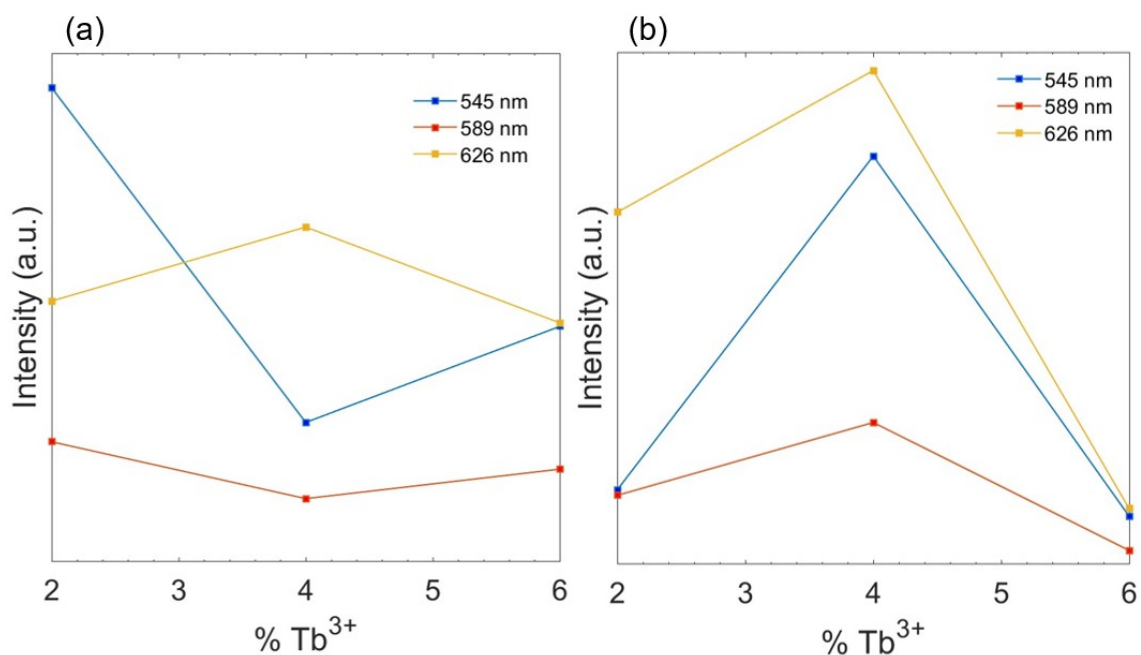
Figure 3.22: (a) Intensity for each transition of La_2O_3: Eu^{3+}, Tb^{3+} as a function of % Tb^{3+} for samples prepared with 3% Eu^{3+}. (b) Intensity for each transition of La_2O_3: Eu^{3+}, Tb^{3+} as a function of % Tb^{3+} for samples prepared with 5% Eu^{3+}.
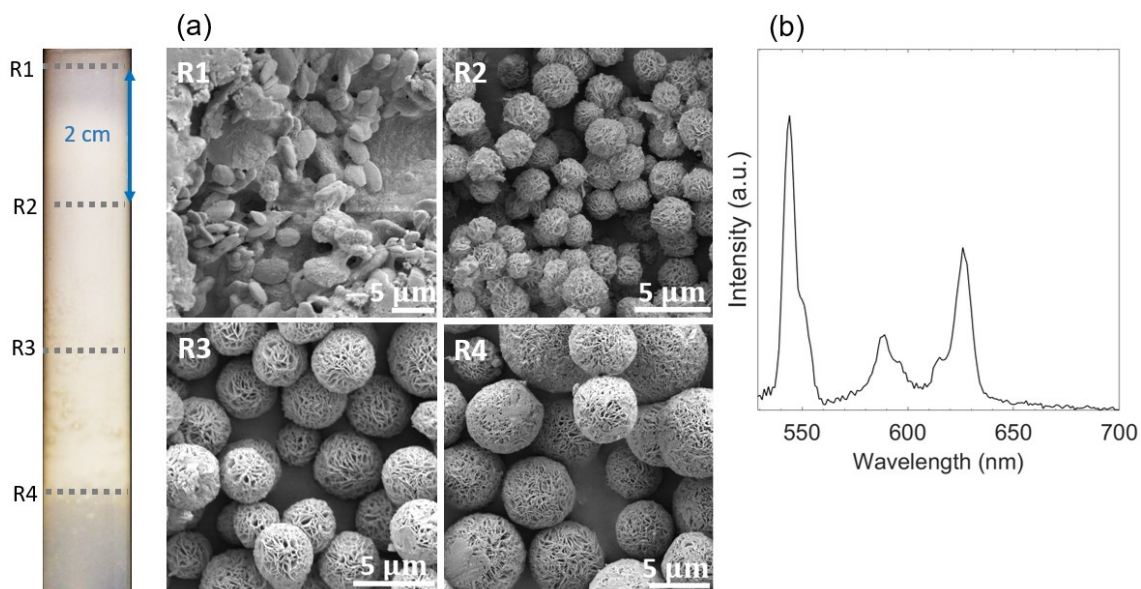
Figure 3.23: (a) $La(OH)_3$ microspheres codoped with Eu^{3+} and Tb^{3+} synthesized using optimum inner electrolyte composition 3% $Eu(NO_3)_3$, 2% $TbCl_3$, and 95% $La(NO_3)_3$. (b) Luminescence emission spectrum of La_2O_3: Eu^{3+},Tb^{3+} synthesized using optimum inner electrolyte composition 3% $Eu(NO_3)_3$, 2% $TbCl_3$, and 95% $La(NO_3)_3$.
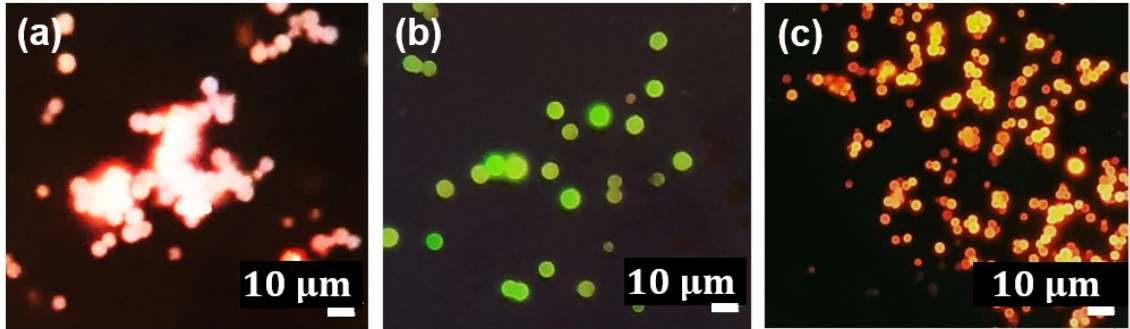
Figure 3.24: Real Camera shots of (a) Eu^{3+}, (b) Er^{3+}, (c) Sm^{3+} doped La_2O_3 obtained at $\lambda_{ex.}=390-410$ nm using an RGB filter using a fluorescence microscope.
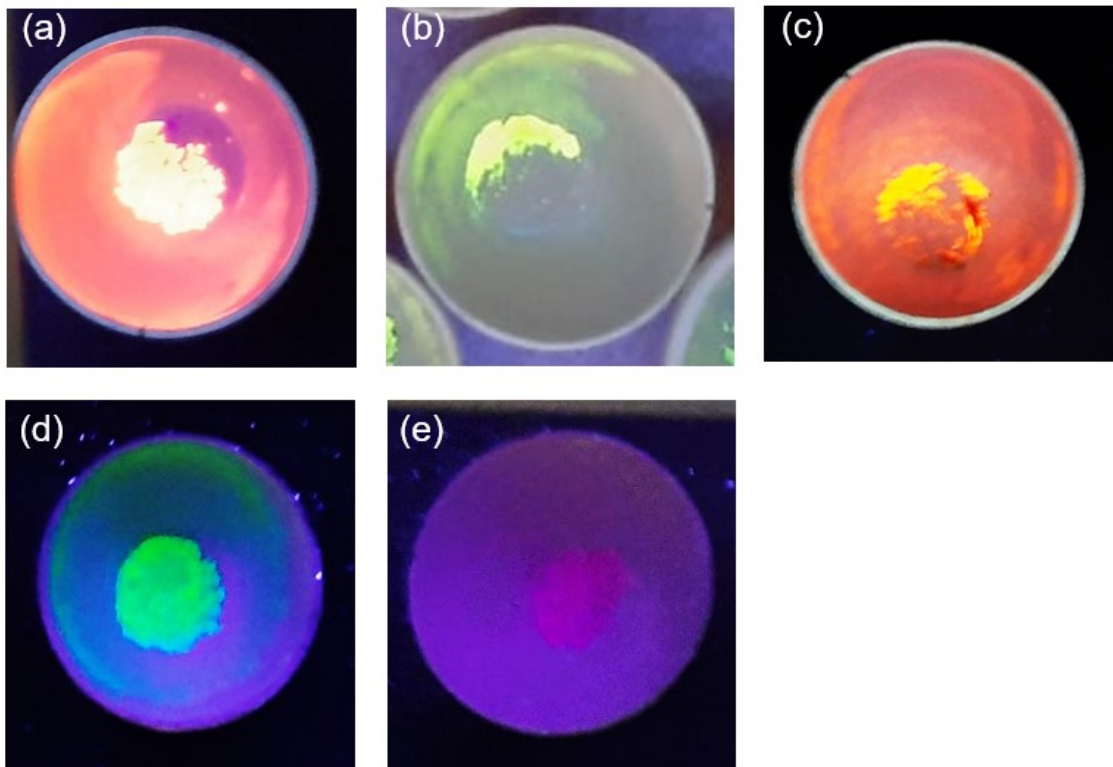
Figure 3.25: Real camera shots using a UV lamp of (a) Eu^{3+}, (b) Tb^{3+}, (c) Eu^{3+} and Tb^{3+} doped La_2O_3 obtained at $\lambda_{ex.}=386$ nm and of (e) Er^{3+}, (f) Sm^{3+} doped La_2O_3 obtained at $\lambda_{ex.}=256$ nm.
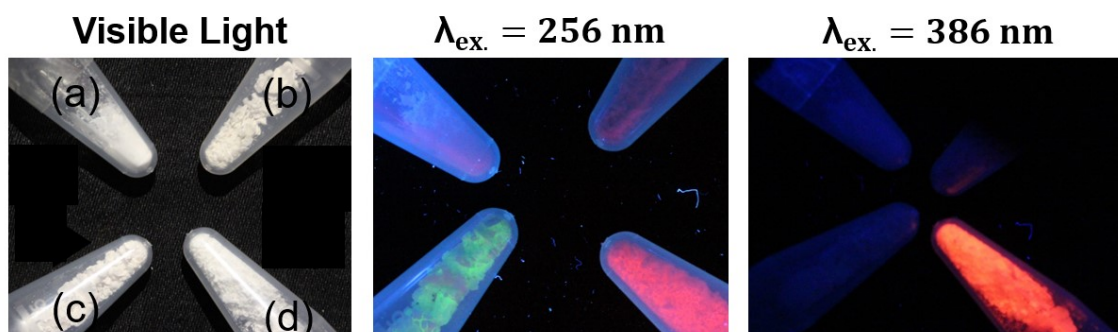
Figure 3.26: Real camera shots using a UV lamp of (a) control, (b) Sm^{3+}, (c) Er^{3+}, (d) Eu^{3+} doped La_2O_3 in visible light and UV light at $\lambda_{ex.}$=256 nm and $\lambda_{ex.}$=386 nm.

Sample	Surface Area (m^2g^{-1})	Pore Volume (cm^3g^{-1})
$La(OH)_3$	11	0.06
La_2O_3	8	0.03

Table 3.3: BET Surface Area and Pore Volume Measurements

is also mesoporous [129]. It has a similarly low surface area to $La(OH)_3$ and a similarly low pore volume as tabulated in 1.5. It's surface area is 8 m^2g^{-1} and it's pore volume 0.03 cm^3g^{-1}. The slight difference in porosity between $La(OH)_3$ and La_2O_3 is indicative of underlying differences in their crystal structure.

3.2.1.7   Zeta Potantial Measurements

Zeta potential measurements are conducted for doped La_2O_3 samples. In the tube containing $La(OH)_3$ prepared with 4% Erbium, oxide prepared from hydroxide sample extracted 5.5 cm from the interface exhibits a negative zeta potential of -7.69 mV at neutral pH. In the tube containing $La(OH)_3$ prepared with 2% Europium, oxide prepared from hydroxide extracted 1 cm from the interface, has a negative zeta potential of -5.89 mv at neutral pH. In the tube prepared from 2% Samarium, oxide prepared from precipitate 1cm from the interface, has a negative zeta potential of -0.89 mv at neutral pH. The somewhat low values of zeta potential indicate the particles' tendency to agglomerate in solution at neutral pH.

3.2.1.8   FTIR

Once synthesized, the Ln^{3+} doped La_2O_3 final product is very sensitive to moisture in the air. The XRD in figure 3.2 proved that upon removal of the Ln^{3+} doped La_2O_3 from the furnace, it was pure Lanthanum Oxide; however, FTIR analysis shown in figure 3.28 performed on Lanthanum Oxide samples exposed to the atmosphere for several months indicated that the oxides revert back to hydroxides upon exposure to moisture in the air. Fourier transform infrared spectroscopy (FTIR) is performed to asses the vibrational modes of the final product functional groups. The prod-
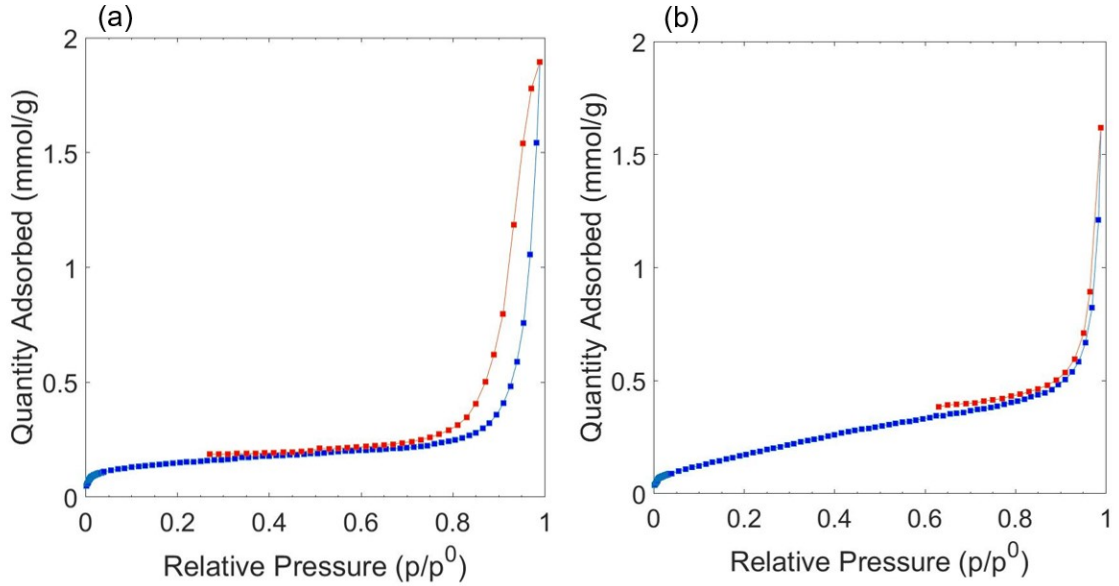
Figure 3.27: Adsorption desorption isotherm for (a) La(OH)$_3$, (b)La$_2$O$_3$ samples prepared using an initial inner electrolyte composition of 50mM La(NO$_3$)$_3$.

ucts tested included a La(OH)$_3$ control sample prepared using a 50 mM La(NO$_3$)$_3$ inner electrolyte solution, a supposed La$_2$O$_3$ control sample, which had been exposed to the atmosphere for several months, prepared using a 50 mM La(NO$_3$)$_3$ inner electrolyte solution, a supposed Eu^{3+} doped La$_2$O$_3$ sample, also exposed to the atmosphere for several months, collected from the upper portion (0-3.5 cm from the interface) of an RDF with inner electrolyte composition 2% Eu(NO$_3$)$_3$, 48% La(NO$_3$)$_3$, and a sample from the latter tube collected from the lower portion of the RDF (3.5-8 cm from the interface). As mentioned earlier in figure 3.4, samples collected from the upper portion of the tube have a platelet morphology while samples collected from the lower portion of the tube have a spherical morphology. All FTIR spectra obtained were identical, thus indicating that the 4 samples had the same functional groups. Each spectrum shows at 3400cm^{-1} a characteristic peak of the stretching mode of hydroxyl groups, and a distinct sharp peak at 3400cm^{-1} that is assigned to the stretching mode of the hydroxyl group of free La–OH groups. The band centered at 1634 cm^{-1} corresponds to the deformation vibration of water molecules. The bands in the region between 800 cm^{-1} and 1700 cm^{-1} can be attributed to carbonate ions resulting from the water dissolution of carbon dioxide present in air at high pH. As for that band at 640 cm^{-1}, it can be assigned to the bending mode of the La–O bond of lanthanum hydroxide crystals [130]. Therefore, FTIR confirms that the products being tested are La(OH)$_3$. Once the La$_2$O$_3$ is freshly prepared, it should be kept under vacuum to prevent reduction to La(OH)$_3$ and to maintain optimum luminescence capacity.
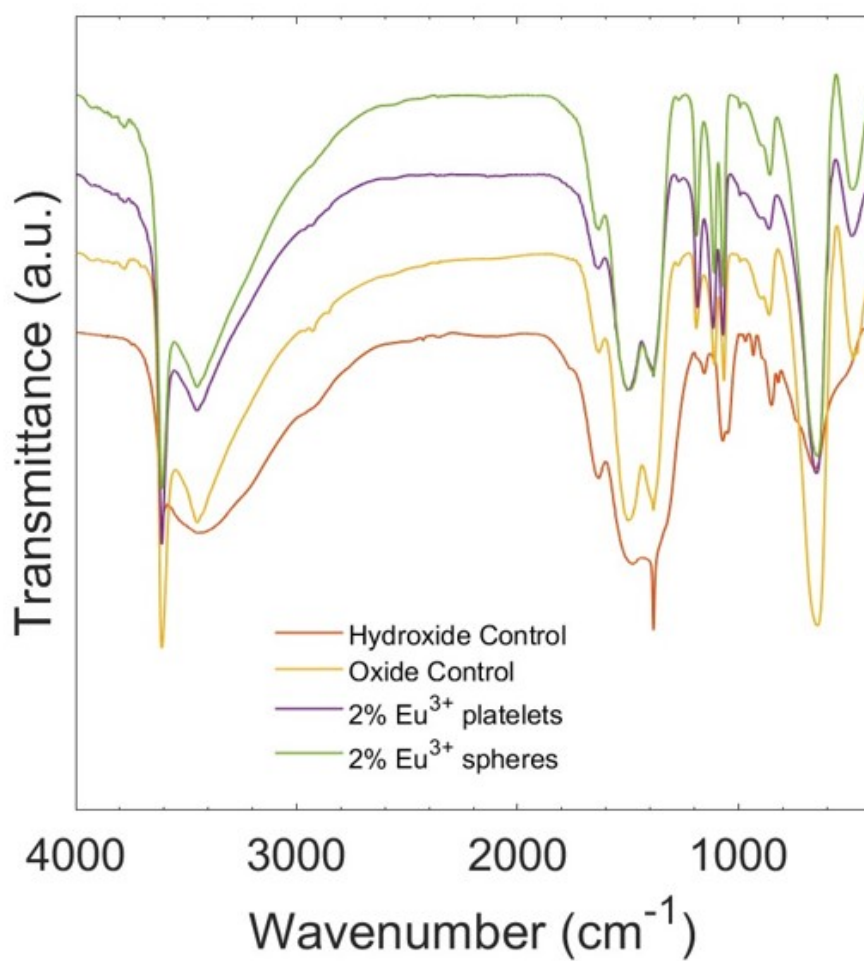
Figure 3.28: FTIR Spectra of $La(OH)_3$ and supposed La_2O_3 samples exposed to the atmosphere for several months.

3.2.2 *Growth mechanism studied on samples prepared with 300 mM inner electrolyte*

The growth mechanism of the $La(OH)_3$ microspheres within the RDF is studied using samples prepared with a 300mM inner electrolyte concentration. The growth study is conducted under an optical microscope where real camera shots of the growing spheres are periodically taken every hour. The radial size of the spheres is plotted as a function of time. SEM images of the fully grown spheres are also taken. Results of this study emphasize the difference in growth kinetics in different regions of the RDF as well as the difference in growth patterns between a control sample and a sample doped with Er^{3+}.

3.2.2.1 Growth of $La(OH)_3$ (control) precipitate in RDF

To study the radial growth of $La(OH)_3$ spheres in a control tube, 14 M NH_3 solution is poured onto a 300 mM $La(NO_3)_3$ inner electrolyte. Camera shots of the growing spheres being formed are taken 4 cm and 5.5 cm from the interface. The radial size of 2 spheres in R1, 4 cm from the interface, is plotted as a function of time in figure 3.29 (a). From the graph, it is apparent that the radius of the first sphere increases from 5 μm to 25 μm in 36 hours. The radius of the second sphere increases from 5 μm to around 29 μm in 36 hours. The growing spheres under optical microscope at time T= 7 h when their radius $\simeq$ 10 μm are shown in figure 3.29 (c). An SEM image of the fully grown spheres having radius $\simeq$ 25 μm is shown in figure 3.29 (b). The same measurements are taken for 2 spheres in R2, 5.5 cm from the interface. Their radial growth is also plotted as a function of time in figure 3.30 (a). The radius of the first sphere increases from 5 μm to around 23 μm and reaches a plateau after 73 hours. The radius of the second sphere increases from 5 μm to around 30 μm and also reaches a plateau after 73 hours. The growing spheres under optical microscope at time T= 7 h when their radius $\simeq$ 10 μm are shown in figure 3.30 (c). An SEM image of the fully grown spheres having radius $\simeq$ 30 μm is shown in figure 3.30 (b).

3.2.2.2 Growth of Er^{3+} doped $La(OH)_3$ precipitate in RDF

To study the radial growth of Er^{3+} doped $La(OH)_3$ spheres in a 1D tube, 14 M NH_3 solution is poured onto a 300 mM $Ln(NO_3)_3$ inner electrolyte solution composed of 6% $Er(NO_3)_3$, 94% $La(NO_3)_3$. Camera shots of the growing spheres being formed are taken 4 cm and 5.5 cm from the interface. The radial size of 2 spheres in R1, 4 cm from the interface, is plotted as a function of time in figure 3.31 (a). From the graph, it is apparent that the radii of the first and second sphere increase from 3 μm to 12 μm in 14 hours. At T= 14 hours, a plateau is obtained. The growing spheres under optical microscope at time T= 7 h when their radius $\simeq$ 10 μm are shown in figure 3.29 (c). An SEM image of crushed spheres obtained 4 cm from the interface are shown in figure 3.29 (b). The same measurements are taken for 2 spheres in R2, 5.5 cm from the interface. Their radial growth is also plotted as a function of time in figure 3.32 (a). The radius of the first sphere increases from 5 μm to around 13 μm and reaches a plateau after 9 hours. The radius of the second sphere increases
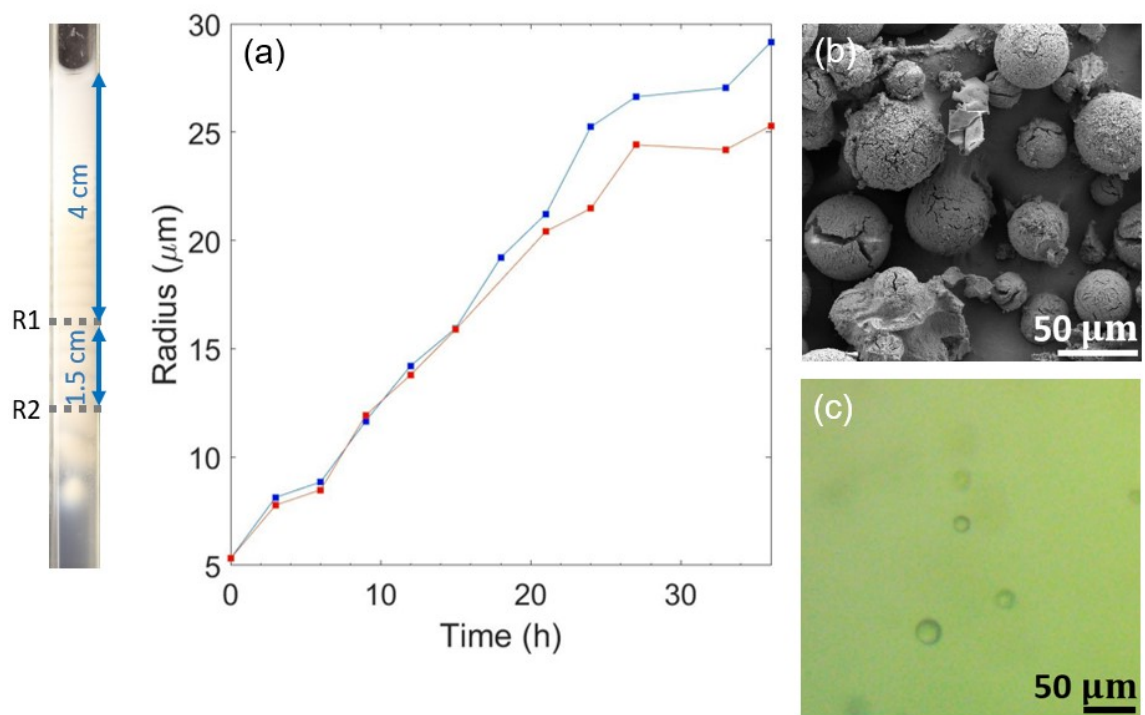
Figure 3.29: Radial growth study for La(OH)$_3$ micro-spheres, synthesized using a 300 mM La(NO$_3$)$_3$ inner electrolyte, 4 cm from the RDF interface using (a) Radial growth (μm) as a function of time (h), (b) SEM image of the fully grown micro-spheres, (c) Image under optical microscope of the growing sphere at T= 7h.
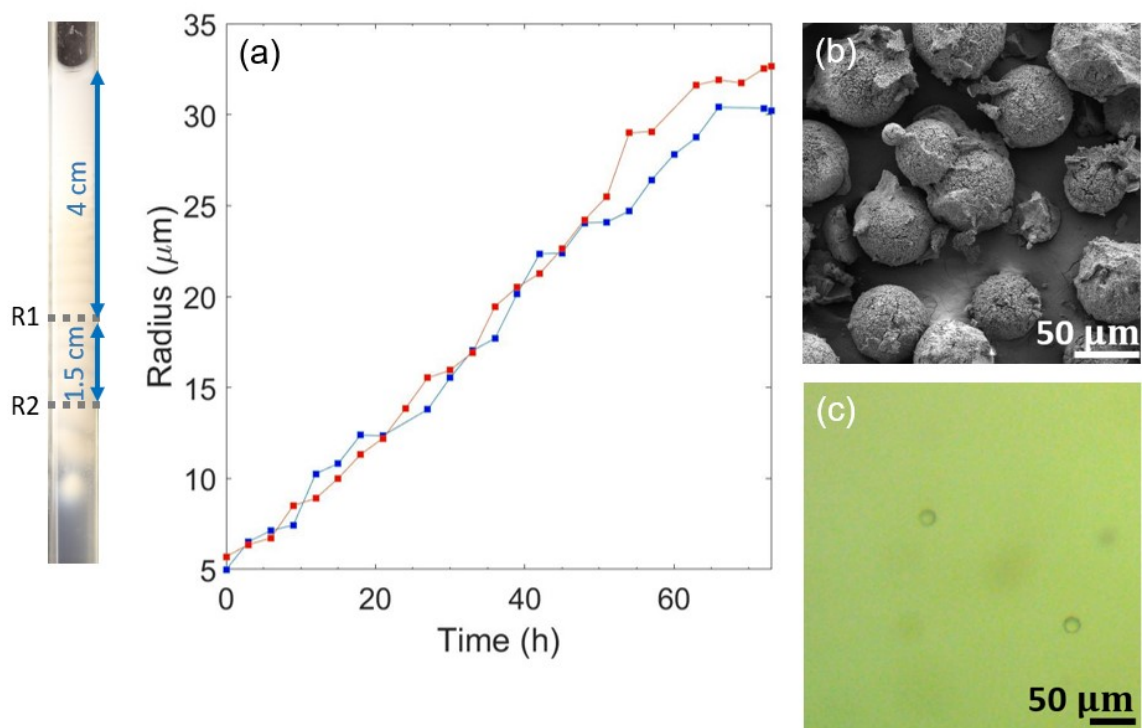
Figure 3.30: Radial growth study for La(OH)$_3$ micro-spheres, synthesized using a 300 mM La(NO$_3$)$_3$ inner electrolyte, 5.5 cm from the RDF interface using (a) Radial growth (µm) as a function of time (h), (b) SEM image of the fully grown micro-spheres, (c) Image under optical microscope of the growing sphere at T= 7h.
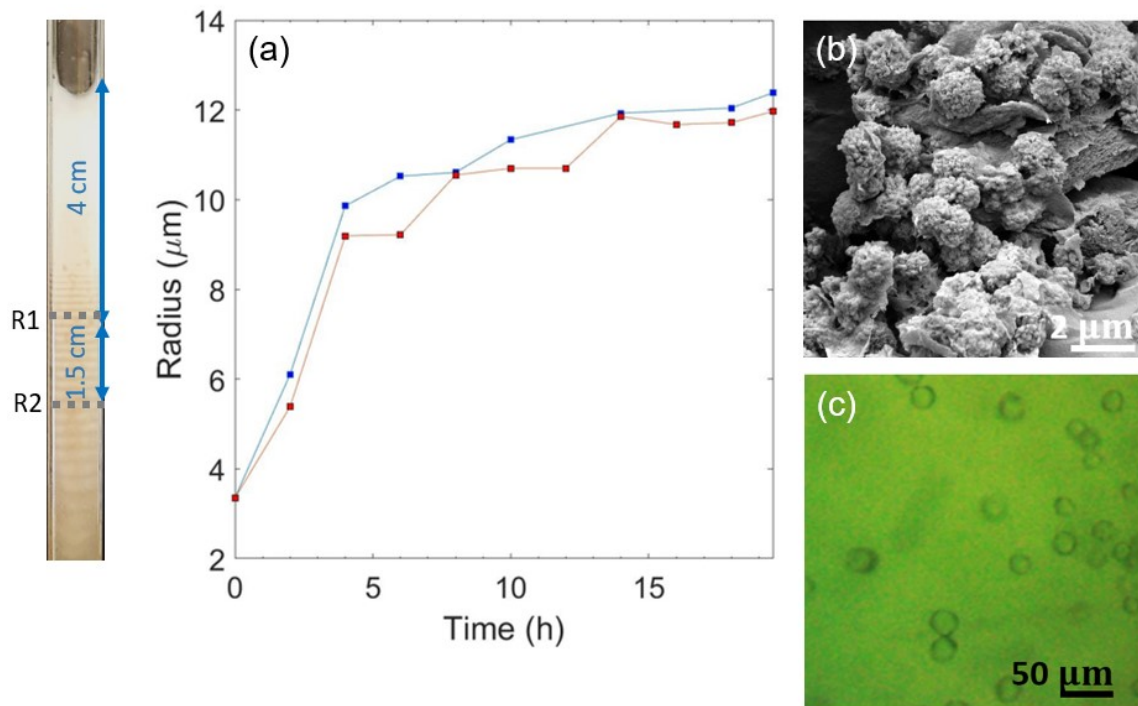
Figure 3.31: Radial growth study of Er^{3+} doped $La(OH)_3$ micro- spheres, synthesized using a 300 mM inner electrolyte with 96% $La(NO_3)_3$ and 4% $Er(NO_3)_3$, 4 cm from the RDF interface using (a) Radial growth (μm) as a function of time (h), (b) SEM image of the broken micro-spheres, (c) Image under optical microscope of the growing sphere at T= 7h.

from 5 μm to around 15 μm and also reaches a plateau after 9 hours. The growing spheres under optical microscope at time T= 7 h when their radius $\simeq$ 12 μm are shown in figure 3.32 (c). An SEM image of the broken spheres extracted from R2 is shown in figure 3.30 (b).

3.2.2.3 Observations

The doped spheres, which reach a final radius of $\approx$ 14 μm, appear to have half the radius of the control spheres which reach a final radius of $\approx$ 30 μm. The doped spheres also reach a plateau faster than the control (10 h vs. 60 h).
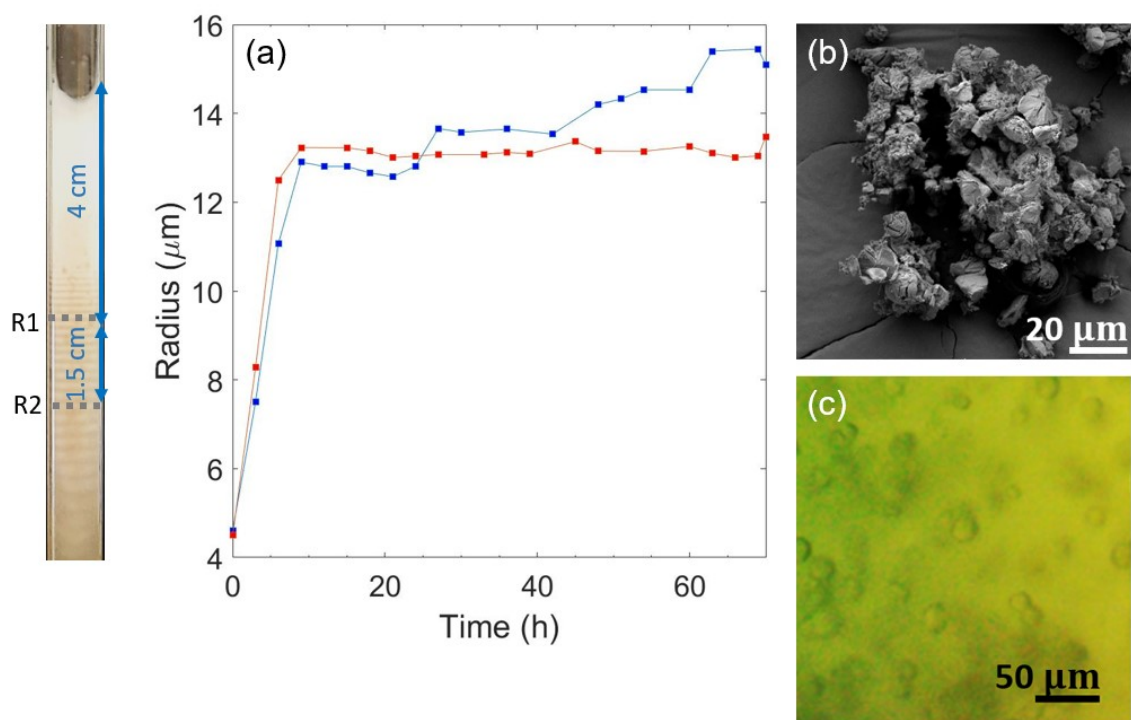
Figure 3.32: Radial growth study of Er^{3+} doped $La(OH)_3$ micro-spheres, synthesized using a 300 mM inner electrolyte with 96% $La(NO_3)_3$ and 4% $Er(NO_3)_3$, 5.5 cm from the RDF interface using (a) Radial growth (μm) as a function of time (h), (b) SEM image of the broken micro-spheres, (c) Image under optical microscope of the growing sphere at T= 7h.

CHAPTER 4

PRIMARY THERMOMETRY

4.1 Introduction

Ln^{3+} doped materials are excellent candidates for luminescent thermometry. Since Ln^{3+} ions work in the spectral ranges where biological tissue has minimal absorption and negligible auto-fluorescence, luminescent thermometers based on Ln^{3+} doped materials have been widely employed in intra-cellular measurements[131], [132] and tumor temperature mapping during thermal therapies[75], [133].

Er^{3+} doped materials are widely used for thermometric purposes due to their $^2H_{11/2} \rightarrow^4 I_{15/2}$ and $^4S_{3/2} \rightarrow^4 I_{15/2}$ transitions shown in figure 4.1. The populations of $^2H_{11/2}$ and $^4S_{3/2}$ are thermally coupled; in other words, even though the levels are spectrally separated, they are not far away enough for the exponential temperature decay rate to be small. The population distribution of thermally coupled levels follows Boltzmann statistics; therefore, the intensity ratio of these two transitions is temperature dependant.

N_1 and N_2 are related by [134]:

$$\frac{N_2}{N_1} = \left(\frac{g_2}{g_1}\right) exp\left(\frac{-\Delta E}{k_B T}\right)$$

$$\frac{I_2}{I_1} \propto \frac{N_2}{N_1}$$

where k_B is the Boltzmann constant, g_1 and g_2 are the degeneracies of the two levels, ΔE the energy difference between the barycenters, B is the pre-exponential factor dependent on the degeneracies, branching ratios, spontaneous absorption coefficients, and frequencies of the $^2H_{11/2} \rightarrow^4 I_{15/2}$ and $^4S_{3/2} \rightarrow^4 I_{15/2}$ transitions.

Performance of ratio-metric luminescent thermometers should be quantified. To evaluate the performance of a luminescent thermometer, the relative thermal sensitivity, S_r, and the minimum temperature uncertainty, δT, are determined.

The conversion of integrated intensity in temperature is made through the thermometric parameter Δ. In case of the single-center ratio-metric thermometer Er^{3+} doped La$_2$O$_3$, Δ is defined as [134]–[136]:
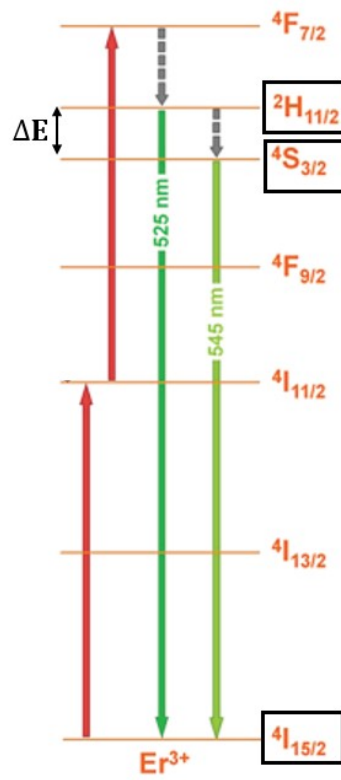
Figure 4.1: Er^{3+} temperature sensitive transitions, adapted from [75].

$$\Delta = \frac{I_{523}}{I_{546}} = B exp\left(\frac{-\Delta E}{k_B T}\right)$$

where I_{523} and I_{546} are the integrated intensities of two transitions $^2H_{11/2} \rightarrow^4 I_{15/2}$ and $^4S_{3/2} \rightarrow^4 I_{15/2}$ respectively.

The relative thermal sensitivity S_r indicates the relative change of Δ per degree of temperature change and is defined by [134]–[136]:

$$S_r = \frac{1}{\Delta}\left|\frac{\partial\Delta}{\partial T}\right|$$

If B is temperature dependant[134], [137]:

$$S_r = \frac{1}{B exp\left(-\frac{\Delta E}{k_B T}\right)} \cdot \left|\frac{\partial B}{\partial T}exp\left(-\frac{\Delta E}{k_B T}\right) - B\frac{\Delta E}{k_B T^2}exp\left(-\frac{\Delta E}{k_B T}\right)\right| = \left|\frac{1}{B}\frac{\partial B}{\partial T} - \frac{\Delta E}{k_B T^2}\right|$$

Assuming B is temperature independent

$$S_r = \frac{\Delta E}{k_B T^2}$$

The temperature uncertainty (or temperature resolution) δT describes the smallest temperature resolvable by the thermometer which is dependent on the material used and on the experimental setup. An estimate for the temperature uncertainty is given by [134]:

$$\delta T = \frac{1}{S_r}\frac{\delta\Delta}{\Delta}$$

In this section, Er^{3+} doped La_2O_3 micro-spheres synthesized using RDF will be used as a luminescent primary thermometer. The performance of this primary thermometer will be evaluated by calculating thermal sensitivity and minimum temperature uncertainty.

4.2   Results and Discussion

4.2.1   *Calibration Curve*

A small amount of the Er^{3+} doped La_2O_3 powder sample obtained prior using a 50mM inner electrolyte composed of 4% $Er(NO_3)_3$, 96% $La(NO_3)_3$ is immersed in methanol inside a quartz cuvette. The emission spectrum of the sample is recorded at different temperatures ranging between 25-60°C after an excitation of $\lambda_{ex} = 386$ nm is applied. The fluorometer is connected to a circulator bath which allows the temperature regulation of the oxide sample in the cuvette. Before each spectrum is collected, the cuvette is placed in the 25°C sonicator for 20 seconds, and then left to equilibrate with the temperature of the fluorometer for 60 seconds before an excitation is applied. 3 trials were performed. The conditions of each trial are

Trial	Emission spectra collected at each temperature	Amount of time sample is subjected to each temperature (min)
A	1	2
B	2	4
C	5	10-15

Table 4.1: Er^{3+} doped La_2O_3 temperature sensing under different conditions.
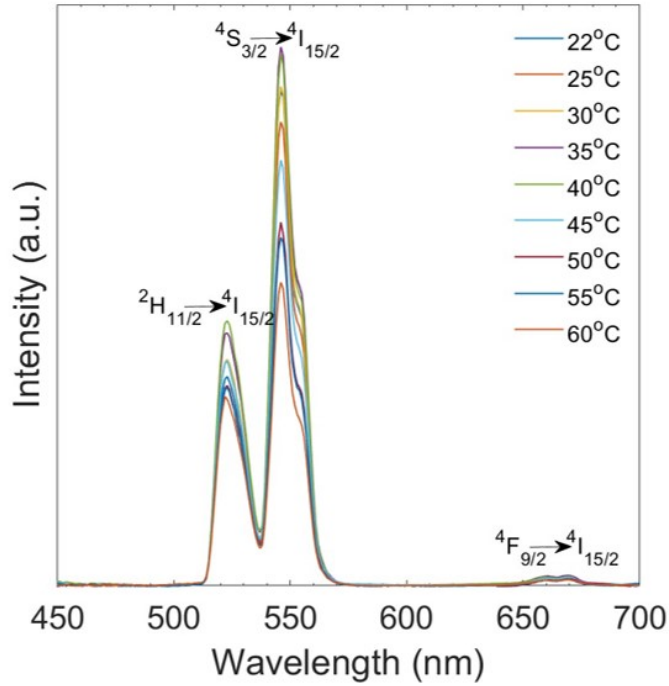
Figure 4.2: Emission spectra of Er^{3+} doped La_2O_3 obtained at different temperatures, $\lambda_{ex.} = 386$nm.

tabulated in 4.1. Emission spectra obtained for the sample at each temperature in trial A are shown in figure 4.2. The intensity for each transition as a function of temperature in trial C is shown in figure 4.3. The common trend seen in all three trials is a slight increase in intensity for each transition followed by a decrease as the temperature increases. When plotting Δ (ratio of the Intensities of $^2H_{11/2} \rightarrow^4 I_{15/2}$ to $^4S_{3/2} \rightarrow^4 I_{15/2}$) as a function of temperature, Δ increases as the temperature increases which is expected for 2 thermally coupled levels. A calibration curve showing variation of Δ as a function of T($^\circ$C) for trial C is shown in figure 4.4. The linear fit to the data has the equation y=0.005x-1.0716 and r^2=0.99.

4.2.2   *Performance of ratio-metric luminescent thermometer*

Since $^2H_{11/2}$ and $^4S_{3/2}$ are thermally coupled, the intensity ratio of $^2H_{11/2} \rightarrow^4 I_{15/2}$ to $^4S_{3/2} \rightarrow^4 I_{15/2}$ is temperature-dependent according to Boltzmann statistics. The
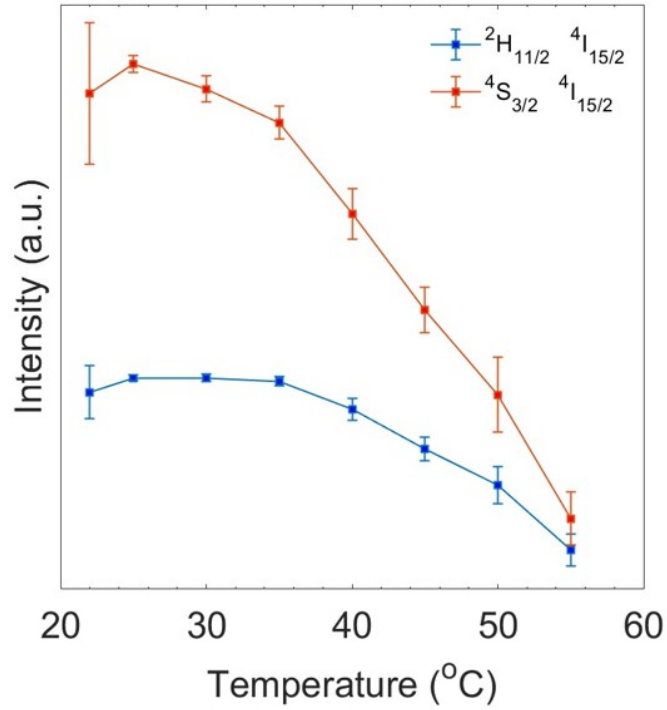
Figure 4.3: Intensity of $^2H_{11/2} \to^4 I_{15/2}$ and $^4S_{3/2} \to^4 I_{15/2}$ transitions as a function of Temperature(°C).
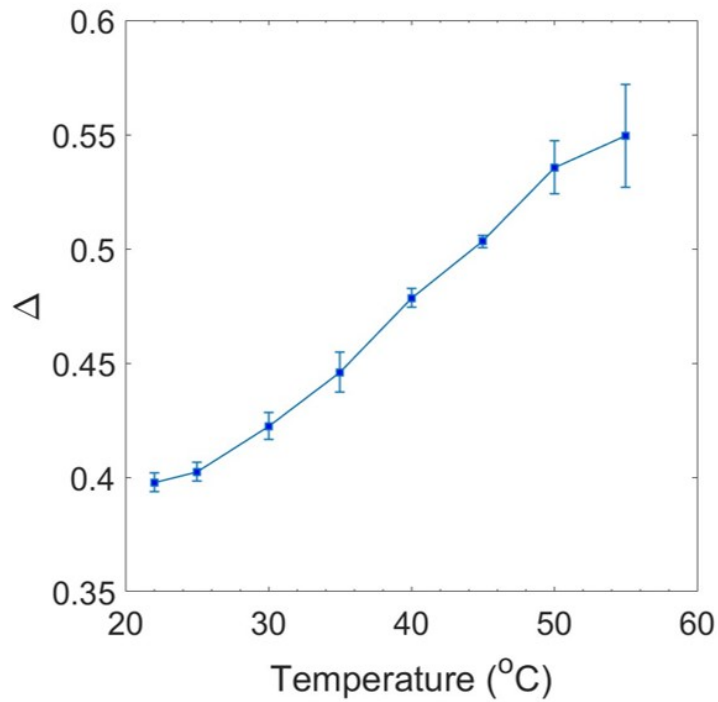
Figure 4.4: Calibration curve showing variation of Δ as a function of T°C.
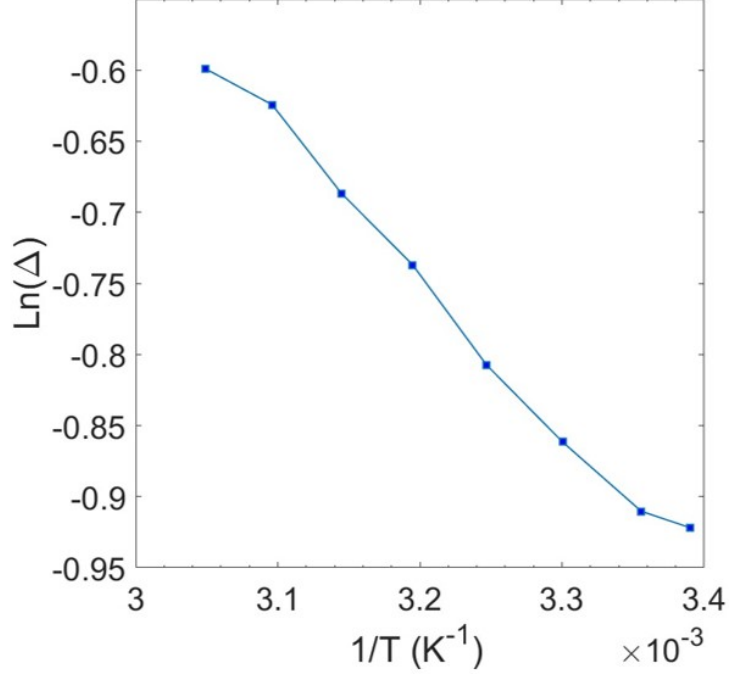
Figure 4.5: $ln(\Delta)$ as a function of $\left(\frac{1}{T(K)}\right)$ for Trial C.

relationship between the intensity ratio and temperature is given by [135]:

$$\Delta = \frac{I_{523}}{I_{546}} = B exp\left(\frac{-\Delta E}{k_B T}\right)$$

$$ln\left(\frac{I_{523}}{I_{546}}\right) = \frac{-\Delta E}{k_B}\left(\frac{1}{T}\right) + lnB$$

A plot of $ln(\Delta)$ as a function of $\left(\frac{1}{T(^\circ C)}\right)$ for trial C is shown in figure 4.5. A linear plot is obtained of equation $y = -1022x + 2.5246$ and r^2=0.9908. This further validates the functionality of the Er^{3+} doped La$_2$O$_3$ as a primary thermometer.

ΔE is evaluated by deconvoluting the emission spectra at room temperature by a set of Gaussian peaks and evaluating the position of the $^2H_{11/2} \rightarrow^4 I_{15/2}$ and $^4S_{3/2} \rightarrow^4 I_{15/2}$ transitions' barycenter[135], [138]. The barycenter of $^2H_{11/2} \rightarrow^4 I_{15/2}$ is found at 523 nm and that of $^4S_{3/2} \rightarrow^4 I_{15/2}$ is found at 546 nm, therefore:

$$\Delta E = 1.601 \cdot 10^{-20} j = 805.4 cm^{-1}$$

This value is in good agreement with those reported in the literature[138].

$$\frac{\Delta E}{k} = \frac{1.601 \cdot 10^{-20}}{1.38 \cdot 10^{-23}} = 1160$$

The value $\frac{\Delta E}{k} = 1160$ is in good agreement with the value of $\frac{\Delta E}{k} = 1022$ obtained from the negative of the slope of figure 4.5. Determining the ΔE parameter from the emission spectra is the preferred method[134].

A plot of the thermal sensitivity, for trial C, assuming parameter B is temperature independent, is shown in figure 4.6. The S_r of 1 is within the commonly reported range for Er^{3+} based thermometers ($\approx$ 0.2–1 % K^{-1})[135]. A plot for temperature uncertainty for trial C is shown in figure 4.7. δT depends on the SNR of the measurement, and is strongly affected by the type and performance of the detector and experimental conditions, such as luminescent material quantity, acquisition time, and background noise, thus precluding a fair comparison with reported values in the literature[135], [139]. However, typical portable detection systems have a δT that ranges between 0.01-0.1K[136]. The reason trial C exhibits larger δT values specially at higher temperatures could result from several factors. To begin with, trial C consists of taking only 5 emission spectra at each temperature. Typically, these measurements are conducted after a larger amount of spectra are collected (e.g. 150 emission spectra collected in [135]). The large δT at higher temperatures is also because of the nature of the experiment conducted in trial C. The sample is left at each temperatures for 10-15 minutes which may not be required in typical applications. This is problematic at temperatures above 323K because the intensity of each transition drops the more the sample is exposed to higher temperatures despite Δ increasing as the temperature increases; therefore, $\delta\Delta$ is larger at higher temperatures. Since δT heavily depends on $\delta\Delta$, δT is large at higher temperatures. This effect is very pronounced starting at 318 K where there's a sharp rise in the δT in figure 4.7. This sharp rise is because, among the 5 emission spectra collected, the intensities of the transitions are dropping as the sample is kept longer at higher temperature and thus $\delta\Delta$ is increasing. These results are due to the fact that all transitions suffer thermal quenching upon temperature increase. Thermal quenching in micro-sized particles is due to multi-phonon non-radiative relaxation mechanisms, resulting in higher decay probabilities[138], [140], [141]. Lower values of δT are expected when the liquid sample is left at each temperature for a shorter period of time as seen in trials A and B.
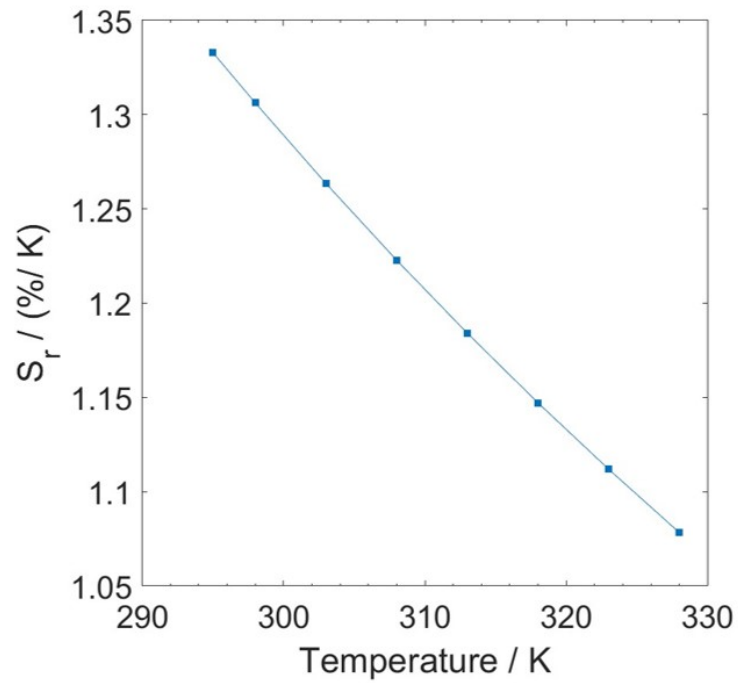
Figure 4.6: Relative thermal sensitivity as a function of temperature with the maximum value of 1.33%/K at 295 K.
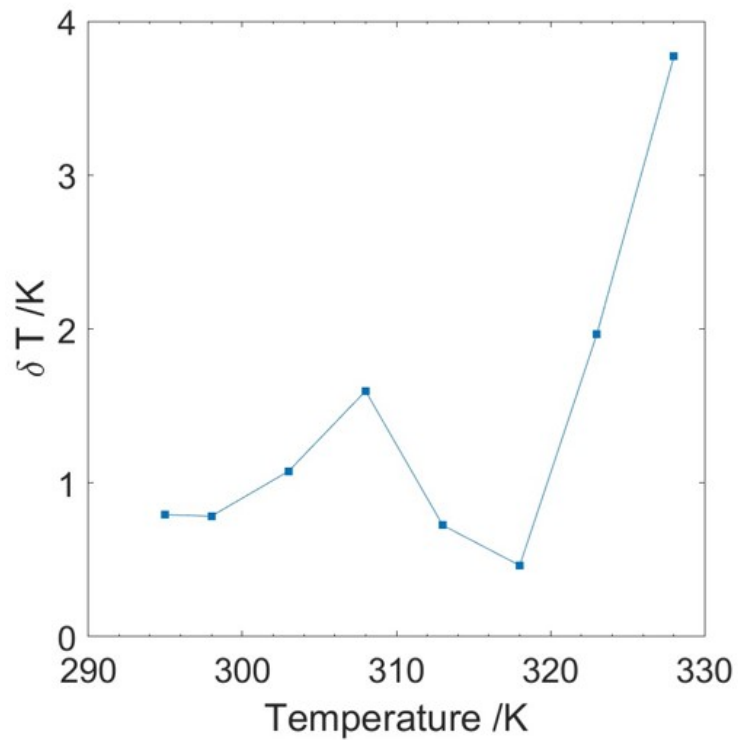
Figure 4.7: Temperature uncertainty (/K) as a function of temperature (/K)

CHAPTER 5

CONCLUSION AND FUTURE WORK

5.1 Conclusion

In this work we report a new two step synthesis method for Ln^{3+} doped La_2O_3 using RDF. This method surpasses other methods due to it's practicality and final product characteristics, for it has allowed the synthesis of mono-dispersed, spherical, luminescent Ln^{3+} doped La_2O_3 via a short procedure that primarily takes place at room temperature and pressure. In the first step, Ln^{3+} doped $La_2(OH)_3$ micro-spheres are synthesized using an RDF framework with a 50 mM inner electrolyte $Ln(NO_3)_3$ where $Ln^{3+}=$ La^{3+}, Er^{3+}, Eu^{3+}, Tb^{3+}, or Sm^{3+} embedded in 1% agar gel and 14 M NH_3 outer electrolyte. The outer electrolyte is poured onto the inner electrolyte embedded in agar, and it's left to diffuse through the gel for 5 days. The resulting precipitate is identified by PXRD to be Ln^{3+} doped $La(OH)_3$. The spherical morphology of the $La(OH)_3$ is shown using SEM where each region of the tube is confirmed to have monodisperesed Ln^{3+} doped $La(OH)_3$ micro-spheres. The gradient in supersaturation in the RDF is translated to a gradient in size of the final product, where smaller spheres are formed closer to the interface, and a progressive increase in the size of the spheres is observed away from the interface. Afterwards, the precipitate is washed, dried in the vacuum oven for 1 day, and oxidized in the furnace at 800°C for 3 hours. The PXRD pattern of the final product confirms it to be pure La_2O_3. SEM images of the final product show the spherical morphology of the Ln^{3+} doped $La(OH)_3$ precipitate obtained via RDF is retained after calcination to La_2O_3. Characterization of Ln^{3+} doped $La(OH)_3$ and Ln^{3+} doped La_2O_3 is achieved via PXRD, SEM, FTIR, BET, DLS, and Fluorescence spectroscopy. Optimization of the Ln^{3+} doped La_2O_3 final product includes varying the amount of dopant in the initial inner electrolyte solution and monitoring the intensities of each transition in the luminescence emission spectra in order to find which inner electrolyte composition will lead to a final product with optimum luminescence intensity.

Er^{3+} doped La_2O_3 micro-spheres obtained via RDF are used for primary thermometry. The emission spectrum for Er^{3+} doped La_2O_3 immersed in methanol is recorded at different temperatures ranging from 295K till 333K. As the temperature increases, the intensity ratio of the thermally coupled levels $^2H_{11/2} \to^4 I_{15/2}$ to $^4S_{3/2} \to^4 I_{15/2}$ increases. A calibration curve showing the variation of Δ as a func-

tion of T exhibits a linear relationship between the 2 variables having $r^2 = 0.99$. Considering the populations of both levels follow Boltzmann statistics, $ln(\Delta)$ vs T also exhibits linear behaviour. The sensitivity of the thermometer is in agreement with the commonly reported range for Er^{3+} based thermometers, thus confirming the functionality of Er^{3+} based thermometer synthesized using RDF.

5.2 Future Work

5.2.1 *RDF*

Considering the fact that Ln^{3+} doped La_2O_3 scale in the nano-meter range when being used for biological applications including sensing and imaging, optimization of a synthesis procedure for nano-meter sized Ln^{3+} doped La_2O_3 using a lower inner electrolyte concentration should be the next step[22]. Knowing that luminescence intensity varies depending on inner electrolyte concentration, and on % dopant integrated in the inner electrolyte, and knowing how morphology can shift from spherical to rod-like if too much dopant is added, an optimization procedure to get nano-meter sized Ln^{3+} doped La_2O_3 should be executed bearing all factors in mind.

5.2.2 *Thermometry*

Getting an Ln^{3+} doped La_2O_3 thermometer with higher sensitivity is also a promising future endeavor. The sensitivity of single center thermometers using Ln^{3+} doped La_2O_3 are limited to values of the order $1.0\%.K^{-1}$[138]. Multicenter upconversion thermometry, on the other hand, exploits the different thermal dependence of the intensity of two lines generated in distinct Ln^{3+} ions, thus achieving higher sensitivity. Secondary thermometers can render values of $S_r > 3\%.K^{-1}$. Co-doping using RDF should also be used to create a secondary thermometer. For instance, previous reports of co-doping an $KLuWO_4$ oxide matrix with Tm^{3+} and Ho^{3+} can be used to create a secondary thermometer where the intensity ratio of the Tm^{3+} $^3F_{2,3} \rightarrow^3 H_6$ at 696 nm and that of Ho^{3+} $^5S_2,^5 F_4 \rightarrow^5 I_7$ at 755 nm can be used to create a thermometer with sensitivity $2.8\%.K^{-1}$ and $\delta T = 0.2K$ at 300 K[134]. Since secondary thermometers require new calibration every time they operate in a distinct medium, double thermometers should also be explored. Double thermometers include secondary thermometers combined with primary thermometers in a single device to attain a thermometer with higher sensitivity while avoiding calibration in different media. An example includes Yb^{3+}/Er^{3+} and Yb^{3+}/Tb^{3+} doped UCNPs of distinct sizes embedding in poly(methyl methacrylate) films to fabricate self calibrated double luminescent thermometers. In this case, the primary thermal probe operates based on the ratio of the $^2H_{11/2} \rightarrow^4 I_{15/2}$ and $^4S_{3/2} \rightarrow^4 I_{15/2}$ Er^{3+} transitions and the secondary thermometer uses the ratio between integrated intensities of the $^1G_4 \rightarrow^3 H_6$ transition of Tm^{3+} and the $^4S_{3/2} \rightarrow^4 I_{15/2}$ of Er^{3+} transitions. In this case the primary thermometer can be used to calibrate the secondary thermometer, avoiding calibration procedures whenever the system operates in new experimental conditions[138].
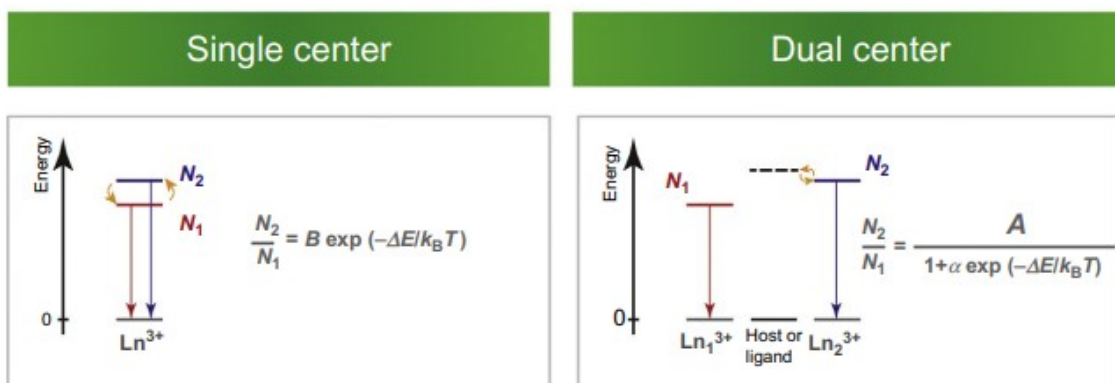
Figure 5.1: Classification of ratiometric luminescent thermometers in single- and dual-center emissions. Adapted from [136].

Bibliography

[1] A. Lewis, M. Seckler, H. Kramer, and G. Van Rosmalen, Industrial crystallization: fundamentals and applications. Cambridge University Press, 2015.

[2] G. A. Al Akhrass, M. Ammar, H. El-Rassy, and M. Al-Ghoul, "Self-assembled lanthanum hydroxide microspheres within a reaction–diffusion framework: Synthesis, characterization, control and application," RSC advances, vol. 6, no. 5, pp. 3433–3439, 2016.

[3] X. Chen, Y. Liu, and D. Tu, Lanthanide-doped luminescent nanomaterials. Springer, 2016.

[4] J.-C. G. Bünzli, "Lanthanide luminescence for biomedical analyses and imaging," Chemical reviews, vol. 110, no. 5, pp. 2729–2755, 2010.

[5] R. Yadav, S. Dhoble, and S. Rai, "Improved photon upconversion photoluminescence and intrinsic optical bistability from a rare earth co-doped lanthanum oxide phosphor via bi 3+ doping," New Journal of Chemistry, vol. 42, no. 9, pp. 7272–7282, 2018.

[6] K. Binnemans, "Interpretation of europium (iii) spectra," Coordination Chemistry Reviews, vol. 295, pp. 1–45, 2015.

[7] K. Binnemans, "Lanthanide-based luminescent hybrid materials," Chemical reviews, vol. 109, no. 9, pp. 4283–4374, 2009.

[8] L. Na, L. Bin, S. Jiao-Jiao, et al., "Research progress of rare-earth doped laser crystals in visible region," Journal of Inorganic Materials, vol. 34, no. 6, pp. 573–589, 2019.

[9] R. Ilmi, S. Kansız, N. K. Al-Rasbi, N. Dege, P. R. Raithby, and M. S. Khan, "Towards white light emission from a hybrid thin film of a self-assembled ternary samarium (iii) complex," New Journal of Chemistry, vol. 44, no. 15, pp. 5673–5683, 2020.

[10] V. Gorelik and M. Burdanova, "Photoluminescence and polariton dispersion in erbium nitrate hydrate," Laser Physics, vol. 24, no. 12, p. 125 001, 2014.

[11] N. Filipescu, W. Sager, and F. Serafin, "Substituent effects on intramolecular energy transfer. ii. fluorescence spectra of europium and terbium β-diketone chelates," The Journal of Physical Chemistry, vol. 68, no. 11, pp. 3324–3346, 1964.

[12] J.-C. G. Bünzli, "Lanthanide luminescence: From a mystery to rationalization, understanding, and applications," in Handbook on the Physics and Chemistry of Rare Earths, vol. 50, Elsevier, 2016, pp. 141–176.

[13] U. Cho and J. K. Chen, "Lanthanide-based optical probes of biological systems," Cell chemical biology, vol. 27, no. 8, pp. 921–936, 2020.

[14] M. Y. Berezin and S. Achilefu, "Fluorescence lifetime measurements and biological imaging," Chemical reviews, vol. 110, no. 5, pp. 2641–2684, 2010.

[15] B. Chen and F. Wang, "Combating concentration quenching in upconversion nanoparticles," Accounts of Chemical Research, vol. 53, no. 2, pp. 358–367, 2019.

[16] D. F. Swinehart, "The beer-lambert law," Journal of chemical education, vol. 39, no. 7, p. 333, 1962.

[17] A. Nadort, J. Zhao, and E. M. Goldys, "Lanthanide upconversion luminescence at the nanoscale: Fundamentals and optical properties," Nanoscale, vol. 8, no. 27, pp. 13 099–13 130, 2016.

[18] H. M. Pandas and M. Fazli, "Preparation and application of la2o3 and cuo nano particles as catalysts for ammonium perchlorate thermal decomposition," Propellants, Explosives, Pyrotechnics, vol. 43, no. 11, pp. 1096–1104, 2018.

[19] R. F. Madani, I. Sofianty, A. G. P. Sari, R. Maryanti, and A. B. D. Nandiyanto, "Synthesis methods and green synthesis of lanthanum oxide nanoparticles: A review," Arabian Journal of Chemical and Environmental Research, vol. 8, no. 2, pp. 287–314, 2021.

[20] N. Ramjeyanthi, M. Alagar, and D. Muthuraman, "Synthesis, structural and optical characterization of uncalcined lanthanum oxide nanoparticles by co-precipitation method," International Journal of Interdisciplinary Research and Innovation, vol. 6, no. 3, pp. 389–395, 2018.

[21] J. Sheng, S. Zhang, S. Lv, and W. Sun, "Surfactant-assisted synthesis and characterization of lanthanum oxide nanostructures," Journal of materials science, vol. 42, pp. 9565–9571, 2007.

[22] G. Chen, H. Qiu, P. N. Prasad, and X. Chen, "Upconversion nanoparticles: Design, nanochemistry, and applications in theranostics," Chemical reviews, vol. 114, no. 10, pp. 5161–5214, 2014.

[23] Y.-W. Zhang, X. Sun, R. Si, L.-P. You, and C.-H. Yan, "Single-crystalline and monodisperse laf3 triangular nanoplates from a single-source precursor," Journal of the American Chemical Society, vol. 127, no. 10, pp. 3260–3261, 2005.

[24] J.-C. Boyer, F. Vetrone, L. A. Cuccia, and J. A. Capobianco, "Synthesis of colloidal upconverting nayf4 nanocrystals doped with er3+, yb3+ and tm3+, yb3+ via thermal decomposition of lanthanide trifluoroacetate precursors," Journal of the American Chemical Society, vol. 128, no. 23, pp. 7444–7445, 2006.

[25] H.-X. Mai, Y.-W. Zhang, R. Si, et al., "High-quality sodium rare-earth fluoride nanocrystals: Controlled synthesis and optical properties," Journal of the American Chemical Society, vol. 128, no. 19, pp. 6426–6436, 2006.

[26] V. Mahalingam, F. Vetrone, R. Naccache, A. Speghini, and J. A. Capobianco, "Colloidal tm3+/yb3+-doped liyf4 nanocrystals: Multiple luminescence spanning the uv to nir regions via low-energy excitation," Advanced Materials, vol. 21, no. 40, pp. 4025–4028, 2009.

[27] Y.-P. Du, X. Sun, Y.-W. Zhang, Z.-G. Yan, L.-D. Sun, and C.-H. Yan, "Uniform alkaline earth fluoride nanocrystals with diverse shapes grown from thermolysis of metal trifluoroacetates in hot surfactant solutions," Crystal Growth and Design, vol. 9, no. 4, pp. 2013–2019, 2009.

[28] F. Wang and X. Liu, "Upconversion multicolor fine-tuning: Visible to near-infrared emission from lanthanide-doped nayf4 nanoparticles," Journal of the American Chemical Society, vol. 130, no. 17, pp. 5642–5643, 2008.

[29] H. Qiu, G. Chen, L. Sun, S. Hao, G. Han, and C. Yang, "Ethylenediaminetetraacetic acid (edta)-controlled synthesis of multicolor lanthanide doped bayf 5 upconversion nanocrystals," Journal of Materials Chemistry, vol. 21, no. 43, pp. 17 202–17 208, 2011.

[30] J.-H. Zeng, J. Su, Z.-H. Li, R.-X. Yan, and Y.-D. Li, "Synthesis and upconversion luminescence of hexagonal-phase nayf4: Yb, er3+ phosphors of controlled size and morphology," Advanced Materials, vol. 17, no. 17, pp. 2119–2123, 2005.

[31] L. Wang, P. Li, and Y. Li, "Down-and up-conversion luminescent nanorods," Advanced Materials, vol. 19, no. 20, pp. 3304–3307, 2007.

[32] M. Salavati-Niasari, G. Hosseinzadeh, and F. Davar, "Synthesis of lanthanum hydroxide and lanthanum oxide nanoparticles by sonochemical method," Journal of Alloys and Compounds, vol. 509, no. 10, pp. 4098–4103, 2011.

[33] L. Wang, W. Qin, Z. Liu, et al., "Improved 800 nm emission of tm 3+ sensitized by yb 3+ and ho 3+ in β-nayf 4 nanocrystals under 980 nm excitation," Optics Express, vol. 20, no. 7, pp. 7602–7607, 2012.

[34] F. Zhang, J. Li, J. Shan, L. Xu, and D. Zhao, "Shape, size, and phase-controlled rare-earth fluoride nanocrystals with optical up-conversion properties," Chemistry–A European Journal, vol. 15, no. 41, pp. 11 010–11 019, 2009.

[35] D. Yang, X. Kang, M. Shang, G. Li, C. Li, J. Lin, et al., "Size and shape controllable synthesis and luminescent properties of bagdf5: Ce3+/ln3+ (ln= sm, dy, eu, tb) nano/submicrocrystals by a facile hydrothermal process," Nanoscale, vol. 3, no. 6, pp. 2589–2595, 2011.

[36] Z.-j. Liu, X.-x. Song, and Q. Tang, "Development of pegylated kmnf 3 nanoparticles as a t 1-weighted contrast agent: Chemical synthesis, in vivo brain mr imaging, and accounting for high relaxivity," Nanoscale, vol. 5, no. 11, pp. 5073–5079, 2013.

[37] P. W. Voorhees, "The theory of ostwald ripening," Journal of Statistical Physics, vol. 38, pp. 231–252, 1985.

[38] H.-S. Qian and Y. Zhang, "Synthesis of hexagonal-phase core- shell nayf4 nanocrystals with tunable upconversion fluorescence," Langmuir, vol. 24, no. 21, pp. 12 123–12 125, 2008.

[39] Z. Li and Y. Zhang, "An efficient and user-friendly method for the synthesis of hexagonal-phase nayf4: Yb, er/tm nanocrystals with controllable shape and upconversion fluorescence," Nanotechnology, vol. 19, no. 34, p. 345 606, 2008.

[40] Z. Li, Y. Zhang, and S. Jiang, "Multicolor core/shell-structured upconversion fluorescent nanoparticles," Advanced Materials, vol. 20, no. 24, pp. 4765–4769, 2008.

[41] S. T. Aruna and A. S. Mukasyan, "Combustion synthesis and nanomaterials," Current opinion in solid state and materials science, vol. 12, no. 3-4, pp. 44–50, 2008.

[42] H. Xu, B. W. Zeiger, and K. S. Suslick, "Sonochemical synthesis of nanomaterials," Chemical Society Reviews, vol. 42, no. 7, pp. 2555–2567, 2013.

[43] D. S. Kumar, B. J. Kumar, and H. Mahesh, "Quantum nanostructures (qds): An overview," Synthesis of inorganic nanomaterials, pp. 59–88, 2018.

[44] A. de Bettencourt-Dias, Luminescence of lanthanide ions. John Wiley & Sons, 2014.

[45] D. Li, H. Ågren, and G. Chen, "Near infrared harvesting dye-sensitized solar cells enabled by rare-earth upconversion materials," Dalton Transactions, vol. 47, no. 26, pp. 8526–8537, 2018.

[46] D. K. Chatterjee, M. K. Gnanasammandhan, and Y. Zhang, "Small upconverting fluorescent nanoparticles for biomedical applications," Small, vol. 6, no. 24, pp. 2781–2795, 2010.

[47] C. Bouzigues, T. Gacoin, and A. Alexandrou, "Biological applications of rare-earth based nanoparticles," ACS nano, vol. 5, no. 11, pp. 8488–8505, 2011.

[48] Y. Liu, D. Tu, H. Zhu, E. Ma, and X. Chen, "Lanthanide-doped luminescent nano-bioprobes: From fundamentals to biodetection," Nanoscale, vol. 5, no. 4, pp. 1369–1384, 2013.

[49] F. Wang and X. Liu, "Recent advances in the chemistry of lanthanide-doped upconversion nanocrystals," Chemical Society Reviews, vol. 38, no. 4, pp. 976–989, 2009.

[50] H. Zijlmans, J. Bonnet, J. Burton, et al., "Detection of cell and tissue surface antigens using up-converting phosphors: A new reporter technology," Analytical biochemistry, vol. 267, no. 1, pp. 30–36, 1999.

[51] J. Hampl, M. Hall, N. A. Mufti, et al., "Upconverting phosphor reporters in immunochromatographic assays," Analytical biochemistry, vol. 288, no. 2, pp. 176–187, 2001.

[52] R. S. Niedbala, H. Feindt, K. Kardos, et al., "Detection of analytes by immunoassay using up-converting phosphor technology," Analytical Biochemistry, vol. 293, no. 1, pp. 22–30, 2001.

[53] P. Corstjens, M. Zuiderwijk, A. Brink, et al., Use of up-converting phosphor reporters in lateral-flow assays, 2001.

[54] L. Wang and Y. Li, "Green upconversion nanocrystals for dna detection," Chemical Communications, no. 24, pp. 2557–2559, 2006.

[55] M. Zuiderwijk, H. J. Tanke, R. S. Niedbala, and P. L. Corstjens, "An amplification-free hybridization-based dna assay to detect streptococcus pneumoniae utilizing the up-converting phosphor technology," Clinical biochemistry, vol. 36, no. 5, pp. 401–403, 2003.

[56] F. Van De Rijke, H. Zijlmans, S. Li, et al., "Up-converting phosphor reporters for nucleic acid microarrays," Nature biotechnology, vol. 19, no. 3, pp. 273–276, 2001.

[57] C. Morgan and A. Mitchell, "Prospects for applications of lanthanide-based upconverting surfaces to bioassay and detection," Biosensors and Bioelectronics, vol. 22, no. 8, pp. 1769–1775, 2007.

[58] D. Tu, L. Liu, Q. Ju, et al., "Time-resolved fret biosensor based on amine-functionalized lanthanide-doped nayf4 nanocrystals," Angewandte Chemie International Edition, vol. 50, no. 28, pp. 6306–6310, 2011.

[59] D. Casanova, D. Giaume, T. Gacoin, J.-P. Boilot, and A. Alexandrou, "Single lanthanide-doped oxide nanoparticles as donors in fluorescence resonance energy transfer experiments," The Journal of Physical Chemistry B, vol. 110, no. 39, pp. 19 264–19 270, 2006.

[60] K. Kuningas, T. Rantanen, T. Ukonaho, T. Lövgren, and T. Soukka, "Homogeneous assay technology based on upconverting phosphors," Analytical Chemistry, vol. 77, no. 22, pp. 7348–7355, 2005.

[61] P. Zhang, S. Rogelj, K. Nguyen, and D. Wheeler, "Design of a highly sensitive and specific nucleotide sensor based on photon upconverting particles," Journal of the American Chemical Society, vol. 128, no. 38, pp. 12 410–12 411, 2006.

[62] M. Wang, W. Hou, C.-C. Mi, et al., "Immunoassay of goat antihuman im-munoglobulin g antibody based on luminescence resonance energy trans-fer between near-infrared responsive nayf4: Yb, er upconversion fluorescent nanoparticles and gold nanoparticles," Analytical chemistry, vol. 81, no. 21, pp. 8783–8789, 2009.

[63] L. Wang, R. Yan, Z. Huo, et al., "Fluorescence resonant energy transfer biosensor based on upconversion-luminescent nanoparticles," Angewandte Chemie International Edition, vol. 44, no. 37, pp. 6054–6057, 2005.

[64] J. Chen and J. X. Zhao, "Upconversion nanomaterials: Synthesis, mechanism, and applications in sensing," Sensors, vol. 12, no. 3, pp. 2414–2435, 2012.

[65] J. Peng, W. Xu, C. L. Teoh, et al., "High-efficiency in vitro and in vivo detection of zn2+ by dye-assembled upconversion nanoparticles," Journal of the American Chemical Society, vol. 137, no. 6, pp. 2336–2342, 2015.

[66] Y. Liu, M. Chen, T. Cao, et al., "A cyanine-modified nanosystem for in vivo upconversion luminescence bioimaging of methylmercury," Journal of the American Chemical Society, vol. 135, no. 26, pp. 9869–9876, 2013.

[67] J. Zhang, B. Li, L. Zhang, and H. Jiang, "An optical sensor for cu (ii) detec-tion with upconverting luminescent nanoparticles as an excitation source," Chemical Communications, vol. 48, no. 40, pp. 4860–4862, 2012.

[68] M. Holland and L. Kozlowski, "Clinical features and management of cyanide poisoning.," Clinical pharmacy, vol. 5, no. 9, pp. 737–741, 1986.

[69] L. Yao, J. Zhou, J. Liu, W. Feng, and F. Li, "Iridium-complex-modified upconversion nanophosphors for effective lret detection of cyanide anions in pure water," Advanced Functional Materials, vol. 22, no. 13, pp. 2667–2672, 2012.

[70] S. Borisov, G. Nuss, and I. Klimant, "Red light-excitable oxygen sens-ing materials based on platinum (ii) and palladium (ii) benzoporphyrins," Analytical chemistry, vol. 80, no. 24, pp. 9435–9442, 2008.

[71] S. Borisov, D. B. Papkovsky, G. V. Ponomarev, A. S. DeToma, R. Saf, and I. Klimant, "Photophysical properties of the new phosphorescent plat-inum (ii) and palladium (ii) complexes of benzoporphyrins and chlorins," Journal of Photochemistry and Photobiology A: Chemistry, vol. 206, no. 1, pp. 87–92, 2009.

[72] X. Ge, M. Hanson, H. Shen, et al., "Validation of an optical sensor-based high-throughput bioreactor system for mammalian cell culture," Journal of Biotechnology, vol. 122, no. 3, pp. 293–306, 2006.

[73] D. E. Achatz, R. J. Meier, L. H. Fischer, and O. S. Wolfbeis, "Luminescent sensing of oxygen using a quenchable probe and upconverting nanoparticles," Angewandte Chemie International Edition, vol. 50, no. 1, pp. 260–263, 2011.

[74] L. Liu, B. Li, J. Ying, et al., "Synthesis and characterization of a new trifunctional magnetic–photoluminescent–oxygen-sensing nanomaterial," Nanotechnology, vol. 19, no. 49, p. 495 709, 2008.

[75] F. Vetrone, R. Naccache, A. Zamarrón, et al., "Temperature sensing using fluorescent nanothermometers," ACS nano, vol. 4, no. 6, pp. 3254–3258, 2010.

[76] M. Engeser, L. Fabbrizzi, M. Licchelli, and D. Sacchi, "A fluorescent molecular thermometer based on the nickel (ii) high-spin/low-spin interconversion," Chemical Communications, no. 13, pp. 1191–1192, 1999.

[77] S. Wang, S. Westcott, and W. Chen, "Nanoparticle luminescence thermometry," The Journal of Physical Chemistry B, vol. 106, no. 43, pp. 11 203–11 209, 2002.

[78] P. Löw, B. Kim, N. Takama, and C. Bergaud, "High-spatial-resolution surface-temperature mapping using fluorescent thermometry," Small, vol. 4, no. 7, pp. 908–914, 2008.

[79] F. Vetrone, J.-C. Boyer, J. A. Capobianco, A. Speghini, and M. Bettinelli, "Significance of yb 3+ concentration on the upconversion mechanisms in codoped y 2 o 3: Er 3+, yb 3+ nanocrystals," Journal of Applied Physics, vol. 96, no. 1, pp. 661–667, 2004.

[80] E. Saıdi, B. Samson, L. Aigouy, et al., "Scanning thermal imaging by near-field fluorescence spectroscopy," Nanotechnology, vol. 20, no. 11, p. 115 703, 2009.

[81] F. Vetrone, R. Naccache, A. J. de la Fuente, et al., "Intracellular imaging of hela cells by non-functionalized nayf4: Er 3+, yb 3+ upconverting nanoparticles," Nanoscale, vol. 2, no. 4, pp. 495–498, 2010.

[82] L.-N. Sun, H. Peng, M. I. Stich, D. Achatz, and O. S. Wolfbeis, "Ph sensor based on upconverting luminescent lanthanide nanorods," Chemical Communications, no. 33, pp. 5000–5002, 2009.

[83] C. McDonagh, C. S. Burke, and B. D. MacCraith, "Optical chemical sensors," Chemical reviews, vol. 108, no. 2, pp. 400–422, 2008.

[84] O. S. Wolfbeis, "Fiber-optic chemical sensors and biosensors," Analytical chemistry, vol. 78, no. 12, pp. 3859–3874, 2006.

[85] A. Song, S. Parus, and R. Kopelman, "High-performance fiber-optic ph microsensors for practical physiological measurements using a dual-emission sensitive dye," Analytical chemistry, vol. 69, no. 5, pp. 863–867, 1997.

[86] P. T. Snee, R. C. Somers, G. Nair, J. P. Zimmer, M. G. Bawendi, and D. G. Nocera, "A ratiometric cdse/zns nanocrystal ph sensor," Journal of the American Chemical Society, vol. 128, no. 41, pp. 13 320–13 321, 2006.

[87] O. S. Wolfbeis, "Materials for fluorescence-based optical chemical sensors," Journal of Materials Chemistry, vol. 15, no. 27-28, pp. 2657–2669, 2005.

[88] R. Ali, S. M. Saleh, R. J. Meier, H. A. Azab, I. I. Abdelgawad, and O. S. Wolfbeis, "Upconverting nanoparticle based optical sensor for carbon dioxide," Sensors and Actuators B: Chemical, vol. 150, no. 1, pp. 126–131, 2010.

[89] C. G. Cooney, B. C. Towe, and C. R. Eyster, "Optical ph, oxygen and carbon dioxide monitoring using a microdialysis approach," Sensors and Actuators B: Chemical, vol. 69, no. 1-2, pp. 183–188, 2000.

[90] A. Mills and Q. Chang, "Fluorescence plastic thin-film sensor for carbon dioxide," Analyst, vol. 118, no. 7, pp. 839–843, 1993.

[91] O. S. Wolfbeis, L. J. Weis, M. J. Leiner, and W. E. Ziegler, "Fiber-optic fluorosensor for oxygen and carbon dioxide," Analytical chemistry, vol. 60, no. 19, pp. 2028–2030, 1988.

[92] H. S. Mader and O. S. Wolfbeis, "Optical ammonia sensor based on upconverting luminescent nanoparticles," Analytical chemistry, vol. 82, no. 12, pp. 5002–5004, 2010.

[93] S. Wu, G. Han, D. J. Milliron, et al., "Non-blinking and photostable upconverted luminescence from single lanthanide-doped nanocrystals," Proceedings of the National Academy of Sciences, vol. 106, no. 27, pp. 10 917–10 921, 2009.

[94] S. M. Borisov and O. S. Wolfbeis, "Optical biosensors," Chemical reviews, vol. 108, no. 2, pp. 423–461, 2008.

[95] L. Xiong, T. Yang, Y. Yang, C. Xu, and F. Li, "Long-term in vivo biodistribution imaging and toxicity of polyacrylic acid-coated upconversion nanophosphors," Biomaterials, vol. 31, no. 27, pp. 7078–7085, 2010.

[96] R. A. Jalil and Y. Zhang, "Biocompatibility of silica coated nayf4 upconversion fluorescent nanocrystals," Biomaterials, vol. 29, no. 30, pp. 4122–4128, 2008.

[97] L. Cheng, K. Yang, M. Shao, X. Lu, and Z. Liu, "In vivo pharmacokinetics, long-term biodistribution and toxicology study of functionalized upconversion nanoparticles in mice," Nanomedicine, vol. 6, no. 8, pp. 1327–1340, 2011.

[98] J.-C. Zhou, Z.-L. Yang, W. Dong, R.-J. Tang, L.-D. Sun, and C.-H. Yan, "Bioimaging and toxicity assessments of near-infrared upconversion luminescent nayf4: Yb, tm nanocrystals," Biomaterials, vol. 32, no. 34, pp. 9059–9067, 2011.

[99] S. F. Lim, R. Riehn, W. S. Ryu, et al., "In vivo and scanning electron microscopy imaging of upconverting nanophosphors in caenorhabditis elegans," Nano Letters, vol. 6, no. 2, pp. 169–174, 2006.

[100] S. F. Lim, R. Riehn, C.-K. Tung, et al., "Upconverting nanophosphors for bioimaging," Nanotechnology, vol. 20, no. 40, p. 405 701, 2009.

[101] K. Wang, J. Ma, M. He, et al., "Toxicity assessments of near-infrared upconversion luminescent laf3: Yb, er in early development of zebrafish embryos," Theranostics, vol. 3, no. 4, p. 258, 2013.

[102] Y. I. Park, J. H. Kim, K. T. Lee, et al., "Nonblinking and nonbleaching upconverting nanoparticles as an optical imaging nanoprobe and t1 magnetic resonance imaging contrast agent," Advanced Materials, vol. 21, no. 44, pp. 4467–4471, 2009.

[103] T. Cao, T. Yang, Y. Gao, Y. Yang, H. Hu, and F. Li, "Water-soluble nayf4: Yb/er upconversion nanophosphors: Synthesis, characteristics and application in bioimaging," Inorganic Chemistry Communications, vol. 13, no. 3, pp. 392–394, 2010.

[104] Y.-J. Xu, J. Lin, Y. Lu, et al., "Lanthanide co-doped paramagnetic spindle-like mesocrystals for imaging and autophagy induction," Nanoscale, vol. 8, no. 27, pp. 13 399–13 406, 2016.

[105] L. Yu, Y. Lu, N. Man, S.-H. Yu, and L.-P. Wen, "Rare earth oxide nanocrystals induce autophagy in hela cells," Small, vol. 5, no. 24, pp. 2784–2787, 2009.

[106] N.-N. Dong, M. Pedroni, F. Piccinelli, et al., "Nir-to-nir two-photon excited caf2: Tm3+, yb3+ nanoparticles: Multifunctional nanoprobes for highly penetrating fluorescence bio-imaging," ACS nano, vol. 5, no. 11, pp. 8665–8671, 2011.

[107] J.-C. Boyer, M.-P. Manseau, J. I. Murray, and F. C. Van Veggel, "Surface modification of upconverting nayf4 nanoparticles with peg- phosphate ligands for nir (800 nm) biolabeling within the biological window," Langmuir, vol. 26, no. 2, pp. 1157–1164, 2010.

[108] J. Shan, J. Chen, J. Meng, et al., "Biofunctionalization, cytotoxicity, and cell uptake of lanthanide doped hydrophobically ligated nayf 4 upconversion nanophosphors," Journal of Applied Physics, vol. 104, no. 9, p. 094 308, 2008.

[109] H. Akiyama, K. Tokuzen, H. Otsuka, K. Soga, and F. Tashiro, "Application of liposome-encapsulated ceramic phoshpors for cancer cell imaging under near infrared excitation," in Journal of Physics: Conference Series, IOP Publishing, vol. 232, 2010, p. 012 001.

[110] Z. Li, H. Guo, H. Qian, and Y. Hu, "Facile microemulsion route to coat carbonized glucose on upconversion nanocrystals as high luminescence and biocompatible cell-imaging probes," Nanotechnology, vol. 21, no. 31, p. 315 105, 2010.

[111] M. Nyk, R. Kumar, T. Y. Ohulchanskyy, E. J. Bergey, and P. N. Prasad, "High contrast in vitro and in vivo photoluminescence bioimaging using near infrared to near infrared up-conversion in tm3+ and yb3+ doped fluoride nanophosphors," Nano letters, vol. 8, no. 11, pp. 3834–3838, 2008.

[112] D. K. Chatterjee, A. J. Rufaihah, and Y. Zhang, "Upconversion fluorescence imaging of cells and small animals using lanthanide doped nanocrystals," Biomaterials, vol. 29, no. 7, pp. 937–943, 2008.

[113] M. Wang, C.-C. Mi, W.-X. Wang, et al., "Immunolabeling and nir-excited fluorescent imaging of hela cells by using nayf4: Yb, er upconversion nanoparticles," ACS nano, vol. 3, no. 6, pp. 1580–1586, 2009.

[114] H. Kobayashi, N. Kosaka, M. Ogawa, et al., "In vivo multiple color lymphatic imaging using upconverting nanocrystals," Journal of Materials Chemistry, vol. 19, no. 36, pp. 6481–6484, 2009.

[115] S. A. Hilderbrand, F. Shao, C. Salthouse, U. Mahmood, and R. Weissleder, "Upconverting luminescent nanomaterials: Application to in vivo bioimaging," Chemical communications, no. 28, pp. 4188–4190, 2009.

[116] B. A. Grzybowski, Chemistry in motion. John Wiley & Sons, 2009.

[117] R. J. Donnelly, R. Herman, and I. Prigogine, "Non-equilibrium thermodynamics; variational techniques and stability.," Non-equilibrium thermodynamics; variational techniques and stability, 1966.

[118] M. Al-Ghoul, R. Issa, and M. Hmadeh, "Synthesis, size and structural evolution of metal–organic framework-199 via a reaction–diffusion process at room temperature," CrystEngComm, vol. 19, no. 4, pp. 608–612, 2017.

[119] S. Prager, "Periodic precipitation," The Journal of Chemical Physics, vol. 25, no. 2, pp. 279–283, 1956.

[120] G. Dee, "Patterns produced by precipitation at a moving reaction front," Physical review letters, vol. 57, no. 3, p. 275, 1986.

[121] R. Sultan, P. Ortoleva, F. DePasquale, and P. Tartaglia, "Bifurcation of the ostwald-liesegang supersaturation-nucleation-depletion cycle," Earth-Science Reviews, vol. 29, no. 1-4, pp. 163–173, 1990.

[122] R. Sultan and P. Ortoleva, "Periodic and aperiodic macroscopic patterning in two precipitate post-nucleation systems," Physica D: Nonlinear Phenomena, vol. 63, no. 1-2, pp. 202–212, 1993.

[123] T. Antal, M. Droz, J. Magnin, Z. Rácz, and M. Zrinyi, "Derivation of the matalon-packter law for liesegang patterns," The Journal of chemical physics, vol. 109, no. 21, pp. 9479–9486, 1998.

[124] C. Wagner, "Mathematical analysis of the formation of periodic precipitations," Journal of Colloid Science, vol. 5, no. 1, pp. 85–97, 1950.

[125] M. Flicker and J. Ross, "Mechanism of chemical instability for periodic precipitation phenomena," The Journal of Chemical Physics, vol. 60, no. 9, pp. 3458–3465, 1974.

[126] A. B. Yousaf, M. Imran, M. Farooq, and P. Kasak, "Interfacial phenomenon and nanostructural enhancements in palladium loaded lanthanum hydroxide nanorods for heterogeneous catalytic applications," Scientific reports, vol. 8, no. 1, p. 4354, 2018.

[127] H. Kabir, S. H. Nandyala, M. M. Rahman, M. A. Kabir, and A. Stamboulis, "Influence of calcination on the sol–gel synthesis of lanthanum oxide nanoparticles," Applied Physics A, vol. 124, pp. 1–11, 2018.

[128] M. Thommes, K. Kaneko, A. V. Neimark, et al., "Physisorption of gases, with special reference to the evaluation of surface area and pore size distribution (iupac technical report)," Pure and applied chemistry, vol. 87, no. 9-10, pp. 1051–1069, 2015.

[129] P. Zhang, "Adsorption and desorption isotherms," KE Group, 2016.

[130] S. Lee, S. Jang, J.-G. Kang, and Y. Sohn, "Luminescent eu (iii) and tb (iii) activator ions in la (oh) 3 and la2o3 nanowire matrices," Materials Science and Engineering: B, vol. 201, pp. 35–44, 2015.

[131] M. Debasu, H. Oliveira, J. Rocha, and L. Carlos, "Colloidal (gd0. 98nd0. 02) 2o3 nanothermometers operating in a cell culture medium within the first and second biological windows," Journal of Rare Earths, vol. 38, no. 5, pp. 483–491, 2020.

[132] R. Piñol, J. Zeler, C. D. Brites, et al., "Real-time intracellular temperature imaging using lanthanide-bearing polymeric micelles," Nano letters, vol. 20, no. 9, pp. 6466–6472, 2020.

[133] E. Carrasco, B. Del Rosal, F. Sanz-Rodrıguez, et al., "Intratumoral thermal reading during photo-thermal therapy by multifunctional fluorescent nanoparticles," Advanced Functional Materials, vol. 25, no. 4, pp. 615–626, 2015.

[134] C. D. Brites, S. Balabhadra, and L. D. Carlos, "Lanthanide-based thermometers: At the cutting-edge of luminescence thermometry," Advanced Optical Materials, vol. 7, no. 5, p. 1 801 239, 2019.

[135] J. C. Martins, A. Skripka, C. D. Brites, et al., "Upconverting nanoparticles as primary thermometers and power sensors," Frontiers in Photonics, p. 48,

[136] C. Brites, A. Millán, and L. Carlos, "Lanthanides in luminescent thermometry," in Handbook on the Physics and Chemistry of Rare Earths, vol. 49, Elsevier, 2016, pp. 339–427.

[137] L. Li, Y. Zhou, F. Qin, Y. Zheng, H. Zhao, and Z. Zhang, "Modified calculation method of relative sensitivity for fluorescence intensity ratio thermometry," Optics Letters, vol. 42, no. 23, pp. 4837–4840, 2017.

[138] C. D. Brites, E. D. Martınez, R. R. Urbano, C. Rettori, and L. D. Carlos, "Self-calibrated double luminescent thermometers through upconverting nanoparticles," Frontiers in Chemistry, vol. 7, p. 267, 2019.

[139] T. P. Van Swieten, A. Meijerink, and F. T. Rabouw, "Impact of noise and background on measurement uncertainties in luminescence thermometry," ACS photonics, vol. 9, no. 4, pp. 1366–1374, 2022.

[140] X. Shen, Q. Nie, T. Xu, S. Dai, and X. Wang, "Temperature dependence of upconversion luminescence in erbium-doped tellurite glasses," Journal of Luminescence, vol. 130, no. 8, pp. 1353–1356, 2010.

[141] D. Yu, J. Ballato, and R. E. Riman, "Temperature-dependence of multiphonon relaxation of rare-earth ions in solid-state hosts," The Journal of Physical Chemistry C, vol. 120, no. 18, pp. 9958–9964, 2016.